New Overlapping Finite Elements and Their Application in the AMORE Paradigm

by

Junbin Huang

B.E. in Civil Engineering, Tsinghua University (2014)
B.S. in Pure and Applied Mathematics, Tsinghua University (2014)
M.E. in Mechanics, Tsinghua University (2017)

Submitted to the Department of Mechanical Engineering
and the Center for Computational Science & Engineering
in partial fulfillment of the requirements for the degree of

Doctor of Philosophy in Mechanical Engineering and Computation

at the

MASSACHUSETTS INSTITUTE OF TECHNOLOGY

May 2020

Author .....
Department of Mechanical Engineering
Center for Computational Science & Engineering
May 15, 2020

Certified by .....
Klaus-Jürgen Bathe
Professor of Mechanical Engineering
Thesis Supervisor

Accepted by .....
Youssef Marzouk
Associate Professor of Aeronautics and Astronautics
Co-Director, Center for Computational Science & Engineering

Accepted by .....
Nicolas Hadjiconstantinou
Professor of Mechanical Engineering
Chairman, Department Committee on Graduate Students

New Overlapping Finite Elements and Their Application in the AMORE Paradigm

by

Junbin Huang

Submitted to the Department of Mechanical Engineering
and the Center for Computational Science & Engineering
on May 15, 2020, in partial fulfillment of the
requirements for the degree of
Doctor of Philosophy in Mechanical Engineering and Computation

Abstract

The finite element method has become a fundamental analysis tool for modern sciences and engineering. Despite the great improvement in theory and application over the past decades, the need for regular conforming meshes in finite element analysis still requires much human effort in engineering practice. In this thesis we focus on designing novel finite element procedures to reduce the meshing effort expended on constructing a finite element model for solids and structures.

The new meshing paradigm of "automatic meshing with overlapping and regular elements", the AMORE paradigm, has recently been formulated. In this paradigm, the finite elements interior to the domain of interest are undistorted traditional elements and overlapping of elements is used for the discretization near the boundaries. The overlapping of elements gives much freedom to the meshing procedure and results in a much reduced meshing effort. Two types of overlapping are investigated.

In the first case we consider the overlapping of individual polygonal elements and propose new quadrilateral overlapping finite elements. The new formulation combines advantageous aspects from both traditional finite elements and meshless methods. The new overlapping finite elements, being insensitive to mesh distortions and giving high-order accuracy, are used to mesh the boundary regions. Such use leads to an effective meshing procedure as desired.

In the second case we study the overlapping of conforming finite element meshes. Each individual mesh is spanned over a regular subdomain and is allowed to overlap with other meshes in any geometric form. Local fields on individual meshes are then assembled using a partition of unity to give the global compatible field. This new scheme allows very convenient local meshing and enriching so that the meshes can be easily adapted to various geometric features and solution gradients with a reasonable computational expense.

We formulate new schemes, analyze their convergence properties, and demonstrate their performance and their use in AMORE in the solution of various problems.

Thesis Supervisor: Klaus-Jürgen Bathe

Title: Professor of Mechanical Engineering

Acknowledgments

The past three years bring me so many valuable memories. I have been enjoying the comfortable and rigorous academic atmosphere here at MIT.

I would like to first thank my advisor Professor Klaus-Jürgen Bathe for his guidance and support through the Ph.D. program. His insight, patience, encouragement, and knowledge helped me find interesting research topics on the frontiers of finite element methods and work through the difficulties to complete this thesis. His guidance will still light my way in future academic life. I would also like to thank Professor Anthony T. Patera and Professor Nicholas M. Patrikalakis, whose generous help really broadened my horizons, for spending time serving in the thesis committee and their invaluable comments and suggestions.

I would like to express my gratitude to all the knowledgeable professors, the warm-hearted students, and the accommodating staff of MIT. I have learned so much through classes and recitations, and received help from so many people in daily life.

I would like to thank my families for their support and encouragement. Their love is the main source of my motivations.

In addition, I thank my friends at MIT and in China for all the joy and friendship. I want to also thank all my colleagues in the Finite Element Research Group for the helpful discussions.

The final thanks are reserved for the MIT chapel and the Apple Tree for bringing peace to my mind whenever I was stuck on mathematical problems.

THIS PAGE INTENTIONALLY LEFT BLANK

Contents

THIS PAGE INTENTIONALLY LEFT BLANK

List of Figures

List of Tables

THIS PAGE INTENTIONALLY LEFT BLANK

Chapter 1

Introduction

The finite element method has become a fundamental analysis tool for modern sciences and engineering [1]. Despite the great improvement in theory and application over the past decades, the use of finite element methods is still much restricted due to the need of much human effort in meshing the analysis domain.

Meshing becomes a crucial step for finite element analysis because traditional elements are very sensitive to mesh distortions. A much distorted mesh can lead to excessive solution error and the solution procedure may even abort because of numerical issues. Although meshes consisting of simplicial elements can be effectively generated with reasonable mesh quality, such meshes are not preferred in engineering practice due to the poor accuracy of simplicial elements.

To reduce the meshing effort, the overlapping finite elements, overlapping finite element meshes, and a new solution scheme referred to as AMORE (automatic meshing with overlapping and regular elements) have been proposed [2, 3, 4, 5, 6, 7, 8].

1.1 Overlapping elements and overlapping meshes

The main idea of these new schemes is to formulate interpolations by considering the overlapping of elements.

In the earlier development, these overlapping elements were disks (in two-dimensional problems and spheres in three-dimensional problems) [9, 10, 11, 12] and the global

interpolation was constructed using the Shepard functions. Since the method of finite spheres, despite being one of the most effective meshless methods, is still too computationally expensive to solve engineering problems on its own, the interior domain was discretized using regular 4-node finite elements and an effective coupling scheme between disk elements and finite elements was proposed [2, 3]. However, the numerical integration in the method of finite spheres is still too costly for the scheme to be practical and the bandwidth is too large to have reasonable solution expense. The concept of overlapping finite elements was then improved to combine advantageous aspects from traditional finite element interpolations and meshless interpolations [4, 5, 7]. Based upon the new concept, new triangular overlapping finite elements were formulated and the computational efficiency was investigated [5, 7]. The original formulation was then modified to formulate quadrilateral overlapping elements and more details in the use of overlapping elements were discussed [6].

Given a conforming mesh of the analysis domain using triangles and quadrilaterals, (triangular and quadrilateral) overlapping finite elements are formulated as the overlapped regions of polygonal elements. A polygonal element is formally just the collection of elements coupling into the same node. On each polygonal element, a local interpolation is established using the method of finite spheres, but with the Shepard functions interpolated using traditional high-order interpolations. The final interpolation of overlapping elements is then the weighted average of local fields with the weights being traditional low-order shape functions. Since in the interpolation of the method of finite spheres each node is assigned a nodal unknown function, the overlapping elements also have functions as the nodal unknowns instead of single nodal values. In general, polynomial functions are used as the nodal degrees of freedom (dofs). For particular problems, some other functions can be added into the nodal unknowns, e.g. trigonometric functions can be included for the solution of wave propagation problems [13]. The final form of the overlapping interpolation is very similar to the traditional interpolation, i.e. each nodal function contributes to the final field via a shape function, where the expression for the shape function is however much more complicated. The new interpolation therefore leads to a similar

bandwidth structure in the global stiffness matrix as in traditional finite element analysis, and since the shape functions are interpolated as polynomial functions of local coordinates, the numerical integration effort is significantly less than that of meshless methods. In addition to the reduced bandwidth and numerical integration effort, the overlapping finite elements can always exactly resolve the functions used as degrees of freedom, which renders the overlapping elements insensitive to mesh distortions.

The use of overlapping elements, which are formulated as the overlapped regions of individual elements, enables more effective meshing procedures because the mesh quality requirement is much relaxed. However, a conforming mesh is still needed. By considering the overlapping of conforming finite element meshes, a more general scheme – the method of overlapping finite element meshes – was proposed [8], and in this scheme elements from different meshes can overlap in any geometric form to further reduce the meshing effort. In the scheme of overlapping meshes, the complete analysis domain is discretized by several independent regular finite element meshes. A local compatible field is interpolated on each individual mesh using any existing compatible interpolation scheme. These local fields are finally assembled to form a continuous global interpolation. To do so, continuous weight functions are formulated upon the mesh overlay to represent the contributions of different meshes. Since these weight functions are designed to satisfy the partition of unity property, many desired properties, e.g. convergence and local enriching, of the interpolation can be derived. An effective implementation of this new scheme relies on the algorithms to compute the mesh overlay structure with reasonable computational cost, which were well studied by the community of computational geometry. Since each individual mesh governs the local solution accuracy, we use a low-order mesh for the interior region where a small solution gradient is expected and high-order meshes are spanned along the boundaries or near some locations of particular interest to resolve the boundary curvature and local stress concentrations.

These novel interpolation schemes play central roles in the AMORE paradigm, see the next section.

1.2 The AMORE paradigm

The AMORE (automatic meshing with overlapping and regular elements) paradigm is a general solution procedure for any CAD representations of engineering objects or models from a computerized scan [2, 3, 4, 5, 6, 7, 8]. In this solution approach, mostly undistorted low-order finite elements are used to discretize the interior part of the domain and the novel overlapping procedures are used to mesh the boundary regions.

Traditional finite elements are most effective in their undistorted configurations, among which 4-node quadrilateral elements (for two-dimensional problems) and 8-node hexahedral finite elements (for three-dimensional problems) are most preferred due to their efficiency, so these undistorted elements are used to discretize the main part (interior) of the domain with the element size determined by the geometric features and the requirement on solution accuracy. To mesh the boundary regions, the boundaries are discretized in such a way to neglect all deficiencies in the geometry. The remaining part of the domain is then meshed using novel schemes. In the case of overlapping elements, the boundary regions are meshed with distorted overlapping elements. Being insensitive to mesh distortions, these overlapping elements still lead to reasonable local solutions. In the case of overlapping meshes, boundary meshes are spanned along the discretized boundaries, and these meshes overlap with the interior regular mesh and with each other. Since overlapping is allowed, each mesh can be quite regular and therefore traditional finite elements can be used and demonstrate their optimal performance. In practical applications in solids and structures, these boundary meshes are chosen to have high-order interpolations, for the reasons given in the previous section.

1.3 Thesis outline

In this chapter, we introduce the main difficulty in the practical application of finite element methods. To tackle this difficulty, novel schemes featuring overlapping ele-

ments and overlapping meshes were proposed and their use in the AMORE paradigm is explained.

In Chapter 2, we introduce some related work in the effort of reducing meshing expense, e.g. the Chimera grids, meshless methods, the analytical trial function method, the generalized finite element method, Nitche's method, the fictitious domain method, etc.

In Chapter 3, the new quadrilateral overlapping elements are formulated. In addition, the boundary conditions, a coupling scheme between overlapping and regular elements, and an analysis on the mesh distortion sensitivity are presented.

In Chapter 4, the method of overlapping finite element meshes is formulated. Details are given on the construction of weight functions. And conditions for the solvability of discretized equations are introduced.

In Chapter 5, the proposed schemes are analyzed to give the error bounds and convergence rates. We discuss the effect of the overlapping sizes on the solution error using two numerical examples. A one-dimensional case is also studied to reveal a special error bound in the limit case.

In Chapter 6, the actual implementations of overlapping elements and overlapping meshes are introduced in details. Several simple problems are solved to illustrate the performance of the new methods. These new methods are also used in the solution of several more practical problems with AMORE to demonstrate their potential in general.

In Chapter 7, we summarize the main contributions and limitations of the current work. Based on these limitations, several future research directions are suggested.

THIS PAGE INTENTIONALLY LEFT BLANK

Chapter 2

Related Work

The idea of allowing "elements" or "cells" to overlap can also be found in the community of computational fluid mechanics, in which the Chimera grids and other overset grids have been proposed for finite difference methods and finite volume methods [14, 15, 16]. Just as the overlapping finite element meshes, these overset grids enable convenient local refinements near obstacles and boundaries, hence can well resolve the local solutions. Although the concepts look very similar to overlapping finite element meshes, the method of overlapping meshes is in essence different as we build in this method a global compatible field, which is not required in the discretizations using finite difference methods or finite volume methods.

For finite element methods, the issue of meshing has been addressed from multiple perspectives.

The method of finite spheres that is used to formulate local fields in the overlapping elements belongs to a large family of meshless methods, in which the global solution fields are constructed using scattered points [9, 10, 17, 18, 19, 20, 21, 22, 23, 24, 25, 26, 27, 28, 29]. Among many meshless methods, the main idea is almost the same but the implementations can vary, due to the choices of shape functions, quadrature schemes, etc. Since a conforming mesh is no longer needed, the discretization is much easier. However, to ensure solution stability without additional numerical stabilization and for a reasonable accuracy, the numerical integration in meshless methods is computationally expensive [10, 22, 23, 25, 26]. These methods are consequently not

widely used in engineering practice.

As we see for the overlapping elements, by formulating distortion insensitive interpolations, the meshing effort for a given accuracy can be much reduced. In the analytical trial function method, the interpolation is established upon some basic solutions of the underlying governing equation [30, 31, 32, 33, 34, 35]. Such interpolations can be exact as long as the exact solution is contained in the interpolation bases and the interpolation bases are to some degree independent of the element configuration. For this reason, elements based on this method show certain immunity to mesh distortions.

In the method of overlapping finite element meshes, the complete analysis domain is divided into subdomains. The similar idea is also seen in domain decomposition methods [36, 37]. Using domain decomposition techniques, the original problem is converted to coupled problems on these subdomains, which can be solved iteratively in a divide-and-conquer manner. As a result, such methods are very suitable for parallel machines. Although sharing some similarities, they are not the interpolation schemes that are being pursued.

The generalized finite element method [38, 39, 40], Nitsche's method [41, 42, 43, 44], and the fictitious domain method [45, 46] handle complex geometries in more direct ways. In the generalized finite element method, a larger regular mesh is spanned to cover the analysis domain and the interpolation is established based on this mesh, but the integration is only performed over the physical domain. The numerical integration is achieved using an adaptive scheme with fast remeshing. A similar idea was already proposed in Reference [47]. However, if the mesh overlaps the Dirichlet boundary, the solution accuracy can be poor because the essential boundary conditions are directly imposed by zeroing all dofs that have support overlapping the boundary. Overlapping meshes are also seen in Nitsche's scheme, but the overlapped regions are actually cut off to have non-matching meshes and the interface conditions are imposed via a penalty term. In the fictitious domain method, an extended variational problem on a larger domain that contains the physical domain is solved, and Lagrange multipliers are used to impose the original boundary conditions. These

methods address the issue of meshing, but they are not widely accepted in the engineering community for finite element analysis of solids and structures due to the loss of several valuable aspects of traditional finite element methods.

In the generalized finite element method, a local approximation for each small region of the analysis domain is first established using a linear combination of some basic functions, and then these local fields are assembled using a partition of unity [38, 39, 40]. Polynomials, harmonic functions, and some handbook functions (for approximating the solutions near corners, voids, and cracks) can be used as degrees of freedom for each local field. This method has similar features as the overlapping finite element method. However, the resulting stiffness matrices of the generalized finite element method are generally only symmetric positive semi-definite. Hence, special solvers are needed and bring extra computational expense, which makes the generalized finite element method hardly effective or even applicable to large-scale engineering problems [39, 40].

The idea of using special functions as local enrichments for finite element interpolations can be seen in many studies, e.g. the singularity enrichment for crack tip elements [48], the ovalization enrichment for pipe elements [49], the discontinuity enrichment for strain localization [50], and the discontinuity and singularity enrichments in the extended finite element method [51, 52]. The schemes all aim to enrich the interpolations and decrease the meshing effort, so that better solutions can be obtained. Hence there are similarities among all these procedures. However, for engineering problems, the details of enriching (i.e. what are the basic functions and the enriching functions, how are the enrichments assembled to form a global field, and how are the formulations implemented) are extremely important. These details decide whether the scheme is stable, accurate, and effective for engineering analysis, and whether the scheme will be used in engineering practice.

The schemes of overlapping finite elements and overlapping meshes focused upon in this thesis are novel procedures based on valuable features seen in the above surveyed schemes, and these approaches enable stable, accurate, and computationally effective engineering solutions.

THIS PAGE INTENTIONALLY LEFT BLANK

Chapter 3

Quadrilateral Overlapping Finite Elements

In this chapter, we present the formulation of new quadrilateral overlapping finite elements which are formulated as the overlapped regions of polygonal elements [6]. The new interpolation scheme can be regarded as a combination of the traditional finite element methods and the method of finite spheres. Inheriting advantages from both traditional interpolations and meshless interpolations, the new elements are much more effective than meshless methods. A schematic description of the idea can be seen in Figure 3-1. A local interpolation is established for each polygonal element, e.g. D_I, using the method of finite spheres (disks in two-dimensional analyses) with the centers of the disks at the nodes. The final displacement field in each quadrilateral is then the weighted average of the four method-of-finite-spheres fields on the polygonal elements corresponding to the four nodes of the element. Traditional shape functions are used as the weight functions. These concepts have been used to formulate the triangular overlapping finite elements [5, 7], and are modified here to formulate the new 4-node quadrilateral overlapping finite elements.

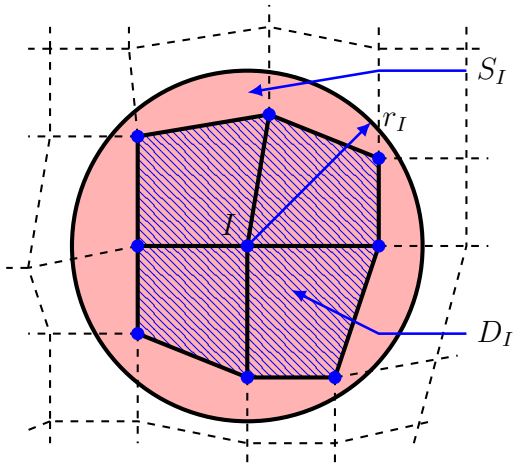

(a) A typical 9-node polygonal element D_I and its local support S_I

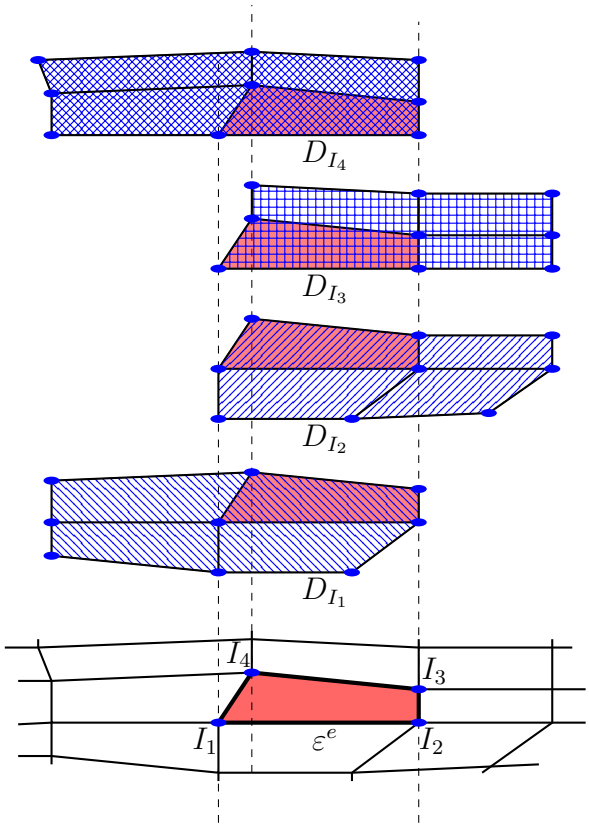

(b) A typical quadrilateral element obtained as the overlapped region ε^e

Figure 3-1: A 4-node quadrilateral overlapping finite element

3.1 The interpolation

We consider a well-posed problem in two-dimensional linear elasticity and introduce the interpolation of one displacement component u (e.g. the x-displacement). This interpolation technique can of course be used for other suitable problems as well.

The final interpolation in a quadrilateral element is given by

$$u(\mathbf{x}) = \sum_{I=1}^{4} \rho_I(\mathbf{x}) u_I(\mathbf{x}) \tag{3.1}$$

where $\rho_I(\mathbf{x})$ is the new interpolation function to be detailed in subsequent sections. In traditional finite element analysis, u_I is the nodal value of the field u at node I. However, in the new scheme, u_I is a function and usually a polynomial function given in the local Cartesian coordinate system $\mathbf{x} = (x, y)$ at node I:

$$u_I(\mathbf{x}) = a_{I1} + a_{I2}x + a_{I3}y + \cdots \tag{3.2}$$

We suggest using the quadratic basis, i.e. $u_I(\mathbf{x}) = a_{I1} + a_{I2}x + a_{I3}y + a_{I4}x^2 + a_{I5}xy + a_{I6}y^2$. Since local Cartesian coordinates are used, $a_{I1} = u_I(\mathbf{0})$. In following sections, we will see that ρ_I is a cubic function in each of the isoparametric coordinates (r, s). We note that cubic or even higher-order bases might also be used. In these cases, additional studies would be needed to assess the computational effort required for a given accuracy. For special problems, other suitable functions can be added into the nodal basis as interpolation enrichments, e.g. trigonometric functions can be used for wave propagation problems [13].

It can be seen from Equation 3.1 that the bandwidth structure due to nodal coupling is similar to that in traditional finite element analysis, while in many meshless methods the bandwidth is very large. As a result, the discretization using Equation 3.1 is computationally effective from the perspective of solution effort, see also Reference [5].

The expression for the new shape functions in Equation 3.1 can be formulated

from (see Figure 3-1)

$$u = \sum_{I=1}^{4} h_I \psi_I \tag{3.3}$$

where h_I is the traditional shape function for a 4-node quadrilateral element, and ψ_I is the local interpolation function that we establish in D_I using the method of finite spheres. The final field u in each element is formulated as a weighted average of four local fields ψ_I. Since the traditional interpolation functions h_I $(I = 1, 2, 3, 4)$ are continuous and vanish outside D_I, the final field u in Equation 3.3 is compatible provided each function ψ_I is continuous in the corresponding polygonal element D_I. The construction of ψ_I is detailed in following sections.

3.2 The function ψ_I

To construct the function ψ_I for each node I, we consider the polygon formed by all basic elements (triangles and quadrilaterals) coupling into node I. This polygon is formally regarded as a polygonal element and a typical polygonal element D_I is shown in Figure 3-2. The support set N_I for node I is defined as the set of all neighboring nodes including node I. The support radius r_I is defined as the radius of a disk that contains N_I.

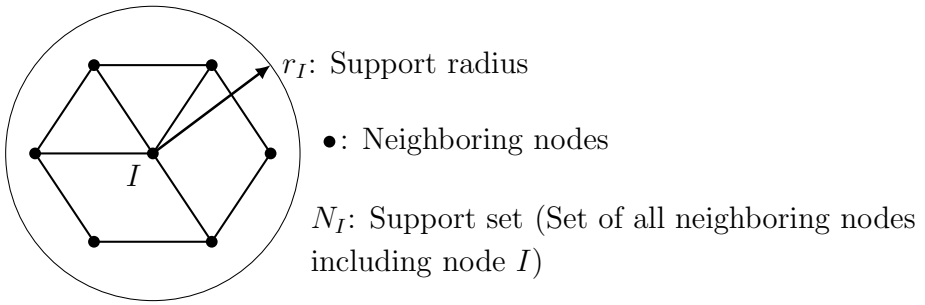

Figure 3-2: A polygonal element and its local support

We suggest using

$$r_I = \max_{J \in N_I} \|\mathbf{x}_I - \mathbf{x}_J\| \tag{3.4}$$

which is the minimum support radius, and we also define another radius for each node by

$$r_I^* = \min_{J \in N_I, J \neq I} \|\mathbf{x}_I - \mathbf{x}_J\| \tag{3.5}$$

The ratio r_I/r_I^* will be used as a local indicator of the mesh regularity. With r_I given the local field ψ_I is expressed as

$$\psi_I = \sum_{K=1}^{4} \phi_K^I(\mathbf{x}) u_K(\mathbf{x}) \tag{3.6}$$

where we use for ϕ_K^I the Shepard functions, but interpolated over the 4-node element of interest in such a way to provide compatibility and to reduce the numerical integration effort and the solution effort. Of course, the support radii are used in the expression of ϕ_K^I.

The Shepard functions are widely used for interpolations of scattered data, and they also play an important role in meshless methods. Since these are non-polynomial functions in the form of a quotient of some weight functions, their use in meshless techniques, e.g. the method of finite spheres, is computationally expensive due to the need of a very large number of quadrature points in the numerical integration [9]. Therefore the Shepard functions are further interpolated using isoparametric polynomials to improve the computational efficiency.

3.3 The interpolation of Shepard functions

We use some mid-edge nodes (see Figure 3-3) to obtain an accurate polynomial representation of the Shepard function in the isoparametric coordinates:

$$\tilde{\phi}_J^I(\mathbf{x}) = \sum_{i=1}^{8} \hat{h}_i(\mathbf{x}) \hat{\phi}_{Ji}^I \tag{3.7}$$

where $\tilde{\phi}_J^I(\mathbf{x})$ is the approximation of the Shepard function, $\hat{\phi}_{Ji}^I$ $(i = 1, \ldots, 8)$ are constant coefficients to be determined, and $\hat{h}_i(\mathbf{x})$ $(i = 1, \ldots, 8)$ are the traditional shape functions of an 8-node quadrilateral element. A similar interpolation was used

to formulate triangular overlapping elements [5].

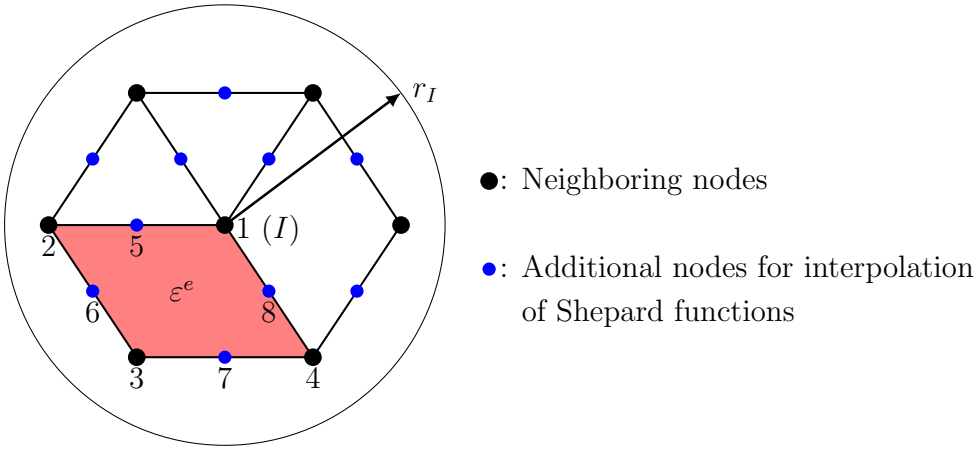

Figure 3-3: Nodal positions (nodes 1 – 4) of the Shepard functions and nodes used for interpolation of Shepard functions (nodes 1 – 8) for the quadrilateral element ε^e

These coefficients $\hat{\phi}^I_{Ji}$ $(i = 1, \ldots, 8)$ are designed to satisfy the following criteria:

1. The interpolated Shepard functions should result in a compatible final field. To satisfy this condition, ϕ^I_J (or equivalently $\tilde{\phi}^I_J$) needs to be continuous in the polygonal element D_I.

2. The interpolated Shepard functions should satisfy the partition of unity property, i.e. $\sum_J \tilde{\phi}^I_J = 1$. As a result, the convergence and the distortion insensitivity can be concluded.

3. The element interpolation should involve only the four weight functions (see below) and the four nodal polynomials at the four corner nodes of the quadrilateral element, in order to reduce the bandwidth.

The coefficients given in Table 3.1 satisfy all these conditions, where W_J is the quartic spline weight function:

$$W_J(\mathbf{x}) = \begin{cases} 1 - 6s_J^2 + 8s_J^3 - 3s_J^4, & 0 \le s_J < 1 \\ 0, & s_J \ge 1 \end{cases} \tag{3.8}$$

Table 3.1: Interpolation of the Shepard functions on a quadrilateral element (see Figure 3-3)

$\tilde{\phi}_1^I = \sum_{i=1}^{8} \hat{h}_i \hat{\phi}_{1i}^I$			
$\hat{\phi}_{11}^I$	$\hat{\phi}_{12}^I$	$\hat{\phi}_{13}^I$	$\hat{\phi}_{14}^I$
1	$\frac{W_1}{W_1+W_2}\Big\|_{\mathbf{x}_2}$	0	$\frac{W_1}{W_1+W_4}\Big\|_{\mathbf{x}_4}$
$\hat{\phi}_{15}^I$	$\hat{\phi}_{16}^I$	$\hat{\phi}_{17}^I$	$\hat{\phi}_{18}^I$
$\frac{W_1}{W_1+W_2}\Big\|_{\mathbf{x}_5}$	$\frac{W_1}{W_1+W_2+W_3}\Big\|_{\mathbf{x}_6}$	$\frac{W_1}{W_1+W_3+W_4}\Big\|_{\mathbf{x}_7}$	$\frac{W_1}{W_1+W_4}\Big\|_{\mathbf{x}_8}$
$\tilde{\phi}_2^I = \sum_{i=1}^{8} \hat{h}_i \hat{\phi}_{2i}^I$			
$\hat{\phi}_{21}^I$	$\hat{\phi}_{22}^I$	$\hat{\phi}_{23}^I$	$\hat{\phi}_{24}^I$
0	$\frac{W_2}{W_1+W_2}\Big\|_{\mathbf{x}_2}$	0	0
$\hat{\phi}_{25}^I$	$\hat{\phi}_{26}^I$	$\hat{\phi}_{27}^I$	$\hat{\phi}_{28}^I$
$\frac{W_2}{W_1+W_2}\Big\|_{\mathbf{x}_5}$	$\frac{W_2}{W_1+W_2+W_3}\Big\|_{\mathbf{x}_6}$	0	0
$\tilde{\phi}_3^I = \sum_{i=1}^{8} \hat{h}_i \hat{\phi}_{3i}^I$			
$\hat{\phi}_{31}^I$	$\hat{\phi}_{32}^I$	$\hat{\phi}_{33}^I$	$\hat{\phi}_{34}^I$
0	0	1	0
$\hat{\phi}_{35}^I$	$\hat{\phi}_{36}^I$	$\hat{\phi}_{37}^I$	$\hat{\phi}_{38}^I$
0	$\frac{W_3}{W_1+W_2+W_3}\Big\|_{\mathbf{x}_6}$	$\frac{W_3}{W_1+W_3+W_4}\Big\|_{\mathbf{x}_7}$	0
$\tilde{\phi}_4^I = \sum_{i=1}^{8} \hat{h}_i \hat{\phi}_{4i}^I$			
$\hat{\phi}_{41}^I$	$\hat{\phi}_{42}^I$	$\hat{\phi}_{43}^I$	$\hat{\phi}_{44}^I$
0	0	0	$\frac{W_4}{W_1+W_4}\Big\|_{\mathbf{x}_4}$
$\hat{\phi}_{45}^I$	$\hat{\phi}_{46}^I$	$\hat{\phi}_{47}^I$	$\hat{\phi}_{48}^I$
0	0	$\frac{W_4}{W_1+W_3+W_4}\Big\|_{\mathbf{x}_7}$	$\frac{W_4}{W_1+W_4}\Big\|_{\mathbf{x}_8}$

where $s_J = d_J(\mathbf{x})/r_J$ is the scaled distance, and $d_J(\mathbf{x})$ is the Euclidean distance between the point $\mathbf{x}$ and the node J. The weight functions of two neighboring nodes can be seen in Figure 3-4.

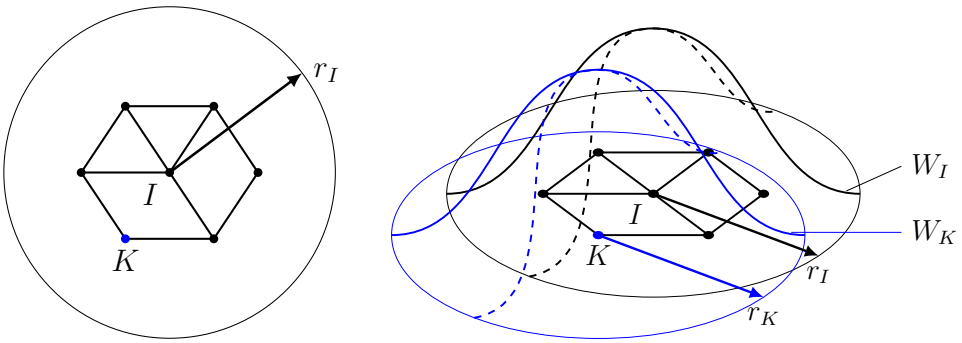

Figure 3-4: Two weight functions

To take mesh distortions into consideration, and noticing that r_I/r_I^* measures the local mesh distortion around node I, the final interpolated Shepard function is given by

$$\phi_J^I = \frac{\sqrt{r_I^*}}{\sqrt{r_I} + \sqrt{r_I^*}}\tilde{\phi}_J^I + \frac{\sqrt{r_I}}{\sqrt{r_I} + \sqrt{r_I^*}}\delta_{IJ} \tag{3.9}$$

where r_I and r_I^* are the radii defined in Equations 3.4 and 3.5, respectively, and δ_{IJ} is the Kronecker delta. If the local mesh near node I is severely distorted, we have $r_I \gg r_I^*$, which yields $\phi_J^I \approx \delta_{IJ}$ and $\psi_I \approx u_I(\mathbf{x})$. It follows that the formulation (locally) reduces to using finite elements with interpolation covers [5, 53]. The elements with interpolation covers can exactly represent polynomial fields that are one order higher than the nodal basis functions, hence better local accuracy can be achieved. However, quadrilateral finite elements enriched by interpolation covers may lead to only positive semi-definite stiffness matrices due to the linear dependency of interpolation functions. For this reason, a reasonable conditioning of the formulation is achieved using the weight coefficients in Equation 3.9.

We see from Equations 3.1, 3.3 and 3.6 that

$$\rho_I = \sum_{J=1}^{4} h_J \phi_I^J \tag{3.10}$$

Having contributions from both traditional and meshless interpolations, the new shape functions combine valuable aspects of mesh-dependent and mesh-independent methods. As a result, the new displacement interpolation gives accurate and distortion insensitive numerical solutions, which is illustrated in the analyses and numerical results in Section 3.6, Section 5.2, and Section 6.1.

3.4 The Dirichlet boundary conditions

In the overlapping finite element method, natural boundary conditions are imposed weakly as in traditional finite element methods [1]. The formulation is a direct result of the principle of virtual work. Due to the special form of the interpolation, the Dirichlet boundary conditions are imposed using the technique of interpolation covers in local coordinates [4, 53].

We consider here two different cases, as shown in Figure 3-5. If the boundary is smooth, a local coordinate system can be established at a boundary node I_4, with one axis along the boundary and another perpendicular to the boundary. If the boundary has a sharp corner, the local axes are oriented along the edges, and in such a case we have a local affine coordinate system instead of a local Cartesian coordinate system.

In the first case, assuming the $I_3 - I_4$ edge is constrained (see Figure 3-5a), we use

$$\psi_{I_4}(r,s) = u_{I_4} = a_{I_4 1} + a_{I_4 2} r + a_{I_4 3} rs + \text{higher-order terms} \tag{3.11}$$

and similarly for ψ_{I_3}. Thus, the local fields ψ_{I_3} and ψ_{I_4} become constant along the constrained edge, where $r = 0$. The final interpolation (see Equation 3.3) is then constrained as desired. Of course, such constraints are only exact if the boundary is flat, otherwise discretization errors occur.

In the second case, a special ψ function is constructed upon the local affine coordinates at the corner node. In Figure 3-5b, the edges of a corner node I_4 are constrained, and we use

$$\psi_{I_4} = u_{I_4} = a_{I_4 1} + a_{I_4 2} rs + \text{higher-order terms} \tag{3.12}$$

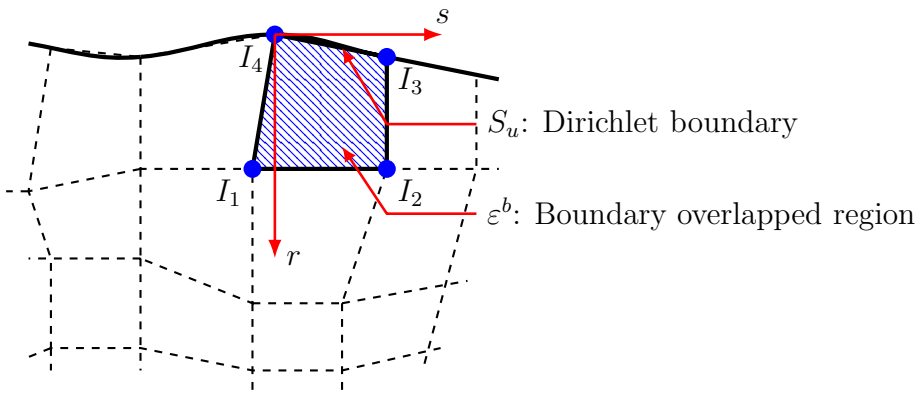

(a) Smooth boundary

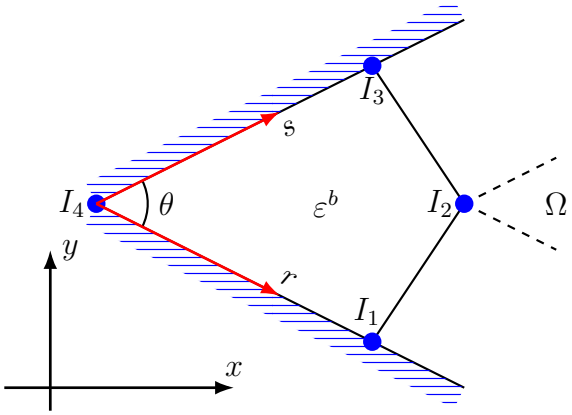

(b) Corner node

Figure 3-5: The local coordinate systems

where the affine coordinates r and s are oriented along the corner edges. It is then seen that if $r = 0$ or $s = 0$, ψ_{I_4} becomes a constant $a_{I_4 1}$.

It can be seen that the new shape functions already satisfy the Kronecker-delta property (see Section 5.2), hence the displacement boundary conditions can actually be imposed by prescribing nodal polynomials instead of local fields. However, the special boundary interpolation proposed in this section gives slightly better numerical solutions.

3.5 The coupling between overlapping elements and traditional elements

The coupling between overlapping elements and traditional elements plays a key role in the AMORE paradigm as these two types of elements are used in different parts of the analysis domain. Here we introduce a continuous coupling interpolation.

In overlapping elements, each node corresponds to an unknown polynomial function. A coupling element touches both overlapping and traditional elements, so it has both overlapping element nodes and finite element nodes, see Figure 3-6.

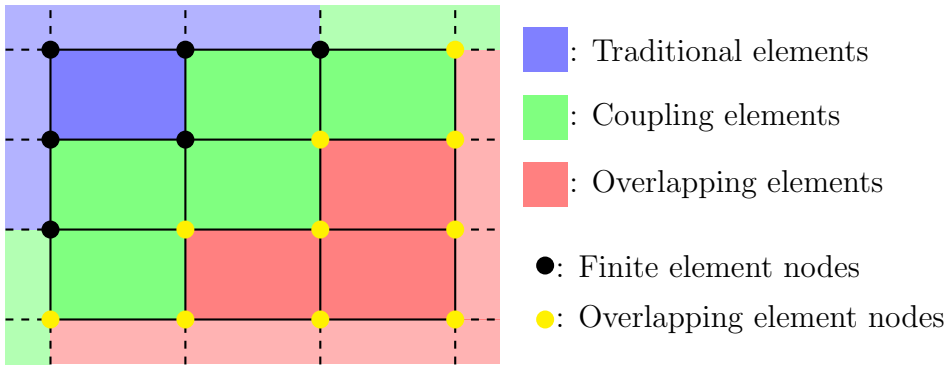

Figure 3-6: Coupling between overlapping elements and finite elements

To obtain a continuous coupling interpolation, it is sufficient to require the local field ψ_I to be continuous in the corresponding polygonal element D_I. If node I is a

node of a coupling element, the function ψ_I is given by

$$\psi_I = \begin{cases} \alpha, & I \in \Lambda_{\mathrm{FE}} \\ \sum_{K\in\Lambda_{\mathrm{OFE}}} \phi_K^I u_K + \sum_{K\in\Lambda_{\mathrm{FE}}} \phi_K^I \alpha, & I \in \Lambda_{\mathrm{OFE}} \end{cases} \tag{3.13}$$

where Λ_{FE} and Λ_{OFE} are the set of finite element nodes in this element and the set of overlapping element nodes in this element, respectively. The function α is defined by

$$\alpha = \sum_{K\in\Lambda_{\mathrm{OFE}}} h_K a_{K1} + \sum_{K\in\Lambda_{\mathrm{FE}}} h_K u_K \tag{3.14}$$

where a_{K1} is the constant part of the nodal polynomial at node K, and h_K is the bilinear shape function in 4-node finite elements.

The function ψ_I is actually consistent with the interpolations of pure overlapping elements and pure finite elements. If $\Lambda_{\mathrm{FE}} = \varnothing$, Equation 3.13 degenerates to Equation 3.6. On the other hand, if $\Lambda_{\mathrm{OFE}} = \varnothing$, the final interpolation becomes the isoparametric interpolation since $\sum_K h_K = 1$.

To see the continuity of the coupling interpolation, the continuity of ψ_I in D_I can be verified using the coefficients listed in Table 3.1. Indeed, on an element edge $I - J$, the local fields ψ_I and ψ_J are unambiguously determined by the nodal unknowns u_I and u_J. Hence, the final interpolation is continuously defined.

It is important to note that the coupling interpolation is able to reproduce an arbitrary linear field. Let $p_1(\mathbf{x})$ be a linear field. We simply assign nodal unknowns by

$$u_I = \begin{cases} p_1(\mathbf{x}), & I \in \Lambda_{\mathrm{OFE}} \\ p_1(\mathbf{x}_I), & I \in \Lambda_{\mathrm{FE}} \end{cases} \tag{3.15}$$

Then, $\alpha = p_1(\mathbf{x})$ and the final interpolation reproduces the linear field. It is therefore seen that the coupling scheme passes the constant stress patch tests. We show in the next section that the overlapping element interpolation is able to reproduce even higher-order polynomial fields, which is an important reason why the overlapping elements are less sensitive to mesh distortions [1, 54].

3.6 The mesh distortion sensitivity and convergence rates

Assume the kth order basis is used in overlapping elements. Given an arbitrary kth order polynomial function p_k, we can choose all nodal polynomials to be p_k and the final interpolation in an element becomes

$$u = \sum_{I=1}^{4} \rho_I p_k \tag{3.16}$$

The new shape functions ρ_I still satisfy the partition of unity property as $\sum_{I=1}^{4} \rho_I = \sum_{I=1}^{4} \sum_{J=1}^{4} h_J \phi_I^J = 1$, where we use $\sum_{I=1}^{4} \phi_I^J = 1$. Therefore, $u = p_k$ holds over the analysis domain. Note that this result does not rely on any assumption on the mesh regularity. As a result, the proposed elements show less mesh distortion sensitivity than traditional high-order finite elements, especially elements in the Serendipity family [1, 54].

Since the overlapping elements with the kth order basis equipped can exactly solve any kth order polynomial, it is naturally expected that the corresponding convergence rate is k. Indeed, assuming that the exact solution is smooth enough, the kth order basis is used, and the mesh is reasonably regular, the convergence rate with respect to the energy norm is k. A detailed discussion on the convergence is given in Chapter 5.

3.7 The use of overlapping elements in AMORE

The AMORE paradigm aims to enable efficient and automatic meshing of a geometry obtained by any CAD program or by a computerized scan. Overlapping elements play a key role as they are insensitive to mesh distortions. They can be used in areas that are difficult to mesh with traditional elements.

The use of overlapping elements in AMORE involves the following steps:

1. The analysis domain is covered by a Cartesian grid. After this step, the interior of the analysis domain is divided into regular cells.

2. The boundaries are discretized. The cells located outside the domain or cutting the boundaries are deleted. The discretized boundaries work as seeds for discretizing the boundary regions.

3. The remaining Cartesian cells are converted into traditional elements.

4. Now the boundary regions are empty. We can fill in these regions using overlapping elements based on the discretized boundaries.

In the last step, the boundary regions can be meshed easily with a relaxed regularity requirement since overlapping elements can still perform well in distorted configurations. In the solution stage, the program automatically identifies all coupling elements and uses the coupling interpolation upon them. Some coupling elements can actually become pure overlapping elements. As mentioned in Section 3.5, the coupling interpolation then automatically degenerates into the overlapping interpolation.

A numerical example illustrating the use of overlapping elements in AMORE is given in Section 6.1.5.

Chapter 4

Overlapping Finite Element Meshes

In the previous chapter, the overlapping finite element is formulated as the overlapped region of several polygonal elements. Although attractive aspects of meshless methods and traditional elements are adopted, conforming meshes are still required throughout the solution procedure.

To further reduce the meshing effort, we present a method of overlapping finite element meshes [8]. In this new scheme, elements from different meshes can overlap freely, as shown in Figure 4-1. The complete analysis domain is first divided into several subdomains, each of which is then meshed independently. Even though the whole analysis domain may be of complex shape, since subdomains are allowed to overlap, each of them can be of regular shape and hence discretized easily using a regular conforming mesh. For each subdomain and the mesh on it, we can use any compatible interpolation as the local field. The final stage is to combine these interpolations together to form a global compatible field. As in the formulation of quadrilateral overlapping elements, we establish continuous weight functions as a partition of unity for the analysis domain according to the domain decomposition. The weighted average of local fields is then the final interpolation.

To render the scheme effective, the construction of weight functions must be achieved with reasonable computational effort. We use in this thesis the plane sweep algorithm to calculate the mesh overlay structure and build upon the mesh overlay the weight functions.

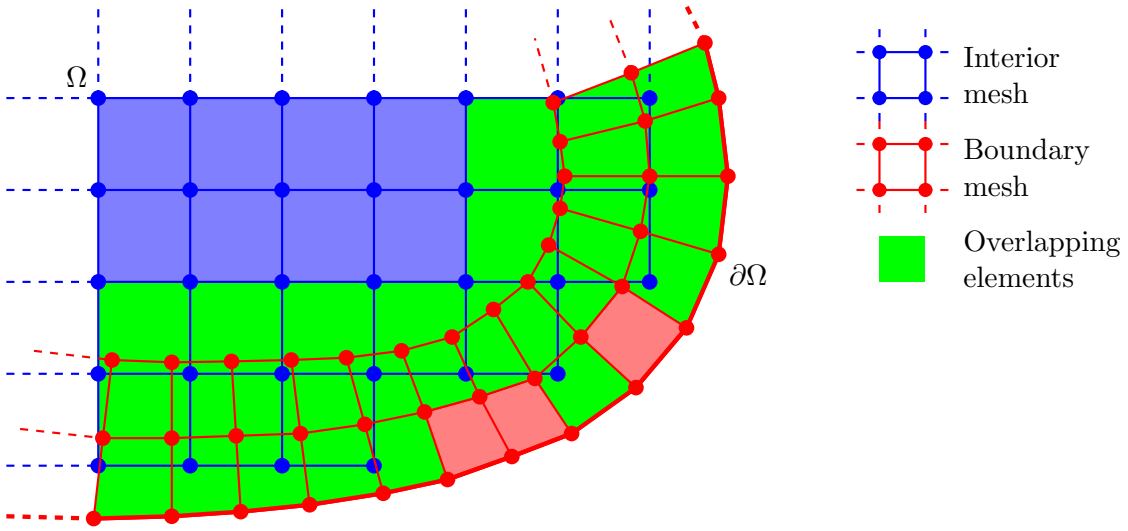

Figure 4-1: Overlapping of meshes

In the following sections, we introduce the method of overlapping finite element meshes for static problems in two-dimensional linear elasticity. The technique is essentially an interpolation scheme and can be readily used for other problems.

4.1 The domain decomposition

We first introduce the notations used. The analysis domain is denoted by Ω, which is decomposed into several subdomains Ω_i $(i = 1, \ldots, m)$. These subdomains overlap and satisfy $\Omega = \cup_{i=1}^{m} \Omega_i$. The overlapped regions cannot degenerate into a curve because each subdomain is regarded as an open set which does not contain its boundary. We will also see that the minimum overlapping size (see Section 5.3) enters the error bound so it cannot be too small compared with the element sizes. Although theoretically there is still no guarantee of convergence as the overlapped regions degenerate, we are interested in such a limit case where the overlapping meshes become non-matching meshes. A discussion is given in Section 5.3.

The boundary of the analysis domain is denoted by $\partial\Omega$, and, similarly, $\partial\Omega_i$ is the boundary of the subdomain Ω_i. The boundary $\partial\Omega_i$ can be divided into the interior

part $\Gamma_i^* = \partial\Omega_i \cap \Omega$ and the exterior part $\Gamma_i = \partial\Omega_i \cap \partial\Omega$. This decomposition is used for formulating weight functions.

An example domain decomposition can be seen in Figure 4-2, in which the analysis domain is decomposed into three subdomains. In most practical problems, the number of meshes need not exceed three. Actually, each single mesh can be disconnected, which means that several connected meshes can be combined and regarded as a single mesh, as long as these meshes do not overlap with each other. We will see examples of disconnected meshes in Section 6.2. The conforming mesh on subdomain Ω_i is denoted by $\mathcal{T}_i$. Since each subdomain is discretized independently, each mesh has its own nodes and degrees of freedom (dofs). In other words, two nodes from different meshes may have the same coordinates but they never share dofs.

The meshes of the subdomains form a mesh overlay for the analysis domain. As mentioned in the beginning of this chapter, we use the information of the mesh overlay to establish continuous weight functions corresponding to different meshes. The efficiency of this process relies on the algorithms and data structures used for calculating and storing the mesh overlay. We suggest here using a modified version of the plane sweep algorithm [55, 56]. The algorithms used are also briefly introduced in Appendix B.

4.2 The weight functions

If an element is not overlapping with other meshes, we want the final interpolation in this element to be identical to the local field. The weight functions are designed to meet this property and represent the contributions of different meshes. Let $w_i(\mathbf{x})$ $(i = 1, \ldots, m)$ be the weight functions. The following conditions should be satisfied:

1. The weight functions are continuous and non-negative over the analysis domain.
2. The weight function w_i vanishes outside the corresponding subdomain Ω_i.
3. The partition of unity property is satisfied by weight functions, i.e. $\sum_{i=1}^{m} w_i(\mathbf{x}) = 1$ holds on Ω.

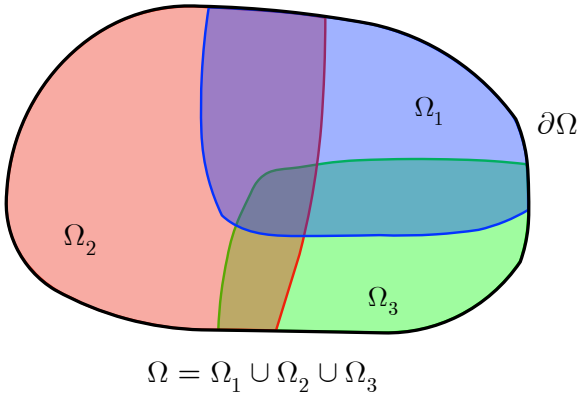

(a) Subdomains

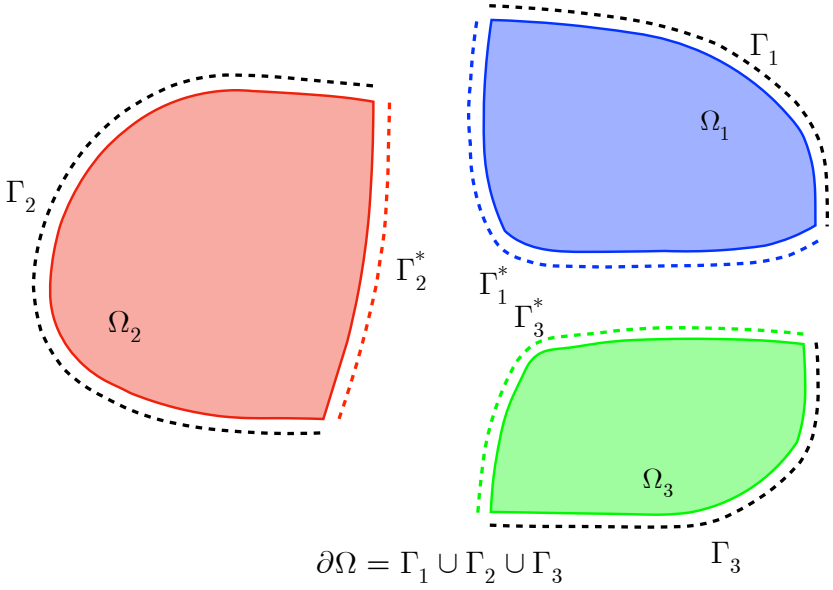

(b) Boundaries of subdomains

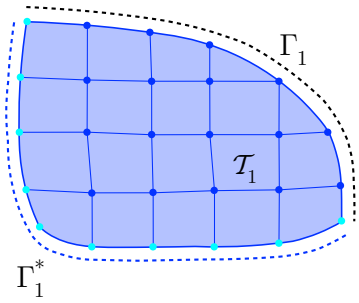

(c) Mesh on a subdomain (the function P_1 is assigned 0 at cyan nodes and 1 at blue nodes)

Figure 4-2: An example of the domain decomposition, $m = 3$

Assume on each mesh $\mathcal{T}_i$ a local field $\mathbf{u}_i$ is interpolated, the final interpolation is then the weighted average $\sum_{i=1}^{m} w_i \mathbf{u}_i$. Since the weight functions are continuous and satisfy the partition of unity property, the final interpolation is continuous and can exactly solve any linear field as long as each local field $\mathbf{u}_i$ is continuous (in Ω_i) and contains an arbitrary linear field. In other words, the constant stress patch tests are passed and the convergence is concluded.

Now we suggest a formulation of the weight functions using the mesh overlay structure. On the subdomain Ω_i, we construct a function $P_i(\mathbf{x}) = \sum_j h_j^i(\mathbf{x}) p_j^i$, where h_j^i is the shape function used in low-order finite elements, j is a node of the mesh $\mathcal{T}_i$, and p_j^i is the nodal weight at the node j. We use here low-order shape functions, e.g. bilinear shape functions for quadrilateral elements and linear shape functions for triangular elements, to ensure that the function P_i is non-negative if all nodal weights are chosen to be non-negative. Since w_i is required to be continuous and vanish outside its subdomain, we assign $p_j^i = 0$ if the node j is on the closure of Γ_i^*. All other nodal values p_j^i are assigned 1, as shown in Figure 4-2c. It can be seen that the functions P_i $(i = 1, \ldots, m)$ now satisfy the first two conditions. The weight functions can then be obtained by normalizing P_i:

$$w_i(\mathbf{x}) = \frac{\alpha_i P_i(\mathbf{x})}{\sum_j \alpha_j P_j(\mathbf{x})} \tag{4.1}$$

where α_i $(i = 1, \ldots, m)$ are constants used in the actual implementation. In the present scheme, the first mesh consisting of regular 4-node finite elements is used to discretize the interior domain, and higher-order elements are used in other meshes to resolve the boundary stress concentrations and the boundary curvature. We therefore use $\alpha_1 = 1$ and $\alpha_2 = \cdots = \alpha_m = 9$ as the interpolation can put more weight on the higher-order interpolation on an overlapped region.

In a reasonable mesh, P_i is strictly positive in Ω_i. Since $\Omega = \cup_{i=1}^{m} \Omega_i$, $\sum_i \alpha_i P_i > 0$ in the analysis domain Ω and the weight functions are well defined in Ω. We will introduce an example of invalid meshes in Section 4.5, where P_i is not strictly positive in Ω_i. Such invalid meshes should of course be avoided and the meshes can

be easily checked before the solution process can continue. We note that such an invalid mesh will not occur if the mesh is reasonably fine. In addition, we assume the weight functions are well defined at all boundary nodes. This assumption actually corresponds to non-zero overlapping sizes, see Section 5.3.

The weight functions defined in Equation 4.1 are rational functions, which may lead to expensive numerical integration of the stiffness matrix. In the actual implementation, we further interpolate the weight functions over triangles by linear functions, see Section 6.2. The re-interpolation allows for more effective numerical integration while all requirements for w_i $(i = 1, \ldots, m)$ are still satisfied.

4.3 The interpolation

On each subdomain Ω_i and the mesh $\mathcal{T}_i$, we can use any compatible interpolation technique to obtain a local field $\mathbf{u}_i(\mathbf{x})$, e.g. the isoparametric interpolations [1], the finite elements enriched by interpolation covers [53], and the overlapping finite elements [2, 3, 4, 5, 6, 7]. We use here the traditional isoparametric interpolations for the sake of simplicity. Let

$$\mathbf{u}_i(\mathbf{x}) = \mathbf{H}_i(\mathbf{x})\mathbf{q}_i \tag{4.2}$$

be the local interpolation on subdomain Ω_i, where $\mathbf{H}_i$ is the corresponding shape function matrix, and $\mathbf{q}_i$ is a vector of degrees of freedom. The final interpolation is the weighted average of local fields, i.e.

$$\mathbf{u}(\mathbf{x}) = \sum_{i=1}^{m} w_i(\mathbf{x})\mathbf{u}_i(\mathbf{x}) = \sum_{i=1}^{m} w_i(\mathbf{x})\mathbf{H}_i(\mathbf{x})\mathbf{q}_i \tag{4.3}$$

whence we have the strain interpolation

$$\boldsymbol{\varepsilon}(\mathbf{x}) = \sum_{i=1}^{m} \mathbf{B}_i(\mathbf{x})\mathbf{q}_i = \begin{bmatrix} \mathbf{B}_1 & \cdots & \mathbf{B}_m \end{bmatrix} \begin{Bmatrix} \mathbf{q}_1 \\ \vdots \\ \mathbf{q}_m \end{Bmatrix} \tag{4.4}$$

with

$$\mathbf{B}_i = \begin{bmatrix} \frac{\partial}{\partial x} & 0 \\ 0 & \frac{\partial}{\partial y} \\ \frac{\partial}{\partial y} & \frac{\partial}{\partial x} \end{bmatrix} [w_i(\mathbf{x})\mathbf{H}_i(\mathbf{x})] \tag{4.5}$$

The stiffness matrix is then given by

$$\mathbf{K} = \int_\Omega \begin{bmatrix} \mathbf{B}_1 & \cdots & \mathbf{B}_m \end{bmatrix}^\top \mathbf{C} \begin{bmatrix} \mathbf{B}_1 & \cdots & \mathbf{B}_m \end{bmatrix} \mathrm{d}\Omega \tag{4.6}$$

where $\mathbf{C}$ is the elastic stress-strain matrix. The stiffness matrix adopts a block structure $\mathbf{K} = [\mathbf{K}_{ij}]$ with

$$\mathbf{K}_{ij} = \int_\Omega \mathbf{B}_i^\top \mathbf{C} \mathbf{B}_j \mathrm{d}\Omega = \int_{\Omega_i \cap \Omega_j} \mathbf{B}_i^\top \mathbf{C} \mathbf{B}_j \mathrm{d}\Omega \tag{4.7}$$

where we use the fact that $\mathbf{B}_i$ vanishes outside Ω_i.

Since the displacement interpolation is only piecewise smooth, the integrand of the stiffness matrix is piecewise defined and piecewise continuous on the mesh overlay. The discontinuity makes the numerical integration much more challenging than that of conventional finite elements. Instead of integrating over each single element, we now need to integrate over each polygon induced by the overlapping meshes. To do so, we first establish the geometric structure of the mesh overlay and then triangulate the polygons in the overlapped regions. Quadrature schemes for triangles can then be used [1, 57, 58]. A detailed discussion of the numerical integration is given in Section 6.2.

4.4 The boundary conditions

We consider here the common displacement boundary conditions and force boundary conditions. On the displacement boundary S_u, usually the displacement or a component of the displacement is prescribed. In such cases, we require each local field to satisfy the same constraints if the corresponding subdomain touches S_u. The final interpolation will then automatically satisfy the given displacement boundary

conditions since the weight functions form a partition of unity.

The force boundary conditions are imposed weakly via the variational form, or the principle of virtual work, i.e.

$$\begin{bmatrix} \delta\mathbf{q}_1 \\ \vdots \\ \delta\mathbf{q}_m \end{bmatrix}^\top \mathbf{F} = \int_\Omega \delta\mathbf{u} \cdot \mathbf{b} \mathrm{d}\Omega + \int_{S_f} \delta\mathbf{u} \cdot \mathbf{f} \mathrm{d}S + \sum_c \delta\mathbf{u}(\mathbf{x}_c) \cdot \mathbf{P}_c \tag{4.8}$$

where $\mathbf{F}$ is the vector of equivalent nodal forces, δ is the variational symbol, $\mathbf{b}$ is the vector of external body forces, S_f is the force boundary, $\mathbf{f}$ is the vector of boundary tractions, and $\mathbf{P}_c$ denotes a concentrated external force at point $\mathbf{x}_c$. The virtual displacement can be directly obtained from Equation 4.3:

$$\delta\mathbf{u}(\mathbf{x}) = \sum_{i=1}^{m} w_i(\mathbf{x}) \mathbf{H}_i(\mathbf{x}) \delta\mathbf{q}_i \tag{4.9}$$

Since several meshes may overlap at a location, an external force can contribute to several meshes at one time as can be readily seen from the above equations.

4.5 The solvability and convergence

Direct sparse solvers for symmetric positive definite systems are usually preferred in the solution of problems in solid mechanics. In this section, we analyze the conditions for the stiffness matrix to be symmetric positive definite after imposing essential boundary conditions, and briefly introduce the convergence rate of the method of overlapping meshes.

For static problems in linear elasticity, the bilinear form of the variational problem is bounded and coercive, provided that the material parameters and displacement boundary conditions are proper. As a result, solution to the variational problem always exists and is unique [1, 59, 60, 61]. However, the resulting stiffness matrix can still be singular (positive semi-definite) if two assignments of degrees of freedom may correspond to the same displacement field. For the discretized equations to have a

unique solution of the degrees of freedom, there must be a one-to-one correspondence between the displacement field and the total vector of degrees of freedom. If such a correspondence exists, the stiffness matrix is guaranteed to be symmetric positive definite after imposing essential boundary conditions. We therefore have the following condition for solvability:

Condition 1 (Necessary and Sufficient)**.** *Assume the weight functions w_i are well defined and further interpolated by linear functions over triangles (see Section 6.2 for more details). The equation $\sum_{i=1}^{m} w_i \mathbf{H}_i \mathbf{q}_i = \mathbf{0}$ has only the unique solution $\mathbf{q}_i = \mathbf{0}$ $(i = 1, \ldots, m)$.*

Unfortunately, this condition cannot be used directly to give constraints on the overlapping meshes without running the actual solution procedure. Ideally we want a procedure to quickly check if a given mesh overlay leads to a well-posed system of equations. We hence introduce some more practical criteria that should be satisfied by the overlapping meshes.

We first consider the issue mentioned in Section 4.2. We require the function P_i to be strictly positive inside the subdomain Ω_i. However, in some case, this condition is not met, see for example Figure 4-3. The function P_i vanishes on element e because all four nodes of this element are located on Γ_i^*. It is then seen that w_i also vanishes on element e. The degrees of freedom at nodes 2 and 3 have no contribution to the final interpolation since the weight w_i vanishes on the support of nodes 2 and 3. Therefore, the assignment of dofs for nodes 2 and 3 can be arbitrary and Condition 1 cannot be satisfied. This type of invalid meshes can be easily checked using a program by examining all elements after the mesh overlay is established. It is also seen that such an invalid mesh only occurs if the mesh is very coarse. Actually, if the element e is further divided into 4 elements, the issue no longer exists.

It is then necessary to avoid such invalid meshes. In other words, the following condition on weight functions w_i should necessarily be satisfied in order to obtain a solvable interpolation:

Condition 2 (Necessary)**.** *Each w_i is strictly positive in Ω_i. Here we consider the*

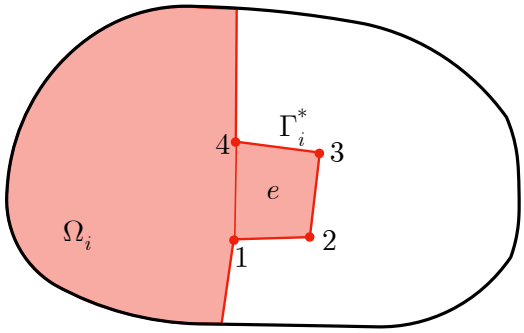

Figure 4-3: An invalid mesh

weight functions defined by Equation 4.1.

In addition, to avoid non-trivial solutions for $\sum_{i=1}^{m} w_i \mathbf{H}_i \mathbf{q}_i = \mathbf{0}$, any weighted displacement interpolation of one mesh cannot be contained in the linear combination of weighted interpolations of other meshes. Due to the piecewise definition of isoparametric interpolations, this is achieved by preventing nodes from overlapping each other except for some boundary nodes.

Note that the weight functions satisfy the partition of unity property. Furthermore, each weight function vanishes outside its subdomain. The global interpolation error has contributions from each individual local field and the convergence rate of the numerical solution is dominated by the lowest-order mesh used. Each individual mesh is responsible for its own subdomain and the local interpolation error can be reduced by using higher-order elements locally. Since, in the problems considered, the solution error in the energy norm is usually of the most interest, the derivatives of weight functions contribute to the global solution error. As a result, the derivatives of weight functions cannot grow too fast, which actually corresponds to requiring reasonably thick overlapped regions.

It is seen already that the final interpolation can exactly solve an arbitrary linear field provided that each local field contains an arbitrary linear field. Hence, the scheme should converge with at least the first order convergence.

A detailed discussion on an error estimate and the effect of overlapping sizes is given in Section 5.3.

4.6 The use of overlapping meshes in AMORE

In AMORE, a regular traditional mesh is used for the interior domain and higher-order elements are used near the boundaries to resolve the boundary stress concentrations and boundary curvature. In the case of overlapping meshes, independent meshes can be spanned for different parts of the analysis domain and they are free to overlap. We suggest the following meshing steps using traditional finite elements:

1. A regular Cartesian grid is spanned over the complete domain of interest.

2. The cells located outside the domain or cutting the boundaries are removed. The remaining cells are converted into 4-node traditional elements, which form the first mesh and the interior subdomain.

3. The boundary regions are divided into several regular subdomains and each subdomain is meshed with 9-node traditional elements.

The meshing procedure is compatible with any reasonable representation of the geometry. Since subdomains or meshes are allowed to overlap freely, the subdomains can all be chosen to be quite regular and the meshes can be simply spanned by procedures such as the coordinate mapping. Although we use traditional elements in the present scheme, the poor performance of them in distorted meshes is effectively avoided since the new meshing procedure and the use of overlapping meshes lead to good quality of each individual mesh.

Several illustrative examples of overlapping meshes in practical engineering problems are given in Section 6.2.

THIS PAGE INTENTIONALLY LEFT BLANK

Chapter 5

Convergence of the Methods

We have introduced the formulations of quadrilateral overlapping finite elements and the method of overlapping finite element meshes in preceding chapters. These new methods involve new interpolation techniques and the resulting fields are continuous. In this chapter, we use the mathematical theorems of conforming finite elements to establish error estimates for these proposed schemes.

Our discussion focuses on a well-posed static problem in two-dimensional linear elasticity.

5.1 Preliminaries

Let Ω be a bounded open connected subset in $\mathbb{R}^2$ with a Lipschitz-continuous boundary $\partial\Omega$. Let S_u be a subset of $\partial\Omega$ with strictly positive measure, and $S_f = \partial\Omega - S_u$. The stress tensor is denoted by τ_{ij}, and the strain tensor is denoted by ϵ_{ij}. We consider the solution of the displacement field $\mathbf{u} = (u_1, u_2)$ in the following system of differential equations:

$$\begin{cases} \tau_{ij,j}(\mathbf{u}) + f_i = 0 \\ \tau_{ij}(\mathbf{u}) = \lambda\epsilon_{kk}(\mathbf{u})\delta_{ij} + 2\mu\epsilon_{ij}(\mathbf{u}) \\ \epsilon_{ij}(\mathbf{u}) = \dfrac{1}{2}\left(u_{i,j} + u_{j,i}\right) \end{cases} \tag{5.1}$$

with boundary conditions

$$\begin{cases} \mathbf{u} = \mathbf{0} \text{ on } S_u \\ \tau_{ij}(\mathbf{u}) n_j = g_i \text{ on } S_f \end{cases} \tag{5.2}$$

where the Einstein summation convention is used, $1 \leq i, j \leq 2$ are indices, $\tau_{ij,j}(\mathbf{u}) = \frac{\partial \tau_{ij}(\mathbf{u})}{\partial x_j}$, $u_{i,j} = \frac{\partial u_i}{\partial x_j}$, $\mathbf{n} = (n_1, n_2)$ is the unit outer normal of $\partial\Omega$, $\mathbf{f} = (f_1, f_2)$ is the body force vector, $\mathbf{g} = (g_1, g_2)$ is the vector of boundary tractions, and λ and μ are material constants.

In following discussions, we denote $\|\cdot\|_{k,\Omega}$ the H^k norm over Ω and $|\cdot|_{k,\Omega}$ the H^k semi-norm over Ω. Whenever the domain Ω is clear, we simply write $\|\cdot\|_k$ and $|\cdot|_k$.

It is well known that the exact displacement solution yields a minimum potential energy of the system among all kinematically admissible displacements, which is called the principle of minimum potential energy. Let $\mathbf{V} = \{(v_1, v_2) \mid v_i \in H^1(\Omega) \text{ and } v_i = 0 \text{ on } S_u\}$ be the space of kinematically admissible displacements equipped with the product norm $\|\mathbf{v}\|_1 = \left(\sum_{i=1}^2 \|v_i\|_1^2\right)^{1/2}$. The space $\mathbf{V}$ is a Hilbert space. The potential energy functional J is given by

$$J(\mathbf{v}) = \frac{1}{2} a(\mathbf{v}, \mathbf{v}) - f(\mathbf{v}) \tag{5.3}$$

where $a(\cdot, \cdot)$ is a bilinear form representing the strain energy, and $-f(\cdot)$ is a linear form representing the potential energy of external forces. It can be seen that

$$a(\mathbf{u}, \mathbf{v}) = \int_\Omega \{\lambda u_{i,i} v_{j,j} + 2\mu \epsilon_{ij}(\mathbf{u}) \epsilon_{ij}(\mathbf{v})\} \, \mathrm{d}\Omega \tag{5.4}$$

and

$$f(\mathbf{v}) = \int_\Omega \mathbf{f} \cdot \mathbf{v} \mathrm{d}\Omega + \int_{S_f} \mathbf{g} \cdot \mathbf{v} \mathrm{d}S \tag{5.5}$$

in which we assume in addition $f_i \in L^2(\Omega)$ and $g_i \in L^2(S_f)$ for $i = 1, 2$ so that the integrations are well defined and the linear form $f(\cdot)$ is continuous. It is also clear that $a(\cdot, \cdot)$ is continuous. Using Korn's Inequality $\|\mathbf{v}\|_1 \leq C(\Omega) \left(\sum_{i,j=1}^2 |\epsilon_{ij}(\mathbf{v})|_0^2 + \sum_{i=1}^2 |v_i|_0^2\right)^{1/2}$, where $C(\Omega)$ is a constant dependent only on the domain Ω, it can be further proved that the bilinear form is coercive, provided the material parameters are reasonable

and the displacement boundary S_u has a strictly positive measure [1, 59, 60, 62]. Therefore, the energy norm $\|\mathbf{v}\|_e = \sqrt{a(\mathbf{v},\mathbf{v})}$ is equivalent to the H^1 product norm, $a(\cdot,\cdot)$ defines an inner product, and $\mathbf{V}$ is also a Hilbert space with respect to the energy norm. In addition, the energy norm is also equivalent to the H^1 product semi-norm $|\mathbf{v}|_1 = \left(\sum_{i=1}^{2} |v_i|_1^2\right)^{1/2}$.

Minimization of the potential energy equivalently yields the principle of virtual work, i.e. the exact solution $\mathbf{u}$ satisfies $a(\mathbf{u},\mathbf{v}) = f(\mathbf{v})$ for all $\mathbf{v} \in \mathbf{V}$. This principle indicating a balance between the internal virtual work and the external virtual work is called a variational form corresponding to the original boundary value problem. It is an immediate result of the Lax-Milgram lemma that the variational problem adopts a unique solution [59, 60, 61].

The main idea of conforming finite element methods is to use a finite-dimensional subspace $\mathbf{V}_h \subset \mathbf{V}$ to approximate the original space, and find an approximation in the subspace in the sense of the variational problem. The subspace, being finite-dimensional, is also a Hilbert space with respect to the same norm and inner product. Therefore all of our discussions on the space $\mathbf{V}$ still hold on the subspace $\mathbf{V}_h$. Our main focus is to find a displacement field $\mathbf{u}_h \in \mathbf{V}_h$ such that

$$a(\mathbf{u}_h,\mathbf{v}_h) = f(\mathbf{v}_h),\ \forall\ \mathbf{v}_h \in \mathbf{V}_h \tag{5.6}$$

The approximation space $\mathbf{V}_h$, being a subspace of $\mathbf{V}$, leads to some restrictions on the actual interpolation used. We consider, for simplicity, the interpolation using straight-edge polygons. In other words, the whole analysis domain is discretized into non-overlapping (closed) polygons K_i, whose boundaries are assumed to be piecewise straight and therefore Lipschitz-continuous. To satisfy $\cup_i K_i = \bar{\Omega}$, the domain needs to be polygonal. It is then a basic result that if the interpolation is piecewise smooth and continuous over the analysis domain, the finite-dimensional approximation space is a subspace of $\mathbf{V}$ [59, 60, 61].

Our discussion focuses on the new interpolation schemes and therefore ignores other non-essential factors. For example, the effect of numerical integration is ignored.

The accuracy of the numerical approximation $\mathbf{u}_h$ depends on the accuracy of the interpolation. In general, let $\mathbf{u}$ be the exact solution and $\mathbf{u}_h$ be the numerical solution, the solution error $\|\mathbf{u} - \mathbf{u}_h\| \leq C \inf_{\mathbf{v}_h \in \mathbf{V}_h} \|\mathbf{u} - \mathbf{v}_h\|$, provided the bilinear form $a(\cdot, \cdot)$ is continuous and coercive, and C is a constant determined by the bilinear form [59, 60, 61]. This result is called Céa's lemma. The $\|\cdot\|$ represents any norm equivalent to the H^1 product norm. In following sections we consider the H^1 product semi-norm. Since the solution error is bounded by the interpolation error, we focus in subsequent sections on the interpolation error using the proposed new interpolations. To further simplify our discussion, we consider the interpolation of one displacement component u.

In following sections, we use without proof some classical interpolation theorems for traditional finite elements. The detailed discussions can be found in References [59, 60, 61, 63].

Throughout the following sections, we use C as a generic constant independent of the element size.

5.2 Convergence of the overlapping elements

5.2.1 Properties of the interpolation

Recall that the interpolation on each element is given in the form $u(\mathbf{x}) = \sum_I \rho_I(\mathbf{x}) u_I(\mathbf{x})$, where $\rho_I(\mathbf{x})$ is the new shape function and $u_I(\mathbf{x})$ is a nodal polynomial. The displacement interpolation is formulated as the weighted average of several local fields interpolated by the method of finite spheres.

As mentioned in Chapter 3, the interpolation is continuous over the whole domain since each local interpolation ψ_I is continuous in its corresponding polygonal element D_I and each traditional shape function h_I is continuous over the whole domain and vanishes outside its corresponding polygonal element D_I, see Equation 3.3. It is seen from Table 3.1 that each $\tilde{\phi}_J^I$ is continuous in D_I. Since the added δ_{IJ} term does not influence the continuity, each ϕ_J^I is also continuous in the polygonal element D_I. It

is therefore concluded from Equation 3.6 that the local field ψ_I is continuous in D_I. In addition, the final interpolation is by definition smooth on each element, provided that elements are not severely distorted. We see that the overlapping finite elements are conforming.

It follows from the continuity of the interpolation that each ρ_I is continuous and vanishes outside its corresponding polygonal element D_I. If we make all nodal polynomials zero except for $u_I = 1$, the displacement field is $u = \rho_I$, hence ρ_I is continuous. It is also directly seen from the interpolation that each u_I has influence only on its adjacent elements, i.e. the support of ρ_I is in D_I. As a result, ρ_I must vanish on the boundary ∂D_I.

The above discussion also holds for any constrained node on the boundary. For imposing boundary displacement constraints, we use a special form for the local fields at constrained boundary nodes. We see from Section 3.4 that $\phi_J^I = \delta_{IJ}$ holds for a constrained node I, and, being a special form of the interpolation when $r_I \gg r_I^*$, ρ_I is still continuous and vanishes outside D_I in this case.

We have shown in Section 3.6 that the new shape functions ρ_I satisfy the partition of unity property, which is actually a crucial fact for proving the error bound, as presented in the next section.

5.2.2 The convergence rate

An interesting feature of the overlapping finite elements is that the interpolation consists of two components, the shape functions and the nodal polynomials, which are constructed in different coordinate systems. The new shape functions have contributions from both traditional and meshless interpolations, see Equation 3.10. However, the Shepard functions are further interpolated using traditional interpolations. Therefore the new shape functions are essentially defined in the local coordinates. On the contrary, the nodal polynomials are directly defined in the (local) Cartesian coordinates.

In traditional finite element analysis, any element in the physical domain is mapped from a fixed reference element. The error bound is also built upon the interpolation

error in this reference element. Since the new interpolation scheme adopts a mixed form using both local (isoparametric coordinates for quadrilaterals and area coordinates for triangles) and Cartesian coordinates, it is actually much more convenient to directly approximate the interpolation error in the global coordinate system. For simplicity, we assume the exact solution u has bounded derivatives up to the order $(k+1)$, where k is the order of nodal polynomials.

As argued in the previous section, we assume the domain is polygonal so that the overlapping finite elements are conforming. In addition, we consider a shape regular and quasi-uniform mesh, that is to say, all elements are of regular shape and their sizes are all close.

For a point $\mathbf{x}$ in the polygonal element D_I, since the polygonal element D_I consists of all triangles and quadrilaterals coupling into node I, the line segment adjoining node I and the point $\mathbf{x}$ is contained in the analysis domain. We can therefore use the Taylor series expansion along this line to find a local polynomial approximation u_I^* of order k such that

$$\begin{cases} |u(\mathbf{x}) - u_I^*(\mathbf{x})| \leq C r_I^{k+1} \\ \left| \frac{\partial \left[u(\mathbf{x}) - u_I^*(\mathbf{x}) \right]}{\partial x} \right| \leq C r_I^k \\ \left| \frac{\partial \left[u(\mathbf{x}) - u_I^*(\mathbf{x}) \right]}{\partial y} \right| \leq C r_I^k \end{cases} \tag{5.7}$$

holds for all $\mathbf{x} \in D_I$, where r_I is the support radius for D_I (see Equation 3.4), and C is a generic constant independent of the element size.

Since the mesh is shape regular and quasi-uniform, we assume that

$$\begin{cases} |\rho_I(\mathbf{x})| \leq C \\ \left| \frac{\partial \rho_I(\mathbf{x})}{\partial x} \right| \leq \frac{C}{r_I} \\ \left| \frac{\partial \rho_I(\mathbf{x})}{\partial y} \right| \leq \frac{C}{r_I} \end{cases} \tag{5.8}$$

holds for all $\mathbf{x} \in D_I$.

Now we take $u^* = \sum_I \rho_I u_I^*$ and estimate the interpolation error in the H^1 semi-

norm

$$
\begin{aligned}
|u-u^*|_1^2 &= \int_\Omega \left\{ \left| \frac{\partial}{\partial x}(u-u^*) \right|^2 + \left| \frac{\partial}{\partial y}(u-u^*) \right|^2 \right\} \mathrm{d}\Omega \\
&= \int_\Omega \left\{ \left| \frac{\partial}{\partial x} \sum_I \rho_I (u-u_I^*) \right|^2 + \left| \frac{\partial}{\partial y} \sum_I \rho_I (u-u_I^*) \right|^2 \right\} \mathrm{d}\Omega
\end{aligned}
\tag{5.9}
$$

where we use $u = \sum_I \rho_I u$ since $\sum_I \rho_I = 1$.

On each quadrilateral or triangular overlapped element, the summation over I involves at most four non-zero items because the element interpolation is dependent only on all nodal dofs of this element. Since the mesh is shape regular and quasi-uniform, denoting by $h = \max_I\{r_I\}$ the maximum element size, we have $r_I \geq \gamma h$ for some positive constant γ. Consequently, the integrand in Equation 5.9 is bounded by Ch^{2k} due to Inequalities 5.7 and 5.8. We therefore have

$$
|u-u^*|_1^2 \leq Ch^{2k} \tag{5.10}
$$

and conclude from Céa's lemma that the overlapping finite elements with the kth order basis yield a convergence rate of k.

We note that the above convergence rate may still be proved if we only assume $u \in H^{k+1}(\Omega)$. In fact, assuming the bounds in Inequality 5.8, we only need to show that a local polynomial u_I^* exists satisfying inequalities similar to those in Inequality 5.7 but in the $L^2(D_I)$ norm. This may be achieved in the standard way using the Deny-Lions Inequality [59, 60, 61] and considering the errors in a reference element with unit support radius. One may refer to References [27, 28] for the idea of the proof.

A numerical example illustrating the convergence rates is given in Section 6.1.3.

5.3 Convergence of the overlapping meshes

5.3.1 Properties of the interpolation

In the method of overlapping finite element meshes, the analysis domain Ω is decomposed into m subdomains Ω_i $(i = 1, \ldots, m)$. Each subdomain Ω_i is then meshed with its own conforming mesh $\mathcal{T}_i$ and traditional finite element interpolations are used to give a local interpolation u_i. On each subdomain Ω_i, a non-negative weight function w_i is constructed using low-order finite element interpolations. These weight functions form a partition of unity for the whole analysis domain and are by construction continuous with $\text{supp}(w_i) \subset \bar{\Omega}_i$. The final interpolation is the weighted average $u = \sum_i w_i u_i$. To integrate the stiffness matrix, the mesh overlay structure is computed and stored, and the overlapped regions are divided into triangles. The weight functions are further interpolated by linear functions over each triangle without violating any requirement.

Since the local interpolation u_i is continuous over Ω_i, and w_i is continuous over Ω and vanishes outside Ω_i, the final field is continuous. The overlapped regions of overlapping meshes are divided into triangles. Clearly, the final interpolation is piecewise smooth in each of these triangles. It follows that the interpolation space is a subspace of the original space and the method is conforming. We assume again the domain is polygonal and the space discretization is exact. In addition, each of these overlapping meshes is shape regular and quasi-uniform. The maximum element size of mesh $\mathcal{T}_i$ is denoted by h_i. An important advantage of the method of overlapping meshes is that, as subdomains are allowed to overlap freely, each subdomain can in practice have a regular shape and be meshed with regular finite elements. Therefore, the assumptions we have here are reasonable and can be fulfilled in engineering practice without much computational overhead.

In Chapter 4 and Chapter 6, we suggest an effective implementation of the method of overlapping meshes following the idea of AMORE. A regular 4-node finite element mesh is used to discretize the interior subdomain and higher-order finite element meshes are spanned over boundary regions to resolve the boundary stress concen-

trations and boundary curvature. On an overlapped region between meshes with different interpolation orders, it is then reasonable to put more weight on the higher-order interpolation. This is achieved by the constants α_i $(i = 1, \ldots, m)$ as seen in Equation 4.1.

5.3.2 The convergence rate

We still consider the interpolation error of a displacement component in the H^1 semi-norm. If an element in mesh $\mathcal{T}_i$ does not overlap with any other element from other meshes, the weight function $w_i = 1$. It follows that all other weight functions must vanish on this element, and the element interpolation degenerates to the local interpolation used. The interpolation error can of course be dealt with using the well-established theory for traditional finite elements. The total interpolation error over non-overlapping elements is then dominated by the lowest-order finite element mesh, which is usually a 4-node finite element mesh for the interior subdomain.

It therefore suffices for us to focus on the interpolation error over the overlapped regions, where the weight functions come into play. Before estimating the interpolation error, we focus on the weight functions and their derivatives.

The weight functions, being non-negative, necessarily range between 0 and 1. Their first order derivatives with respect to x and y are however difficult to bound. Without extensively studying the details of the complicated overlapped regions, we propose a reasonable assumption that is clearly true for many typical overlapping meshes.

Since each weight function w_i vanishes outside Ω_i, we see that $\sum_{j\neq i} w_j$ vanishes outside $\cup_{j\neq i}\Omega_j$. It follows that $w_i = 1$ on the interior boundary of $\cup_{j\neq i}\Omega_j$, i.e. $[\partial\left(\cup_{j\neq i}\Omega_j\right)]\cap\Omega$, and $w_i = 0$ on the interior boundary of Ω_i, i.e. $(\partial\Omega_i)\cap\Omega$. Let h_i^* be the shortest distance between these two interior boundaries (see for example Figure 5-1) and let $h = \min_i\{h_i^*\}$ be the smallest overlapping size. As w_i is continuously defined, and further interpolated by linear functions, we assume $\left|\frac{\partial w_i}{\partial x}\right| \leq \frac{C}{\min\{h_i, h_i^*\}} \leq \frac{C}{\min\{h_i, h\}}$ and $\left|\frac{\partial w_i}{\partial y}\right| \leq \frac{C}{\min\{h_i, h_i^*\}} \leq \frac{C}{\min\{h_i, h\}}$, where h_i is the maximum element size of $\mathcal{T}_i$. Here the h_i enters due to the piecewise interpolation for P_i. It is mentioned in Chapter 4

that the subdomains should overlap rather than just touch each other. We therefore assume that there exists a positive constant γ such that $\gamma h_i \leq h \; \forall i$, i.e. the overlapped regions are thick enough.

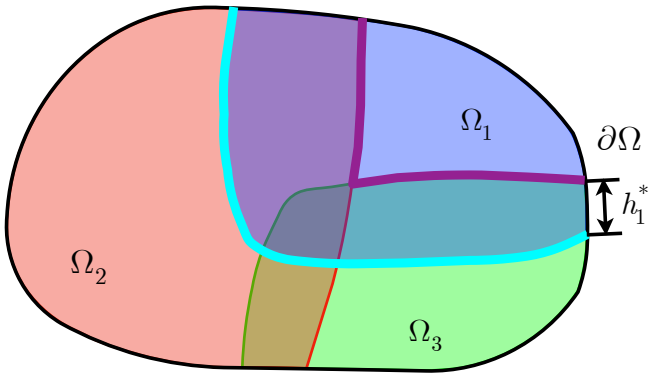

Figure 5-1: The overlapping size h_1^* (the domain decomposition is given in Figure 4-2)

Now each subdomain Ω_i contains a non-overlapping part $\Omega_{i,1}$ and an overlapping part $\Omega_{i,2}$ that satisfy $\Omega_{i,2} = \Omega_i \cap (\cup_{j\neq i}\Omega_j)$ and $\Omega_{i,1} = \Omega_i - \Omega_{i,2}$. Let k_i be the (maximum) order of finite elements in mesh $\mathcal{T}_i$. Assume the exact solution u satisfies $\|u\|_{\max_i\{k_i+1\},\Omega} \leq +\infty$ as in classical interpolation theory. On each subdomain we can find an interpolation u_i^* satisfying

$$\begin{aligned} |u-u_i^*|^2_{1,\Omega_i} &= |u-u_i^*|^2_{1,\Omega_{i,1}} + |u-u_i^*|^2_{1,\Omega_{i,2}} \leq C h_i^{2k_i} \\ \|u-u_i^*\|^2_{0,\Omega_i} &= \|u-u_i^*\|^2_{0,\Omega_{i,1}} + \|u-u_i^*\|^2_{0,\Omega_{i,2}} \leq C h_i^{2k_i+2} \end{aligned} \tag{5.11}$$

where C is a generic constant independent of the element size [59, 60, 61, 63].

Let $u^* = \sum_i w_i u_i^*$ be a global interpolation. The interpolation error in the H^1 semi-norm satisfies

$$\begin{aligned} |u-u^*|^2_{1,\Omega} &= |u-u^*|^2_{1,\cup_i\Omega_{i,2}} + \sum_i |u-u^*|^2_{1,\Omega_{i,1}} \\ &= |u-u^*|^2_{1,\cup_i\Omega_{i,2}} + \sum_i |u-u_i^*|^2_{1,\Omega_{i,1}} \\ &\leq |u-u^*|^2_{1,\cup_i\Omega_{i,2}} + C\sum_i h_i^{2k_i} \end{aligned} \tag{5.12}$$

where the second term on the right-hand side represents the error over non-overlapping parts and the remaining is the error over the overlapped regions. The first term can be rewritten as

$$\begin{aligned} |u-u^*|^2_{1,\cup_i\Omega_{i,2}} &= \int_{\cup_i\Omega_{i,2}} \left\{ \left[\frac{\partial(u-u^*)}{\partial x}\right]^2 + \left[\frac{\partial(u-u^*)}{\partial y}\right]^2 \right\} \mathrm{d}\Omega \\ &= \int_{\cup_i\Omega_{i,2}} \left\{ \left[\frac{\partial \sum_i (w_i(u-u_i^*))}{\partial x}\right]^2 + \left[\frac{\partial \sum_i (w_i(u-u_i^*))}{\partial y}\right]^2 \right\} \mathrm{d}\Omega \end{aligned} \tag{5.13}$$

where we use $u = \sum_i w_i u$. Since

$$\begin{aligned} \left[\frac{\partial \sum_i (w_i(u-u_i^*))}{\partial x}\right]^2 &= \left[\sum_i \frac{\partial w_i}{\partial x}(u-u_i^*) + \sum_i w_i \frac{\partial(u-u_i^*)}{\partial x}\right]^2 \\ &\le \left[\sum_i \left|\frac{\partial w_i}{\partial x}(u-u_i^*)\right| + \sum_i \left|w_i \frac{\partial(u-u_i^*)}{\partial x}\right|\right]^2 \\ &\le 2m \left[\sum_i \left|\frac{\partial w_i}{\partial x}(u-u_i^*)\right|^2 + \sum_i \left|w_i \frac{\partial(u-u_i^*)}{\partial x}\right|^2\right] \end{aligned} \tag{5.14}$$

where we use the Cauchy-Schwarz Inequality and m is the number of meshes. Similarly we can bound $\left[\frac{\partial \sum_i (w_i(u-u_i^*))}{\partial y}\right]^2$. Substituting these inequalities back into Equation 5.13 and using the local error bounds in Inequality 5.11 together with the bounds for w_i $(i = 1, \ldots, m)$ and their derivatives yields

$$\begin{aligned} |u-u^*|^2_{1,\cup_i\Omega_{i,2}} &\le C \int_{\cup_i\Omega_{i,2}} \left\{ \sum_i \left(\chi_{\Omega_{i,2}} \frac{1}{\min\{h_i,h\}^2} |u-u_i^*|^2 \right) \right. \\ &\quad \left. + \sum_i \left[\chi_{\Omega_{i,2}} \left|\frac{\partial(u-u_i^*)}{\partial x}\right|^2 \right] + \sum_i \left[\chi_{\Omega_{i,2}} \left|\frac{\partial(u-u_i^*)}{\partial y}\right|^2 \right] \right\} \mathrm{d}\Omega \\ &\le C \sum_i \left(\frac{1}{\min\{h_i,h\}^2} \|u-u_i^*\|^2_{0,\Omega_{i,2}} \right) + C \sum_i |u-u_i^*|^2_{1,\Omega_{i,2}} \\ &\le C \sum_i \left(\frac{h_i^2}{\min\{h_i,h\}^2} h_i^{2k_i} \right) + C \sum_i h_i^{2k_i} \end{aligned} \tag{5.15}$$

where the function $\chi_{\Omega_{i,2}}$ is 1 on $\Omega_{i,2}$ and 0 elsewhere. Using the assumption $\gamma h_i \le h$ $\forall i$ gives $|u-u^*|^2_{1,\cup_i\Omega_{i,2}} \le C \sum_i h_i^{2k_i}$. Combining the interpolation errors over non-

overlapping parts and overlapped regions then leads to

$$|u - u^*|^2_{1,\Omega} \leq C \sum_i h_i^{2k_i} \tag{5.16}$$

Due to Céa's lemma, we have the same asymptotic bound for the numerical solution error. As expected, the global convergence rate is determined by the lowest-order finite element mesh if all element sizes from different meshes are close.

Notice that if several meshes overlap at a location and the elements involved are not on interior boundaries, each weight function w_i is locally a constant. As a result, the global interpolation is (locally) a linear combination of local fields with constant coefficients. In such a case, we can get rid of the derivatives of w_i in the interpolation error. Because the procedure puts more weight on higher-order interpolations, the local error is then very close to the error of the higher-order interpolations. Such observation allows us to use high-order meshes overlaying a low-order base mesh as local enrichments. However, it is even more effective if the local high-order elements are non-overlapping so the accuracy of high-order interpolations is completely retained. We briefly study the effectiveness of different overlapping meshes in several numerical examples, as given in Section 6.2. It is found that the overlapped regions, which are assumed to be thick enough for the error bound to hold, should not be too large, and the number of meshes overlapping at a location should remain small, so as to save computational effort. Indeed, Inequality 5.15 indicates that the coupling interpolation somewhat deteriorates the accuracy of high-order elements. Small overlapped regions are also advantageous from the viewpoint of solvability, since any single mesh interpolation is not contained in the interpolation of other meshes in such cases, see Section 4.5.

5.3.3 The limit case

The error bound given in the last section relies on an assumption $\gamma h_i \leq h \ \forall i$, i.e. the overlapped regions cannot be too thin. However, whether the solution converges if we let $h \to 0$ while keeping all h_i $(i = 1, \ldots, m)$ finite cannot be predicted using

Inequality 5.15. Alternatively, it would be valuable to give an error bound that is independent of the overlapping sizes. Such a limit case is similar to using non-matching grids so it is interesting to see if the solution really converges to the solution obtained with some scheme for non-matching grids. For this purpose, we study two numerical examples.

A thin beam

We consider in the first example the problem described in Figure 5-2. This slender beam has a free end deflection at 0.1081, which can be calculated using Timoshenko beam theory [64]. Note that we are not interested in this problem in whether the numerical solution converges to the reference solution as the mesh is refined – because we know it does from the last section – but the convergence as $h \to 0$ with h_i $(i = 1, 2)$ staying finite. This thin beam is solved now using two overlapping 9-node finite element meshes, which can be seen in Figure 5-3. The overlapping size is denoted by h.

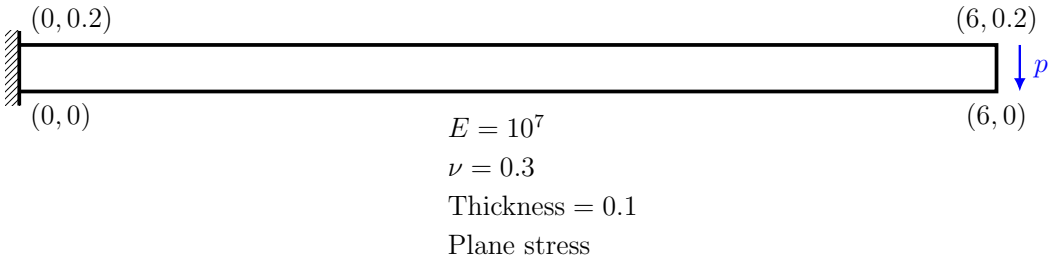

Figure 5-2: The thin beam problem, total applied force = 1

In the overlapping meshes, all elements have the same length 1 except for the leftmost element in the red mesh. The overlapping meshes therefore, in geometry, degenerate to a uniform conforming mesh with six 9-node finite elements, if $h \to 0$. The numerical solutions of the tip deflection and the energy are listed in Table 5.1, where $h = 0$ represents the solutions obtained with a uniform conforming mesh with six 9-node finite elements. It is seen that the solutions converge to the solutions obtained with a uniform conforming mesh.

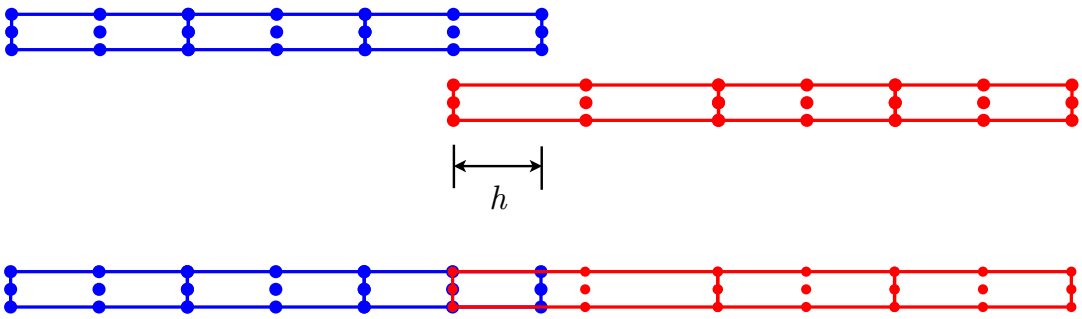

Figure 5-3: Two overlapping 9-node finite element meshes

Table 5.1: Numerical solutions at different overlapping sizes h

h	0.5	0.1	0.01
Tip deflection	0.106946	0.107049	0.107040
Energy	5.34726E−2	5.35241E−2	5.35194E−2
h	0.001	0.0001	0
Tip deflection	0.107035	0.107034	0.107034
Energy	5.35174E−2	5.35168E−2	5.35167E−2

A thick beam

In this example, we consider a thick beam described in Figure 5-4a. The meshes overlap now in a more complex way, as shown in Figure 5-4b. There are two parameters a and b representing the overlapping size. By definition we have $h = \min\{a, b\}$. The numerical solutions of the energy are given in Table 5.2. A reference solution 2.45995E+1 has been obtained using the gluing mesh feature in ADINA.

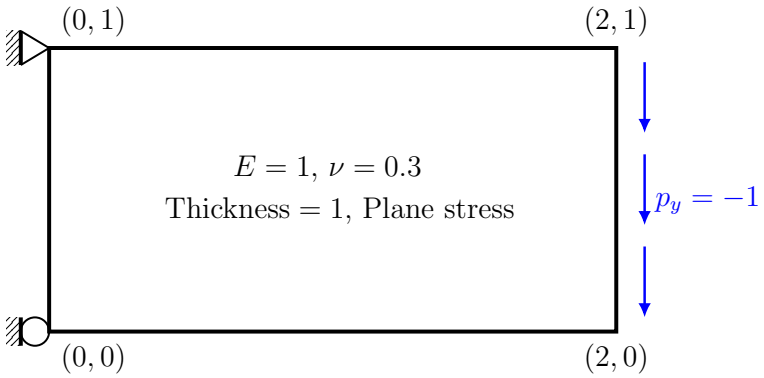

(a) Problem description

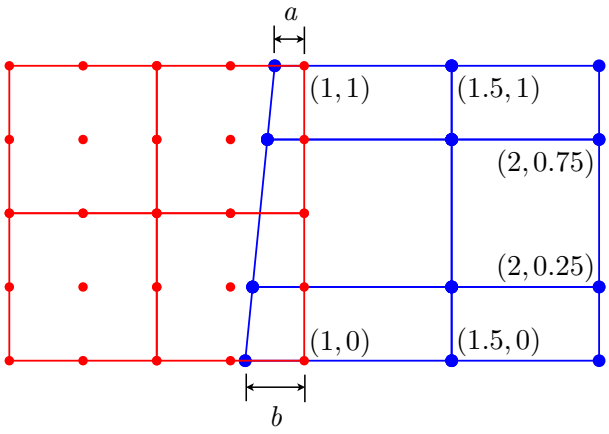

(b) Overlapping meshes

Figure 5-4: A thick beam and the overlapping meshes

If we focus on the diagonal entries of the table, we see that as $h = a = b \to 0$ the energy solution does not increase or decrease monotonically. In addition, there is no evidence showing that the solution converges to the gluing mesh solution in

ADINA, although it is still possible that the limit solution corresponds to a specific scheme for non-matching grids. Actually, if we further reduce the overlapping size, the solution is 2.45603E+1 when $h = a = b = 0.00001$. The convergence is at least not as obvious as in the first example. We note that the energy solutions are not symmetric with respect to a and b because the triangulation used for the overlapped region is asymmetrical, see Appendix B for details.

Table 5.2: Numerical solutions of the energy at different parameters (a, b)

b \ a	0.2	0.1	0.01	0.001	0.0001
0.2	2.46632E+1	2.46658E+1	2.46530E+1	2.46269E+1	–
0.1	2.46779E+1	2.46891E+1	2.46877E+1	2.46692E+1	–
0.01	2.46844E+1	2.47027E+1	2.47020E+1	2.46839E+1	–
0.001	2.46672E+1	2.46904E+1	2.46863E+1	2.46484E+1	–
0.0001	–	–	–	–	2.45857E+1

Discussion

It is seen from these two examples that, although there is no solid evidence supporting the claim that the overlapping meshes correspond to a certain non-matching grid scheme in the limit case, this property may hold in some special cases. In addition, we see that, at least for these example problems, the solution error does not increase without bound in the limit case. For this reason, in practical problems, overlapping meshes with very thin overlap may still be used and the solution may still be reasonable. It would be of much value to improve the existing error bound, in order to precisely predict the behavior of solutions in such limit cases. The interpolation error over overlapped regions is now estimated quite roughly. Therefore a better error bound is also needed for us to better understand the extra error induced by the coupling.

For conforming finite elements, the energy norm of any numerical solution is less than or equal to the energy norm of the exact solution, since $a(u-u_h, u-u_h) = a(u,u) - a(u_h,u_h) \geq 0$. A larger energy therefore indicates less solution error. However, it is seen in Table 5.2 that as h becomes very small, the energy starts to decrease. It is thus possible for the solution to get worse in the limit case. In addition, the almost vanishing overlapped region may yield very small entries in the stiffness matrix, and the condition number of the discretized equations can become prohibitively large. For the thick beam problem, the 1-norm condition numbers of the stiffness matrices obtained with different overlapping sizes are listed in Table 5.3. It can be seen that the condition number increases rapidly as the overlapping size decreases. We therefore do not suggest using the present scheme in overlapping meshes with very thin overlapped regions.

Table 5.3: 1-norm condition numbers of the stiffness matrices obtained with different overlapping sizes ($h = a = b$)

$h = a = b$	0.2	0.1	0.01	0.001	0.0001
Condition number	8110	9154	74838	737597	7350116

5.3.4 A discussion on one-dimensional overlapping meshes

Although there is still no evidence showing that the solution error of overlapping meshes remains well bounded in the limit case, the one-dimensional counterpart does have such a property. This also partially explains the convergence for the thin beam problem, in which the overlapping is essentially one-dimensional, and the error bound can be proved using an argument similar to the following.

In the one-dimensional case we still consider a well-posed second order elliptic problem, e.g. Poisson's equation with vanishing boundary values. All the properties mentioned in Section 5.1 still hold. We hence can still focus on the interpolation error in the H^1 semi-norm.

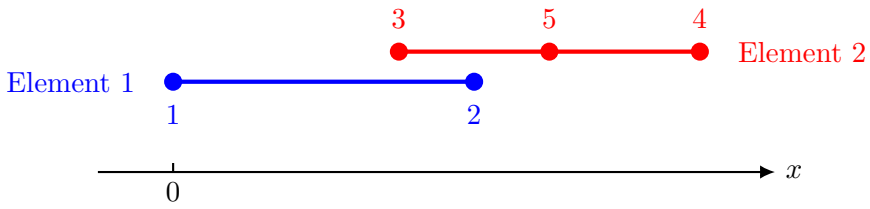

Figure 5-5: The overlapping of a linear element and a quadratic element

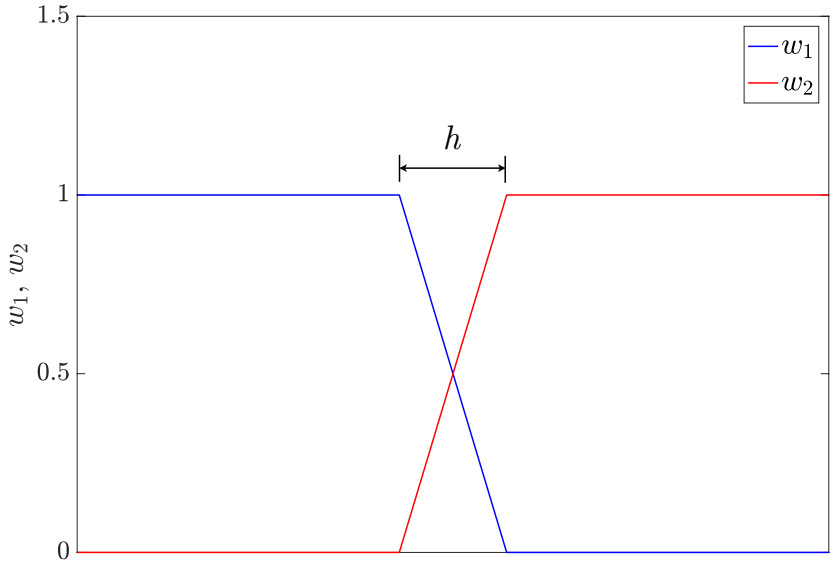

Figure 5-6: The weight functions in one-dimensional overlapping meshes

For simplicity, we consider the overlapping of a linear element mesh $\mathcal{T}_1$ and a quadratic element mesh $\mathcal{T}_2$. The weight functions are still constructed using the low-order finite element interpolation, that is, the linear interpolation, and then normalized. Similarly, the weight functions are interpolated over each overlapped line segment using linear functions. As argued for the two-dimensional case, we focus here on the interpolation error over an overlapped region. We show in Figure 5-5 the overlapping of a linear element and a quadratic element. The overlapping size is denoted by h. The (interpolated) weight functions are plotted in Figure 5-6. Since the weight functions are linear functions, the slopes can be easily calculated and we have

$$\left|\frac{\mathrm{d}w_i}{\mathrm{d}x}\right| = \frac{1}{h} \ (i = 1, 2) \tag{5.17}$$

Let $f : [a, b] \to \mathbb{R}$ be a target function with derivatives up to the order $(k+1)$. A polynomial interpolation P_k of order k satisfies $f(x_i) = P_k(x_i)$ $(i = 0, 1, \ldots, k)$ with $a = x_0 < x_1 < \cdots < x_k = b$. It is a classical result that

$$f(x) - P_k(x) = f^{(k+1)}(\xi)\frac{w_k(x)}{(k+1)!} \tag{5.18}$$

where $x \in [a, b]$, $w_k(x) = \Pi_{i=0}^{k}(x - x_i)$, and ξ is a point in (a, b). Such an interpolation necessarily yields $f'(y_i) = P_k'(y_i)$ $(i = 1, \ldots, k)$ and each $y_i \in (x_{i-1}, x_i)$. Let $w_{k-1}^*(x) = \Pi_{i=1}^{k}(x - y_i)$. There exists a point $\xi^* \in (a, b)$ such that

$$f'(x) - P_k'(x) = f^{(k+1)}(\xi^*)\frac{w_{k-1}^*(x)}{k!} \tag{5.19}$$

$\forall x \in [a, b]$.

To use the classical interpolation error bounds, we assume the exact solution has bounded derivatives up to the third order. For simplicity we only consider the case where h is very small compared with the element sizes. On the overlapped region we

can find interpolations u_1^* and u_2^* satisfying

$$\begin{aligned} |u - u_1^*| &\leq Ch_1 h \\ |u - u_2^*| &\leq Ch_2^2 h \\ \left|\frac{\mathrm{d}}{\mathrm{d}x}(u - u_1^*)\right| &\leq Ch_1 \\ \left|\frac{\mathrm{d}}{\mathrm{d}x}(u - u_2^*)\right| &\leq Ch_2^2 \end{aligned} \tag{5.20}$$

where h_i is the maximum element size in $\mathcal{T}_i$. It follows that

$$|u_1^* - u_2^*| \leq C(h_1, h_2)h \tag{5.21}$$

on the overlapped region, where $C(h_1, h_2)$ is a constant dependent only on h_1 and h_2.

The global interpolation is taken as $u^* = w_1 u_1^* + w_2 u_2^*$, and the interpolation error over the overlap is

$$|u - u^*|^2_{1,\Omega_1 \cap \Omega_2} = \int_{\Omega_1 \cap \Omega_2} \left|\frac{\mathrm{d}}{\mathrm{d}x}(u - u^*)\right|^2 \mathrm{d}x \tag{5.22}$$

Noticing $u = w_1 u + w_2 u$, it can be seen that the integrand in Equation 5.22 is bounded, since

$$\begin{aligned} \left|\frac{\mathrm{d}}{\mathrm{d}x}(u - u^*)\right| &= \left|\frac{\mathrm{d}}{\mathrm{d}x}\left[(w_1 + w_2)(u - u_1^*) + w_2(u_1^* - u_2^*)\right]\right| \\ &= \left|\frac{\mathrm{d}}{\mathrm{d}x}\left[(u - u_1^*) + w_2(u_1^* - u_2^*)\right]\right| \\ &\leq \left|\frac{\mathrm{d}}{\mathrm{d}x}(u - u_1^*)\right| + \left|\frac{\mathrm{d}}{\mathrm{d}x}\left[w_2(u_1^* - u_2^*)\right]\right| \\ &\leq C(h_1, h_2) \end{aligned} \tag{5.23}$$

where we use Equation 5.17 and Inequalities 5.20 and 5.21. An error bound independent of the overlapping size h can then be obtained. The crucial observation is to show that $|u_1^* - u_2^*|$ is well bounded on the overlapped region by the overlapping size h. A similar argument can be used to prove an error bound independent of the overlapping sizes for two-dimensional overlapping meshes, provided that the overlapping elements are well aligned. However, the error bound in general cases remains an

outstanding problem.

THIS PAGE INTENTIONALLY LEFT BLANK

Chapter 6

Numerical Solutions

In this chapter, several numerical examples are solved using the proposed schemes for a better understanding of their numerical performance.

6.1 Numerical solutions using the overlapping finite elements

6.1.1 The numerical implementation

In the overlapping finite element method, the nodal unknowns are polynomial functions. And these polynomial coefficients are solved for numerically in the implementation stage. The stiffness matrix can be ill-conditioned as different polynomial terms can vary significantly in magnitude. To avoid stability issues, the system of discretized equations can be normalized by rewriting the nodal polynomials as

$$u_I = a^*_{I1} + a^*_{I2}\frac{2x}{r_I} + a^*_{I3}\frac{2y}{r_I} + a^*_{I4}\frac{4x^2}{r_I^2} + a^*_{I5}\frac{4xy}{r_I^2} + a^*_{I6}\frac{4y^2}{r_I^2} + \dots \tag{6.1}$$

where r_I is the support radius for node I. The system of equations corresponding to the new unknown coefficients a^*_{Ii} has a much better conditioning.

For the numerical integration, we require the integration to be exact when the elements are not distorted [1, 59]. Specifically, for the overlapping elements with

quadratic basis, we use the 16-point quadrature rule (see References [1, 57, 58]) for triangular overlapping elements (see Appendix A), and the 6×6 Gauss quadrature rule for the quadrilateral overlapping elements.

In practical applications, the numbers of quadrature points may be reduced, as 5×5 quadrature points for quadrilateral elements and 12 quadrature points for triangles lead to almost the same solutions in the tested problems, and no spurious mode is observed. Unlike many meshless methods, the numerical integration effort is insignificant in the proposed scheme [5, 13]. Therefore, we still suggest using the full integration schemes.

Several example solutions using the new overlapping finite elements are given in the following sections.

6.1.2 A thin beam problem for testing trapezoidal elements

This thin beam problem shown in Figure 5-2 was studied by MacNeal. It was found that no traditional 4-node finite element would well resolve the trapezoidal locking in this problem, as well as passing the constant stress patch tests [65]. Table 6.1 lists the numerical solutions of the tip deflection at the free end obtained with quadrilateral overlapping elements, 4-node elements with incompatible modes [66], and traditional 4-node finite elements. The meshes used can be seen in Figure 6-1. The reference solution 0.1081 has been obtained using Timoshenko beam theory [64]. In the solutions, a mesh is refined by dividing each element edge into equal line segments.

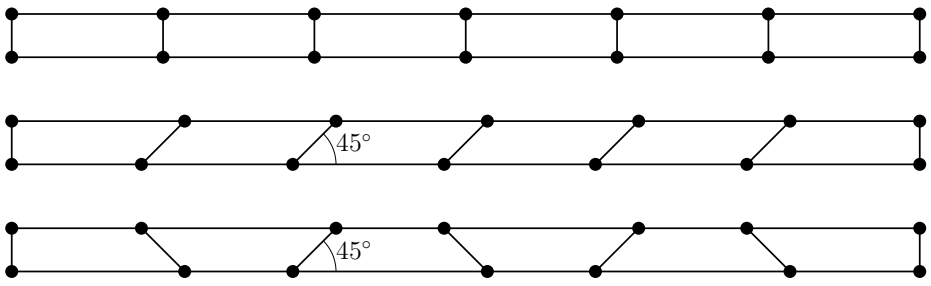

Figure 6-1: Meshes used for the thin beam problem

The incompatible element performs well when the mesh is regular since it is designed in the rectangular configuration by adding bending solutions into the interpolation. However, we see that incompatible elements suffer from the trapezoidal locking although the convergence is still observed. In this problem, the proposed new overlapping elements are more effective, especially when the mesh is distorted. The 4-node finite element, as expected, performs poorly due to the shear locking and mesh distortions.

Table 6.1: Numerical solutions for the thin beam problem (Reference solution = 0.1081)

	1×6 Mesh	2×12 Mesh	3×18 Mesh	4×24 Mesh
Overlapping finite elements (Quadratic basis)				
Rectangular	0.1069 (156 dofs)	–	–	–
Parallelogram	0.1072 (156 dofs)	–	–	–
Trapezoidal	0.1070 (156 dofs)	–	–	–
Incompatible elements				
Rectangular	0.1073 (24 dofs)	–	0.1076 (144 dofs)	0.1077 (240 dofs)
Parallelogram	0.0675 (24 dofs)	–	0.1056 (144 dofs)	0.1072 (240 dofs)
Trapezoidal	0.0049 (24 dofs)	–	0.0964 (144 dofs)	0.1044 (240 dofs)
4-node finite elements				
Rectangular	0.0101 (24 dofs)	–	–	0.0671 (240 dofs)
Parallelogram	0.0037 (24 dofs)	–	–	0.0395 (240 dofs)
Trapezoidal	0.0029 (24 dofs)	–	–	0.0502 (240 dofs)

6.1.3 Convergence study for an ad-hoc problem

The convergences of different elements in an ad-hoc problem are investigated. In this problem, the displacements are prescribed and the applied body forces are calculated

using the equations of equilibrium, as shown in Figure 6-2 along with the meshes used. The exact strain energy is about 5.9414×10^8.

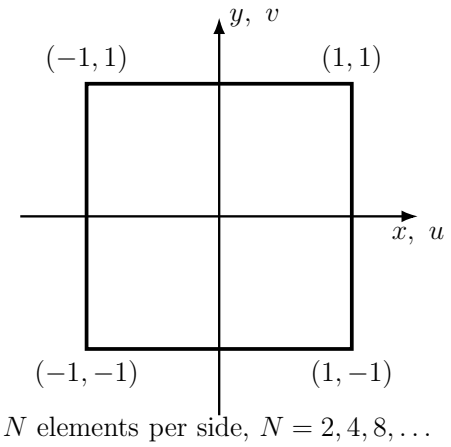

$E = 2 \times 10^5,\ \nu = 0.3$

$u = (1 - x^2)(1 - y^2)e^{5y} \cos 5x$

$v = (1 - x^2)(1 - y^2)e^{5y} \sin 5x$

Unit thickness

Plane stress

(a) Problem description

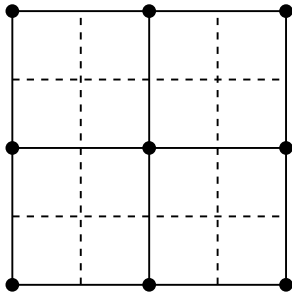

(b) Regular mesh

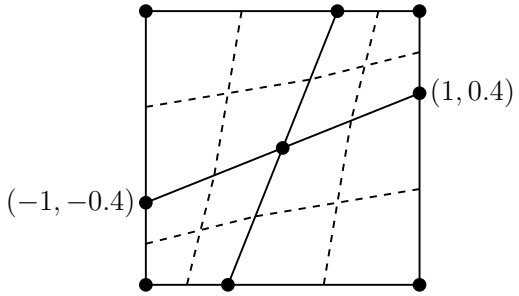

(c) Distorted mesh

Figure 6-2: The ad-hoc problem

It is seen in Figure 6-3 that the convergence rates agree with our discussion in Chapter 5, where h overall represents the element size, i.e. diameter of the smallest circle encompassing the element [1].

6.1.4 Bending beam problems for studying the effects of mesh distortions

It is mentioned in Chapter 3 that the overlapping finite elements are insensitive to mesh distortions because they are able to reproduce an arbitrary kth order polynomial

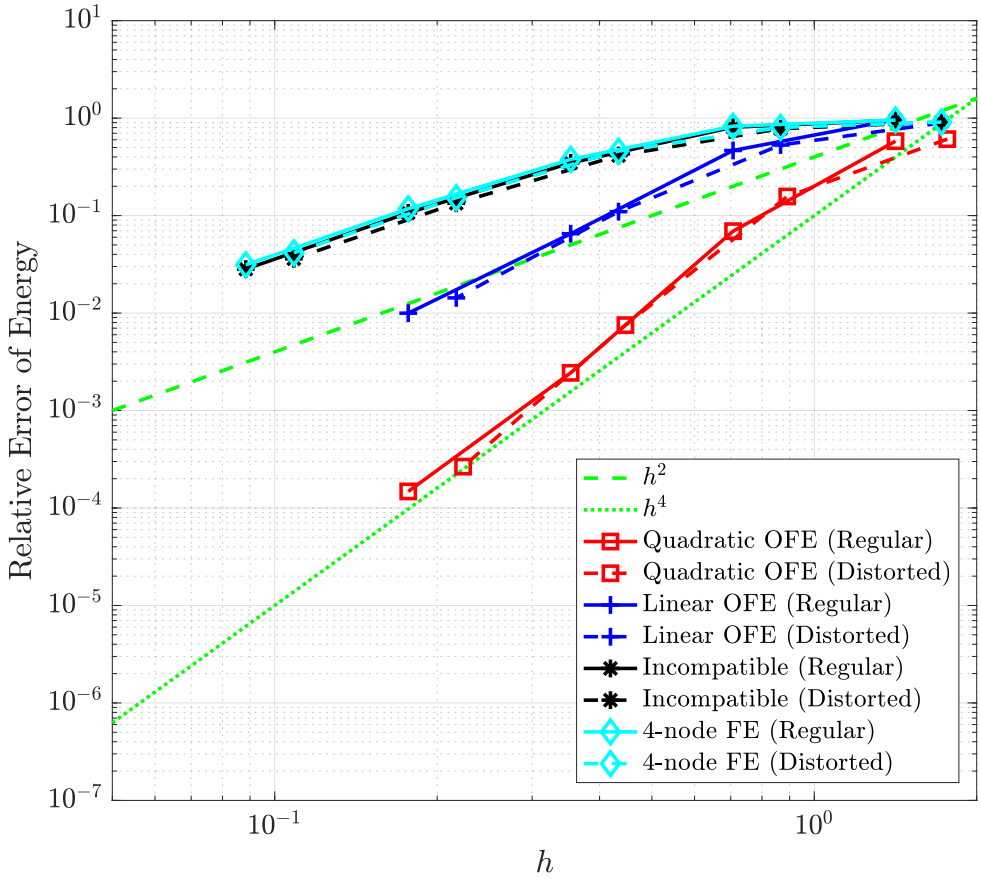

Figure 6-3: Convergence rates of elements for the ad-hoc problem

irrespective of the mesh distortions, where k is the order of basis functions. We demonstrate the mesh distortion insensitivity using a pure bending beam and a linear bending beam given in Figure 6-4. The analytical solutions [54] for these problems are

$$\begin{aligned}
\text{Pure bending:} \quad u &= \frac{120x - 120xy}{E} \\
v &= \frac{60x^2 + 18y^2 - 36y}{E} \\
\text{Linear bending:} \quad u &= \frac{6x^2y - 4.6y^3 - 6x^2 - 120xy + 13.8y^2 + 120x - 9.2y}{E} \\
v &= \frac{-2x^3 - 1.8xy^2 + 60x^2 + 3.6xy + 18y^2 + 9.2x - 36y}{E}
\end{aligned} \tag{6.2}$$

where u denotes the x-displacement and v denotes the y-displacement.

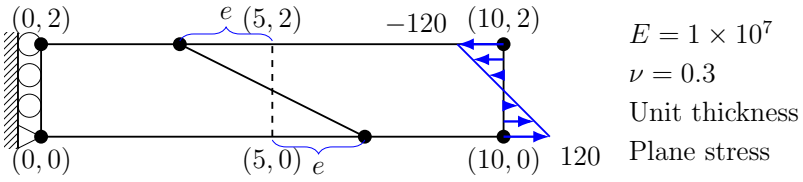

(a) Pure bending

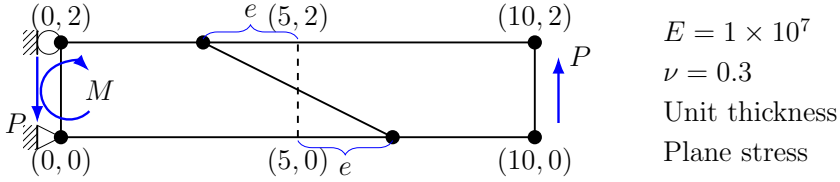

(b) Linear bending

Figure 6-4: Two bending beams

Table 6.2 and Table 6.3 list the numerical solutions of the vertical displacement at the corner point $(10, 0)$ as the distortion parameter e increases. These numerical solutions with traditional 4-node finite elements and incompatible elements are obtained by refining the given meshes into $4 \times 4 \times 2$.

As expected, the quadratic overlapping elements give the exact solution for the pure bending beam irrespective of the mesh distortion. For this constant bending case, the incompatible elements give the exact solution when elements are regular since the added interpolation functions are bending solutions in this case. However, the solution accuracy using incompatible elements decreases as e increases. The 4-node finite elements are most sensitive to the mesh distortion because only the linear field can be exactly reproduced. For the linear bending case, the quadratic overlapping finite elements still give very accurate numerical solutions for different values of e, although the analytical displacement field, being a cubic polynomial, can no longer be exactly resolved by these elements.

Table 6.2: The vertical displacement v at $(10, 0)$: The pure bending beam (OFE: overlapping finite elements; FE: finite elements)

	$e = 0$	$e = 2$	$e = 4$	$e = 4.9$
Quadratic OFE (65 dofs)	6.0000E−4	6.0000E−4	6.0000E−4	6.0000E−4
Incompatible FE (84 dofs)	6.0000E−4	5.9741E−4	5.4826E−4	4.8066E−4
4-node FE (84 dofs)	5.1861E−4	3.3018E−4	1.6362E−4	1.2214E−4
Reference		6.0000E−4		

Table 6.3: The vertical displacement v at $(10, 0)$: The linear bending beam

	$e = 0$	$e = 2$	$e = 4$	$e = 4.9$
Quadratic OFE (69 dofs)	4.0874E−4	4.0886E−4	4.0899E−4	4.0931E−4
Incompatible FE (87 dofs)	4.0766E−4	4.0573E−4	3.7196E−4	3.2252E−4
4-node FE (87 dofs)	3.5059E−4	2.4361E−4	1.3642E−4	1.0495E−4
Reference		4.0920E−4		

6.1.5 The AMORE paradigm in the analysis of a bracket problem

We present in Section 3.7 a general framework for using overlapping elements in the AMORE paradigm. In this section, we give a detailed example and discuss the numerical solutions.

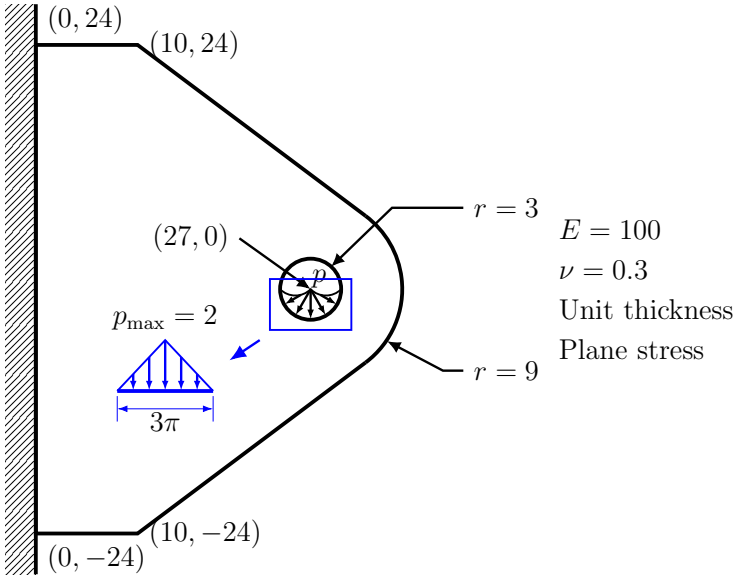

Figure 6-5: A bracket problem

The bracket, which is fixed on the left boundary and loaded on its hole, can be seen in Figure 6-5. In the AMORE paradigm, both overlapping elements and regular finite elements are used to mesh the complete analysis domain. Regular finite elements, being very effective, are spanned over the interior part of the domain. Overlapping elements, being accurate and mesh distortion insensitive, are used to fill in the boundary regions. The new meshing procedure is described in Figure 6-6. In Figure 6-6d, overlapping elements are red, regular finite elements (4-node incompatible elements) are blue, and coupling elements are filled in with green.

In this problem, we use both quadrilateral and triangular overlapping finite elements. The triangular overlapping elements are more suitable for the boundary with large curvature. We note that the formulation of triangular overlapping elements is

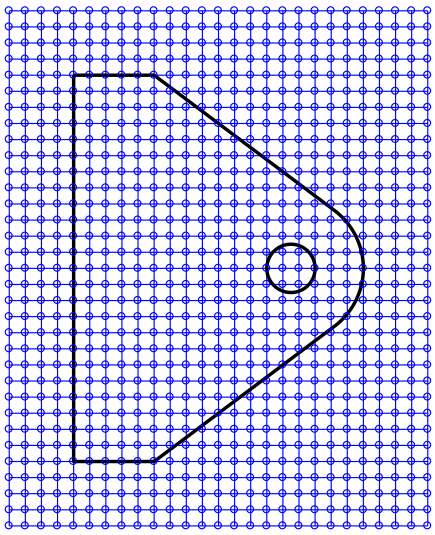

(a) Step 1: The analysis domain is covered by a Cartesian grid

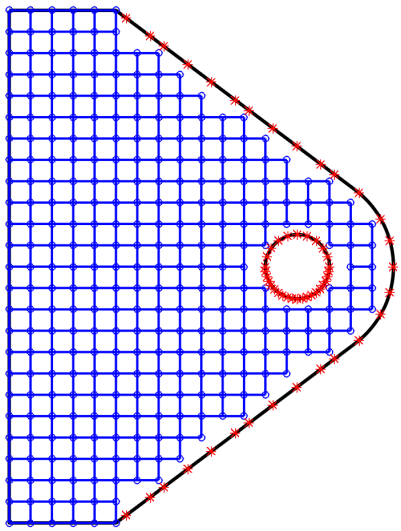

(b) Step 2: The boundary is discretized; The cells outside or cutting the boundaries are deleted

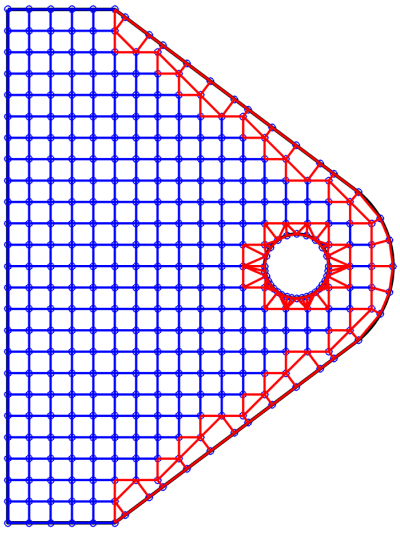

(c) Step 3: The empty boundary regions are meshed with overlapping elements

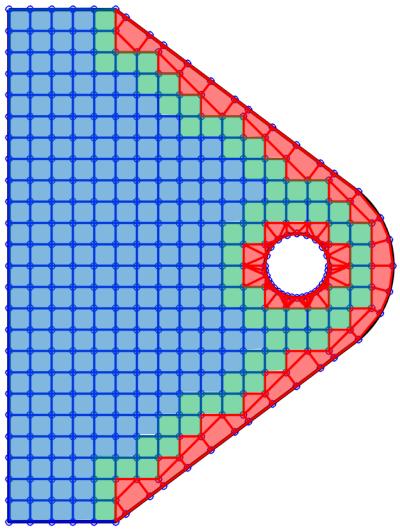

(d) The AMORE mesh (1936 dofs)

Figure 6-6: The AMORE paradigm in the solution of a bracket problem

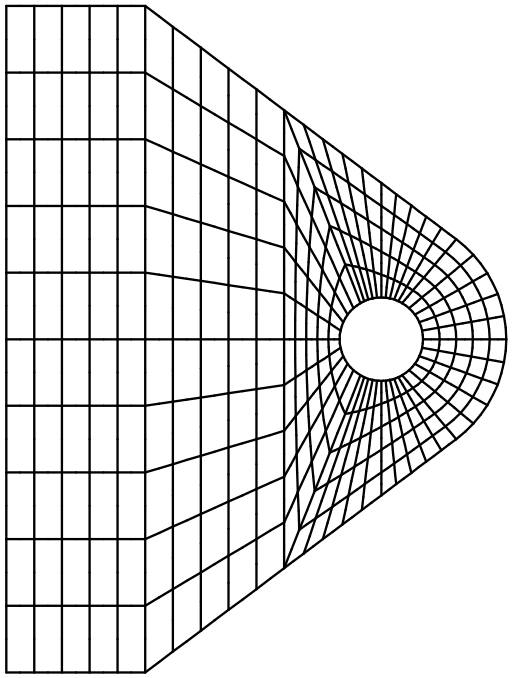

Figure 6-7: A traditional 9-node element mesh (2558 dofs)

slightly different from an earlier formulation [5, 7] in order to obtain compatibility between quadrilateral and triangular overlapping elements. The new formulation of triangular overlapping elements is given in Appendix A.

A traditional 9-node element mesh is used for comparison, and is shown in Figure 6-7. A reference solution has been obtained with a very fine 9-node element mesh in ADINA. The solutions of the horizontal displacement u, the stress τ_{xy}, and the effective stress $\bar{\tau}$ are presented in Figure 6-8. From the perspective of overall accuracy, the AMORE paradigm and traditional mesh both give reasonable energy predictions with about 0.2% relative error. Although the traditional mesh leads to satisfying overall accuracy and displacement results, the AMORE paradigm shows better local stress solutions. The AMORE scheme has this advantage since the local stress concentrations are well resolved by using efficient overlapping elements in the boundary regions.

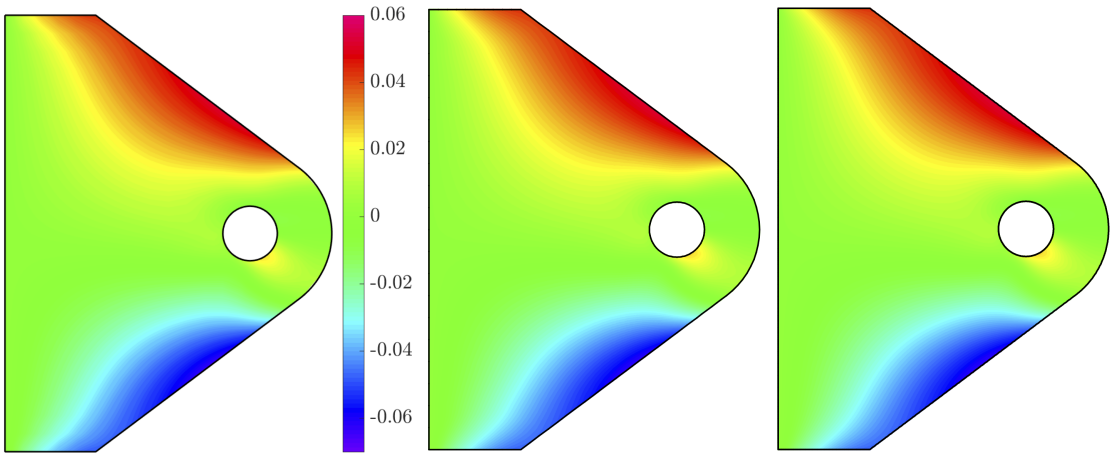

(a) Left: AMORE mesh ($u_{\max} = 0.05224$, $u_{\min} = -0.06284$); Middle: Traditional mesh ($u_{\max} = 0.05224$, $u_{\min} = -0.06298$); Right: Reference ($u_{\max} = 0.05231$, $u_{\min} = -0.06312$)

Figure 6-8: Numerical solutions for the bracket problem

6.2 Numerical solutions using the overlapping meshes

6.2.1 The numerical implementation

The use of overlapping meshes in AMORE is introduced in Section 4.6. The analysis domain is decomposed into an interior subdomain and several boundary subdomains. For the interior subdomain, 4-node elements with or without incompatible modes are used [1, 66]. If a 4-node element is overlapping with elements from other meshes, the incompatible modes are removed. Although finite elements with incompatible modes generally perform better, the present overlapping interpolation requires compatibility of all local fields. For the boundary meshes, 9-node finite elements are used.

A cantilever plate with two holes can be seen in Figure 6-9. In engineering problems, there are usually fillets to avoid large stress concentrations, and the fillets are also considered here. This analysis domain is decomposed into two subdomains, and the red subdomain is disconnected. As in many AMORE meshes, the interior subdomain (blue) is discretized using 4-node elements, and 9-node elements are used in the boundary subdomain (red) to resolve the boundary stress concentrations and the boundary curvature at the fillets and holes.

As introduced in Chapter 4, the key of an effective implementation of the method

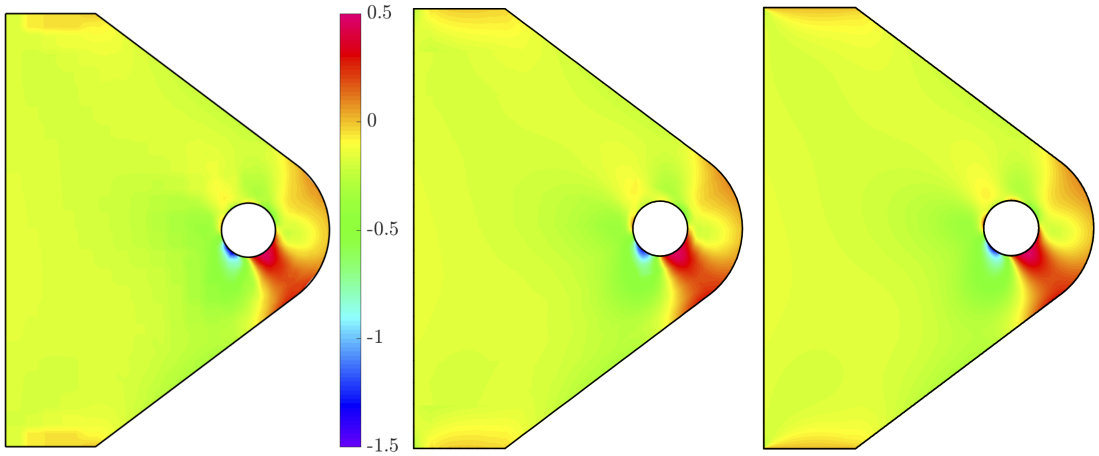

(b) Left: AMORE mesh ($\tau_{xy\,\max} = 0.4728$, $\tau_{xy\,\min} = -1.4525$); Middle: Traditional mesh ($\tau_{xy\,\max} = 0.4625$, $\tau_{xy\,\min} = -1.3187$); Right: Reference ($\tau_{xy\,\max} = 0.4680$, $\tau_{xy\,\min} = -1.4604$)

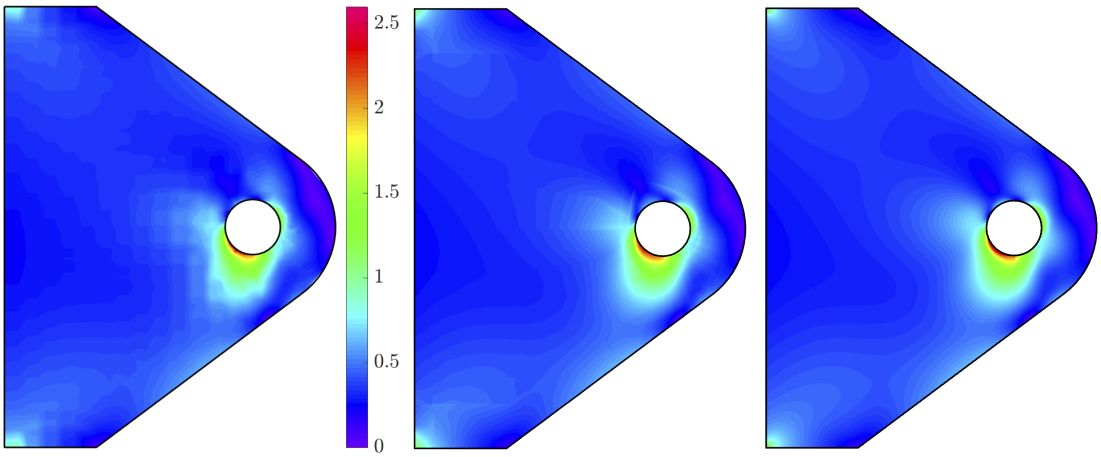

(c) Left: AMORE mesh ($\bar{\tau}_{\max} = 2.6681$); Middle: Traditional mesh ($\bar{\tau}_{\max} = 2.3358$); Right: Reference ($\bar{\tau}_{\max} = 2.5800$)

Figure 6-8: Numerical solutions for the bracket problem (continued)

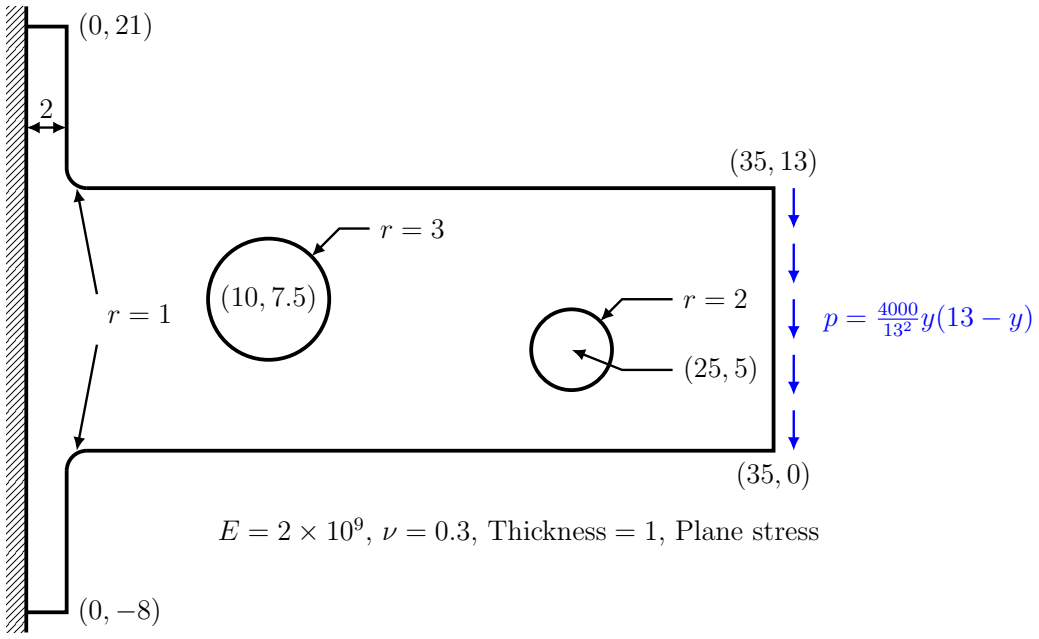

(a) Problem description

Figure 6-9: A plane stress plate problem and the overlapping meshes

of overlapping meshes is to effectively integrate the stiffness matrix. We propose here an integration procedure based on efficient calculation and storage of the mesh overlay structure. A mesh overlay is formally defined as the planar subdivision induced by several overlapping meshes. It is seen in Figure 6-9c that the mesh overlay consists of general polygons. These polygons can be quite arbitrary due to the arbitrariness of the overlapped regions.

For a practical numerical integration scheme, the mesh overlay is calculated to give a list of polygons (for overlapped regions) and a list of non-overlapping elements. Each polygon is then triangulated. The mesh overlay corresponding to Figure 6-9 is shown in Figure 6-10. In this figure, red quadrilaterals are non-overlapping elements and blue triangles represent the result of the triangulation. Over each triangle, the weight functions are interpolated by linear functions using their values on vertices. Quadrature schemes for triangles are then used to evaluate the contribution of the stiffness matrix from each triangle [1, 57, 58]. All elements overlapping at a location couple in the stiffness matrix, therefore we also maintain for each triangle pointers to

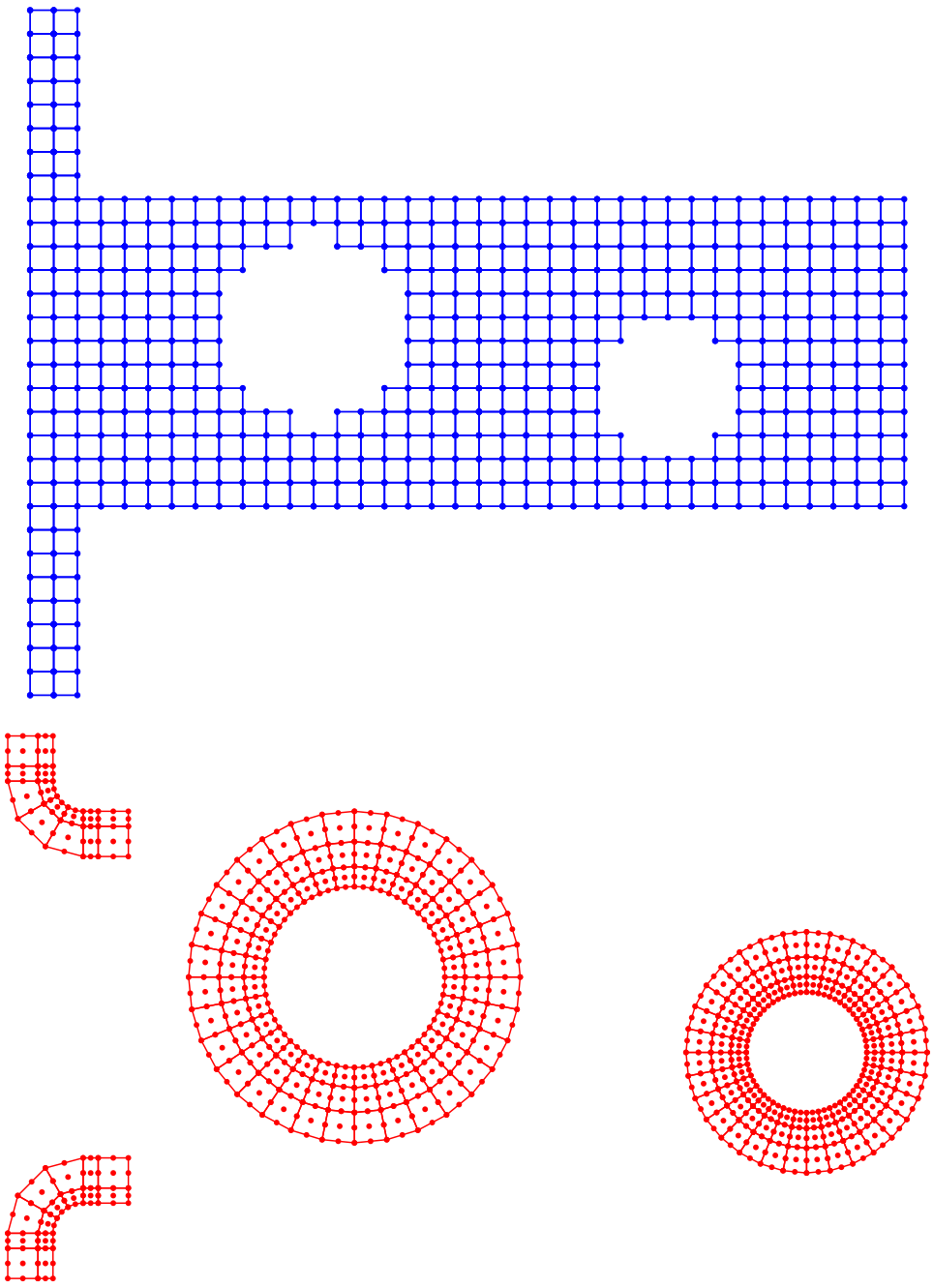

(b) The individual meshes used (not to scale)

Figure 6-9: A plane stress plate problem and the overlapping meshes (continued)

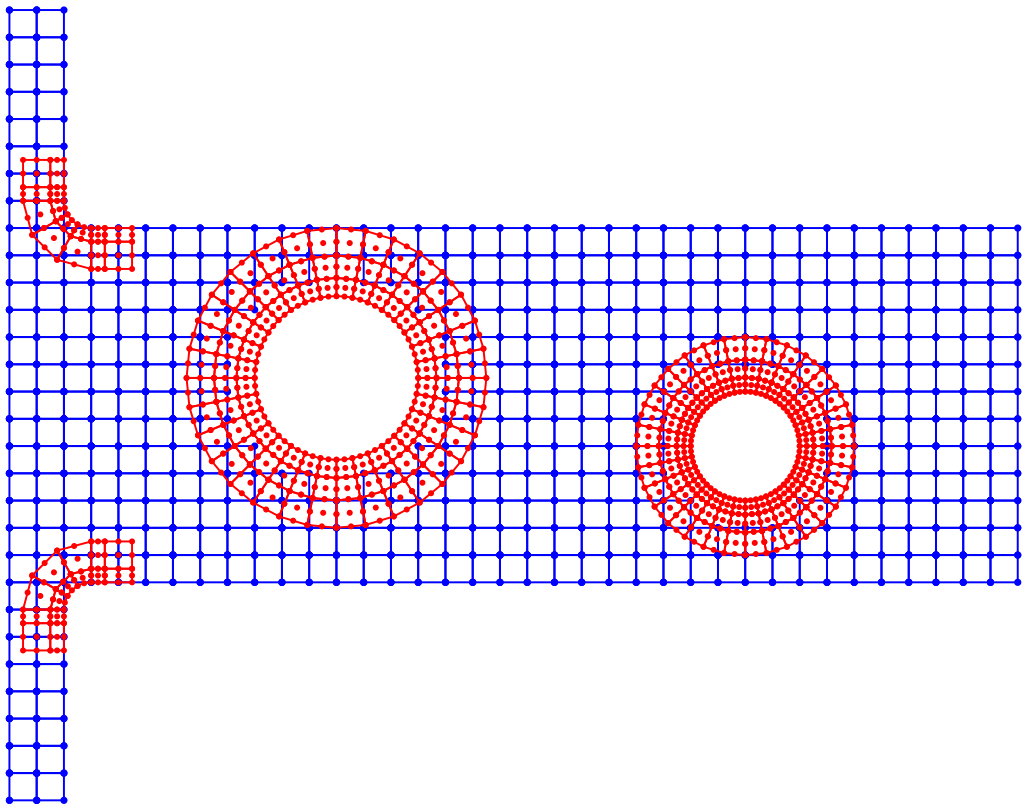

(c) Overlapping meshes

Figure 6-9: A plane stress plate problem and the overlapping meshes (continued)

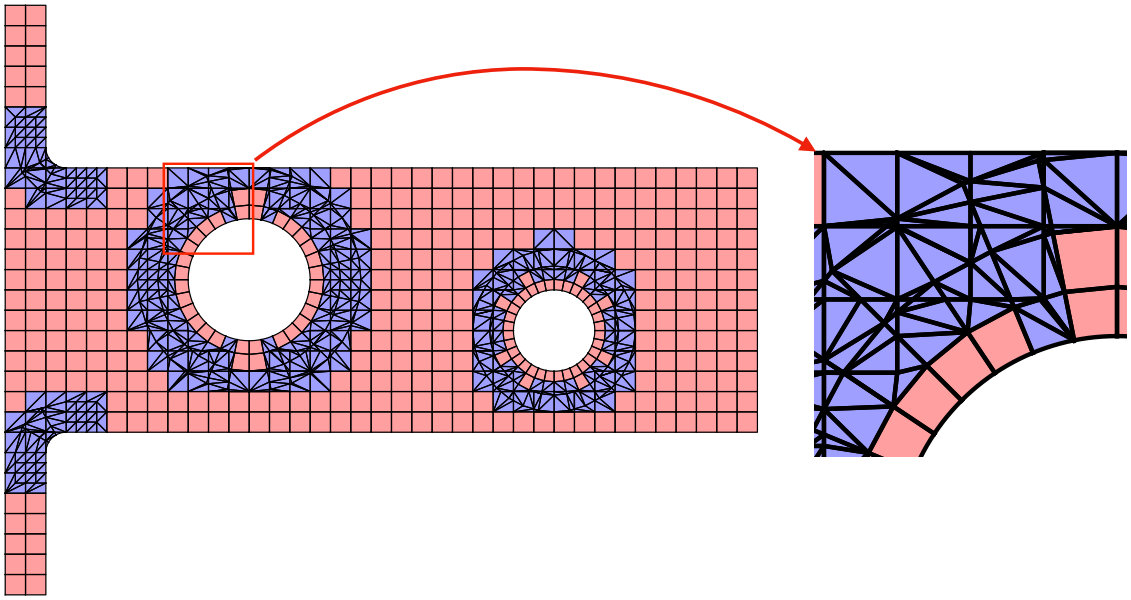

Figure 6-10: A mesh overlay and the triangulation

its incident elements. Although many triangles in Figure 6-10 are severely distorted, we note that they are not triangular finite elements and are merely used for numerical integration. The distortion hence causes no harm to the numerical solution. For all non-overlapping elements, it is known from Chapter 4 that $w_i = 1$ holds for some i. The local interpolation is identical to a traditional interpolation and these elements are integrated as traditional elements.

The plane sweep algorithm and a simple triangulation algorithm are used in the proposed implementation. A detailed introduction can be found in References [55, 56], while a brief introduction of the algorithms is also given in Appendix B. Let n be the total complexity of the mesh overlay, i.e. the total number of polygons, vertices, and edges. The computational expense for the mesh overlay processing is $O(n \ln n)$. Such time complexity can be practical for engineering applications. In the plane sweep algorithm, a sweep line moves towards a specific direction over the whole domain to find all intersections and at the same time the algorithm calculates the mesh overlay structure. However, in the scheme proposed, several meshes may have overlapping edges and edges parallel to the sweep line. Special attention is needed to avoid detrimental effects of rounding errors in these cases. Therefore, it may be more suitable to use other algorithms [67, 68, 69] to achieve the similar or even better efficiency for engineering problems.

The numerical integration schemes used in the present scheme are exact when each of the overlapping meshes is not distorted [1, 59]. For the coupling of two 4-node bilinear elements, the integrand in Equation 4.7 is of order 4. We thus use 6 quadrature points. In the case of a coupling triangle of a 4-node element and a 9-node element, the integrand is of order 6, which requires 12 quadrature points. Similarly, the overlapping of two 9-node elements requires 16 quadrature points to exactly integrate the 8th order integrand [57, 58].

A summary of the proposed procedure is given in Table 6.4. In following sections, the performance of the method of overlapping finite element meshes is demonstrated by some example solutions. Traditional finite element solutions using ADINA are presented for comparison.

Table 6.4: The procedure to compute the stiffness matrix and load vector of overlapping meshes

Procedure The method of overlapping meshes (2D linear elasticity)

1. **Input**: Material properties, domain Ω, and boundary conditions
2. Decompose Ω into m subdomains Ω_i $(i = 1, \ldots, m)$.
3. Mesh each subdomain Ω_i into a traditional, conforming mesh $\mathcal{T}_i$.
4. Calculate the mesh overlay structure. Let T be the list of triangles, Q be the list of non-overlapping elements, V be the list of vertices, and E be the list of edges.
5. Initialize all nodal values of P_i $(i = 1, \ldots, m)$ to 1.
6. For each edge in E:
   - If the edge is on the closure of some interior boundary Γ_i^*:
     - For each of the two end points of the edge: If the end point is a node in $\mathcal{T}_i$, set P_i to 0 at this point.
7. For each vertex in V: Calculate and store the values of weight functions w_i $(i = 1, \ldots, m)$.
8. For each element in Q: Calculate the element stiffness matrix as in traditional finite element analysis.
9. For each triangle in T:
   - For each pair of incident elements:
     - Interpolate the corresponding weight functions using their values on vertices.
     - Evaluate the strain matrices at the quadrature points (see Equation 4.5).
     - Numerically integrate the sub-matrix in Equation 4.7 over this triangle.
10. Assemble the global stiffness matrix.
11. Calculate the force term using Equation 4.8.

6.2.2 The patch test

In Chapter 4, we have mentioned that the proposed scheme passes the constant stress patch tests given proper local interpolations. The problem and overlapping meshes shown in Figure 6-11 are mainly used for validating the code. The rectangular domain is discretized using a blue mesh, a red mesh, and a green mesh. 4-node elements are used in the blue mesh and 9-node elements are used in other two meshes. In this example, the proposed numerical integration scheme fails to yield exact integrations because the meshes used are distorted. The stress solutions give a maximum relative error smaller than 0.03%.

6.2.3 A thin beam problem

In this section, we discuss some solutions using different simple overlapping meshes in a thin beam problem introduced in Section 6.1.2. The beam is given in Figure 5-2. We consider the tip deflection of the free end of the beam, and the Timoshenko beam theory [64] gives a reference solution 0.1081. The numerical solution using six identical regular 4-node elements is 0.0101, which is very inaccurate due to the shear locking. The solution given by six identical regular 9-node finite elements, 0.1070, is much more reasonable.

Coupling of meshes used in different regions

It is reasonable to use a low-order mesh for the region with small stress gradients and a high-order mesh for the region with large stress gradients. Following this idea, we use the overlapping meshes shown in Figure 6-12a. The numerical solution of the tip deflection is 0.1072.

Higher-order elements as enrichments

We also consider placing a higher-order mesh upon a complete mesh of the analysis domain to improve the local accuracy. The overlapping meshes in Figure 6-12b give a tip deflection solution at 0.1044. It is seen that the performance of the 4-node

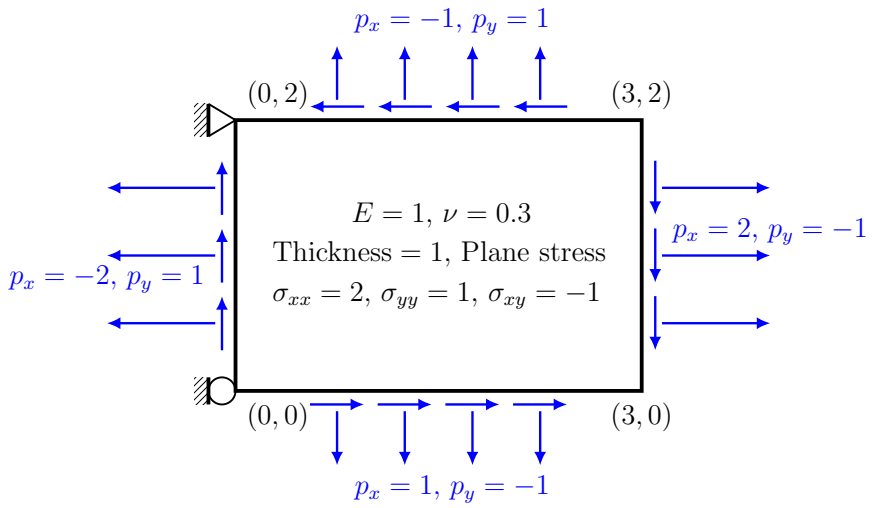

(a) Problem description

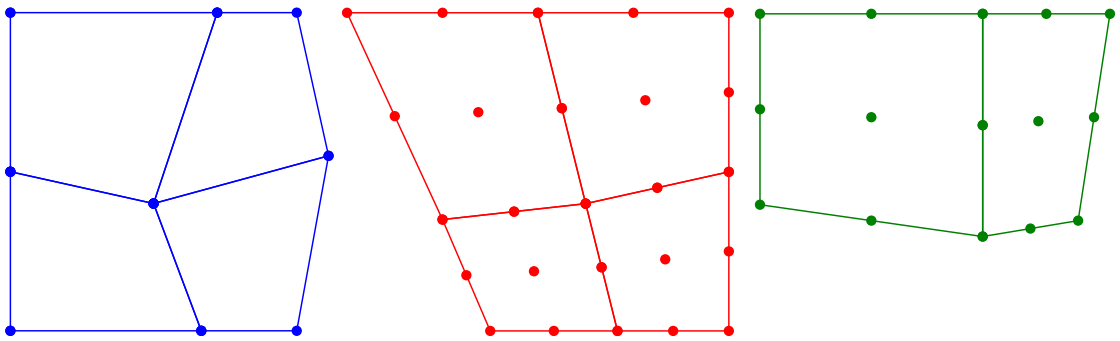

(b) Individual meshes

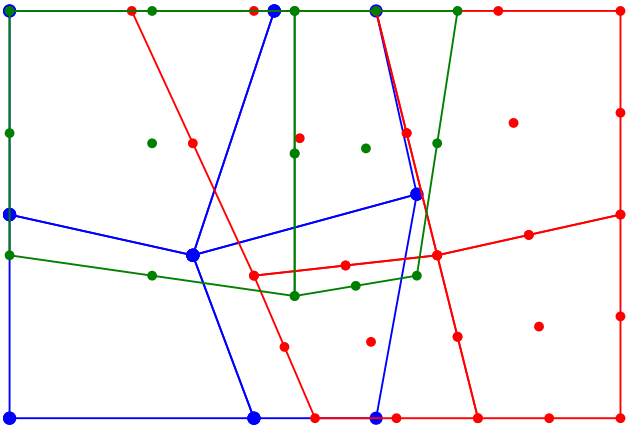

(c) Overlapping meshes

Figure 6-11: A patch test problem and the overlapping meshes

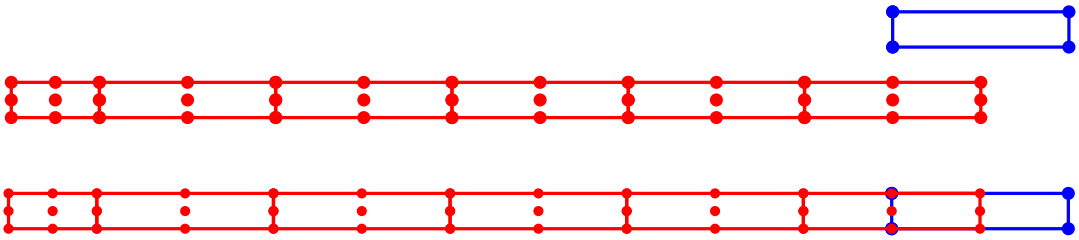

(a) Coupling of two meshes, tip deflection = 0.1072

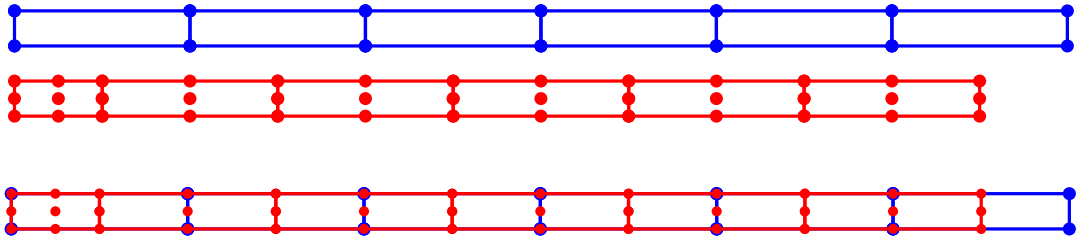

(b) Higher-order elements as enrichments, tip deflection = 0.1044

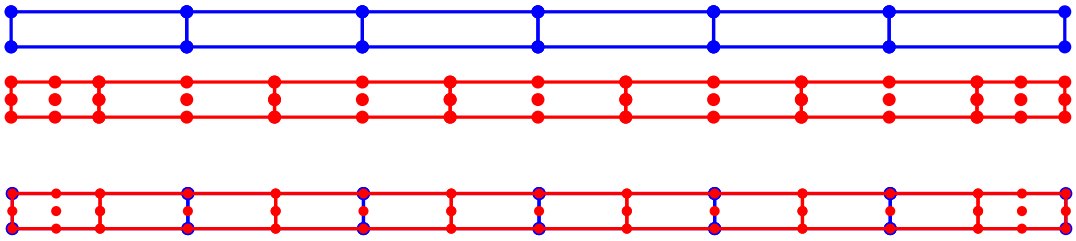

(c) Completely overlapping meshes, tip deflection = 0.1074

Figure 6-12: Different overlapping meshes for the thin beam problem

element mesh is much improved due to the coupling to a higher-order mesh. On the other hand, coupling with lower-order elements actually deteriorates the accuracy of the higher-order mesh. In this example, the coupling interpolation fails to exactly solve an arbitrary quadratic field, while the 9-node element mesh is able to. From the viewpoint of computational efficiency, such use of overlapping meshes is not economical and attractive. However, the convenience of improving the local solution without modifying the base mesh may be promising for adaptation and other special applications.

Completely overlapping meshes

As a special case, if the weight functions all become constants, the final interpolation is just a linear combination of local interpolations with these constant weights. The coupling interpolation now achieves its optimal performance as being more accurate than any individual local interpolation. This case corresponds to using meshes that are completely overlapping, e.g. the meshes shown in Figure 6-12c. The resulting numerical solution is 0.1074.

When a direct sparse solver for symmetric positive definite matrices is preferred, such use should be avoided because the condition we present in Section 4.5 for solvability may be violated.

6.2.4 The AMORE paradigm in the analysis of a plate with two holes

We discuss the numerical solutions to the problem shown in Figure 6-9. The problem and meshes used have been introduced in Section 6.2.1.

Numerical solutions obtained with a traditional 9-node finite element mesh in ADINA are used for comparison. The traditional mesh is given in Figure 6-13 and the solutions are referred to as the "FE solution" in Table 6.5. The reference solutions were calculated in ADINA using a very fine 9-node finite element mesh.

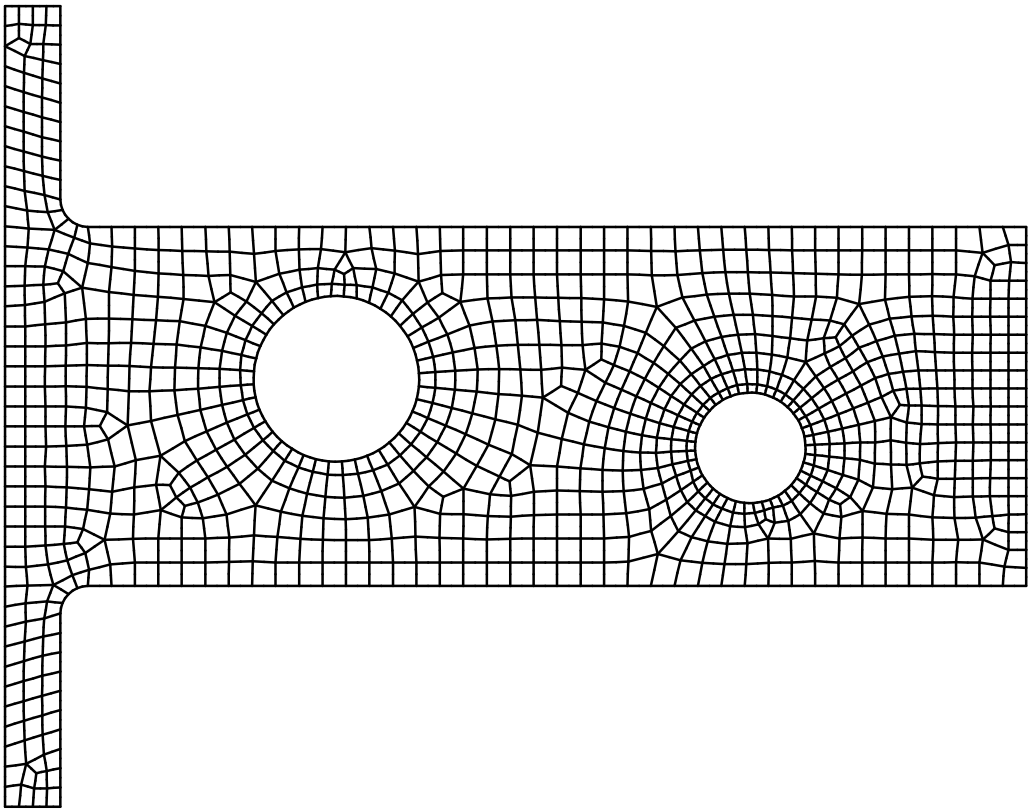

Figure 6-13: A traditional free-form 9-node finite element mesh

We consider in this problem two different choices for the non-overlapping 4-node elements. In the first case we use 4-node finite elements and the solutions are referred to as "AMORE-FE". In the second case 4-node elements with incompatible modes [1, 66] are used instead and the solutions are named "AMORE-ICM". Some numerical solutions can be seen in Table 6.5 and Figure 6-14, where u is the horizontal displacement component, τ_{xx} is the xx-stress component, and $\bar{\tau}$ represents the von Mises effective stress. We note that all stress solutions using AMORE are plotted without stress smoothing.

Table 6.5: Numerical solutions for the plate with two holes

	AMORE-FE	AMORE-ICM	FE solution	Reference
Energy	1.9891	1.9922	1.9870	1.9962
$u_{\max}$	0.11313E−3	0.11332E−3	0.11325E−3	0.11352E−3
$u_{\min}$	−0.10349E−3	−0.10364E−3	−0.10353E−3	−0.10377E−3
$\tau_{xx\,\max}$	18.190E+3	18.205E+3	18.017E+3	19.135E+3
$\tau_{xx\,\min}$	−18.284E+3	−18.295E+3	−18.013E+3	−19.181E+3
$\bar{\tau}_{\max}$	19.124E+3	19.135E+3	18.935E+3	19.673E+3
Number of dofs	3,070	3,070	7,724	>98,000
NNZ*	120,769	120,769	120,690	>1,602,000

*NNZ: Number of non-zero sparse matrix entries

A very important feature of AMORE is that most of the analysis domain is discretized using regular low-order finite elements. In this problem, Figures 6-9 and 6-10 show that most of the analysis domain is discretized by non-overlapping 4-node elements. As a result, the increase in solution effort due to the overlapped regions is reasonable. Indeed, the coupling between meshes results in a larger bandwidth and an increase of the number of non-zero entries in the stiffness matrix (NNZ). If the overlapped regions constitute a small part of the analysis domain – which is the case here – the scheme is quite effective for a given accuracy. We also see from Table 6.5

that the local stress concentrations are well captured by the proposed scheme, since 9-node element meshes are used at these locations to resolve the boundary stress concentrations and curvature. As expected, we see that 4-node incompatible elements are preferred for the non-overlapping part of the interior subdomain.

6.2.5 The AMORE paradigm in the analysis of bracket problems

The suitable number of overlapping meshes generally depends on the geometry and stress distribution of a given problem. Using more meshes gives more freedom so that the meshing effort is further reduced. In this section, we present the solutions to bracket problems using more than two overlapping meshes. However, we note that the increase of number of meshes overlapping at a location may deteriorate the efficiency of the scheme.

A bracket with a hole

We consider in this section an elastic bracket fixed on the left boundary and loaded on its hole. The problem description and meshes used are given in Figure 6-15. A 4-node incompatible element mesh is used for the interior subdomain. And two 9-node finite element meshes are used to discretize the boundary layers. Recall that the incompatible modes are removed for overlapping elements. The proposed numerical solutions are named "AMORE-ICM". For comparison, solutions obtained with 4-node incompatible elements in ADINA are presented, which are named "ICM solution". The reference solutions were calculated using a very fine 9-node element mesh in ADINA. These solutions are given in Table 6.6 and visualized in Figure 6-16.

It is seen from Table 6.6 that the ICM solutions are reasonably accurate. Using a comparable number of dofs, the AMORE-ICM scheme leads to slightly better solutions and the overall performance of AMORE-ICM is promising. The prediction of the maximum effective stress is however not better. Actually, since all stress results are not smoothed using AMORE-ICM, the maximums and minimums are calculated

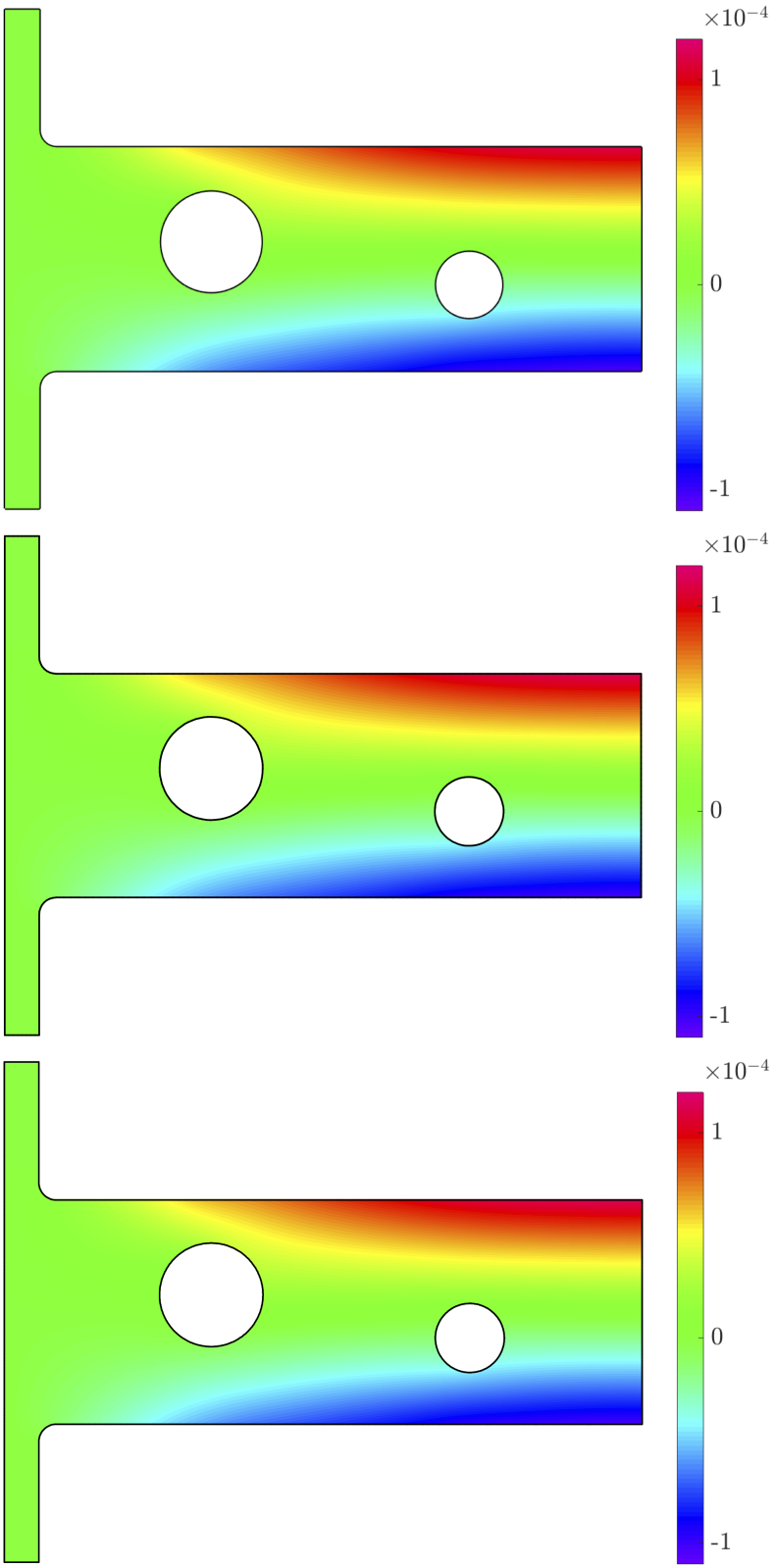

(a) Solutions of u (Top: AMORE-ICM; Middle: FE solution; Bottom: Reference)

Figure 6-14: Numerical solutions for the plate with two holes

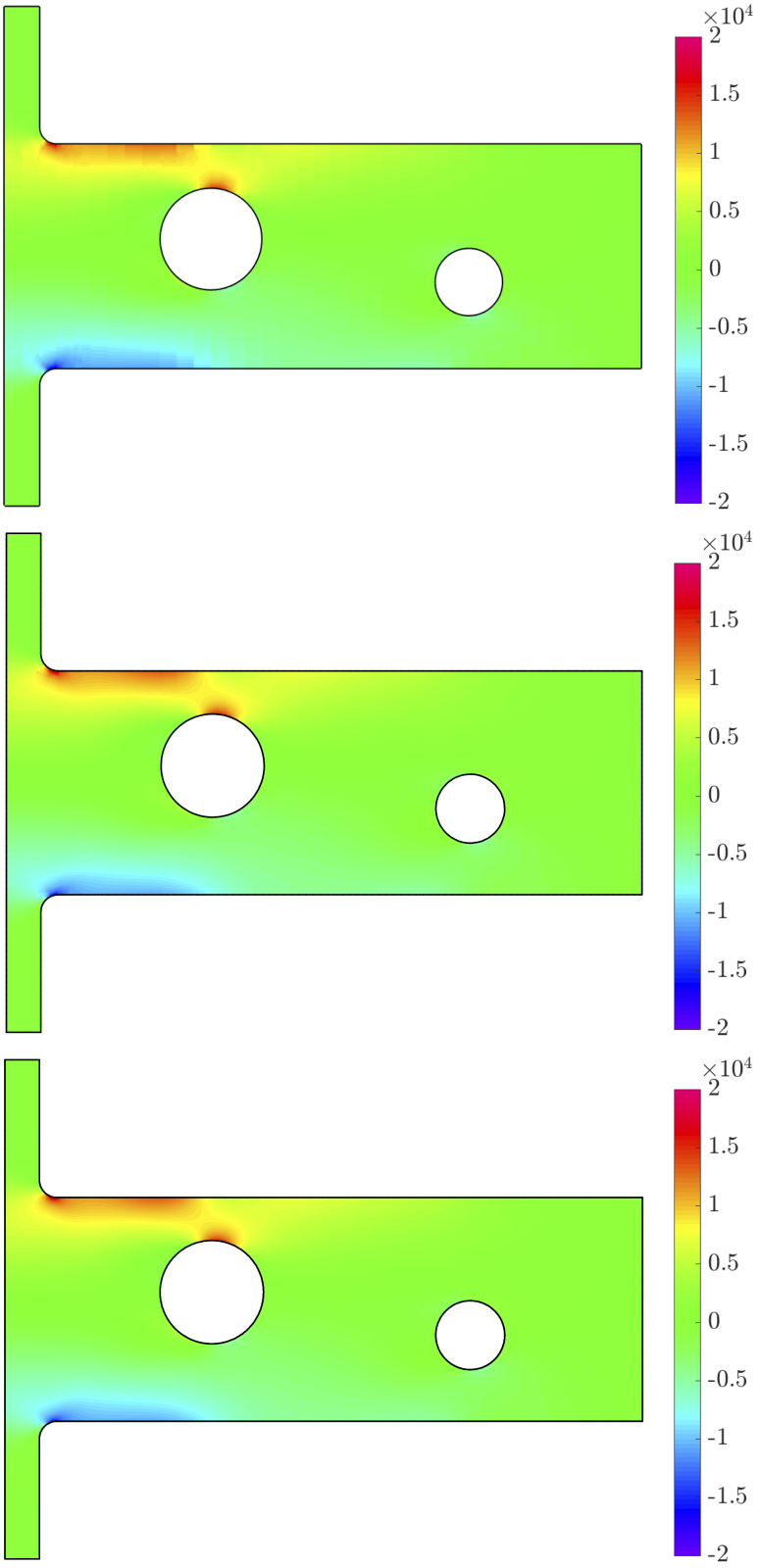

(b) Solutions of τ_{xx} (Top: AMORE-ICM; Middle: FE solution; Bottom: Reference)

Figure 6-14: Numerical solutions for the plate with two holes (continued)

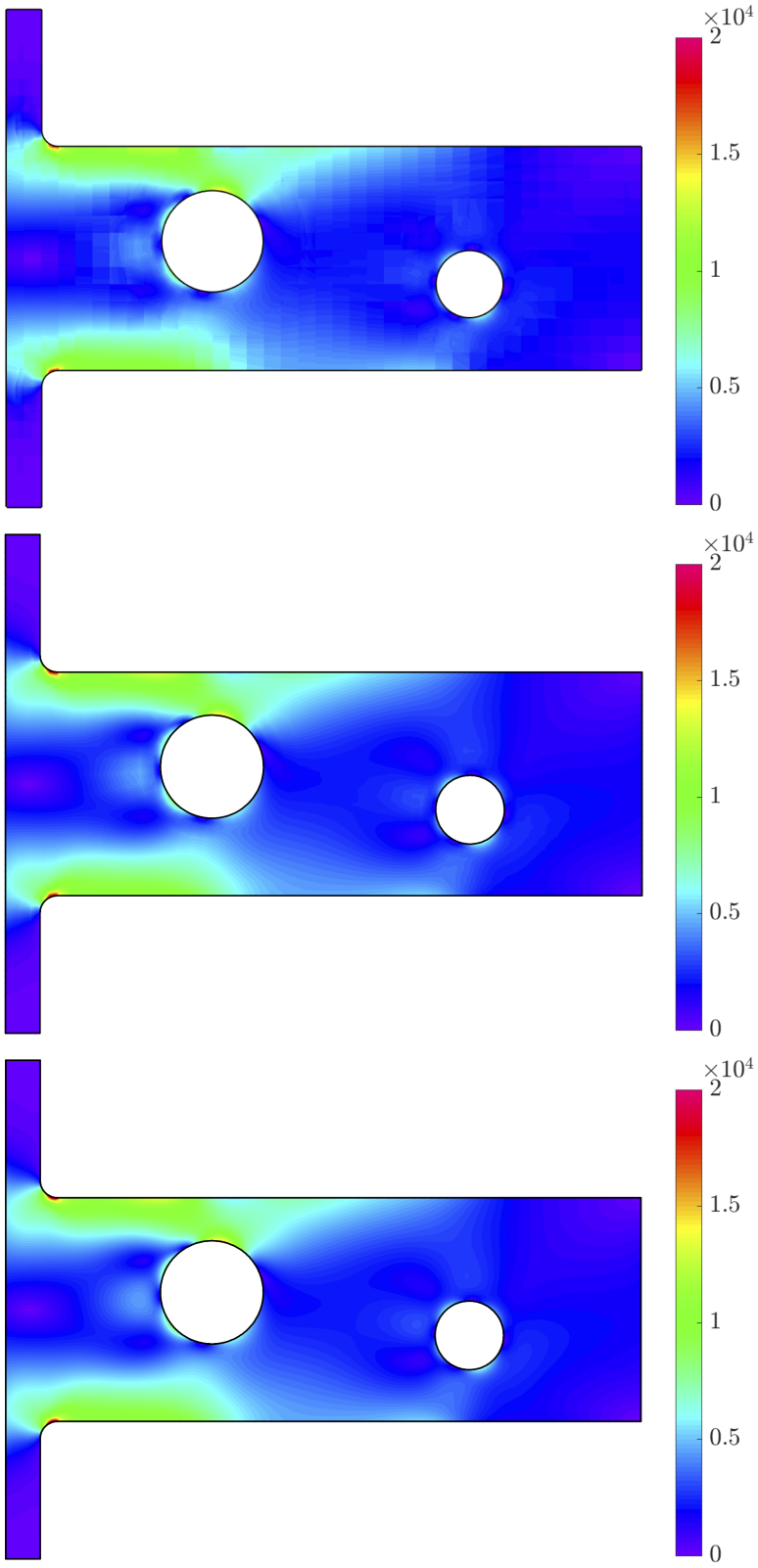

(c) Solutions of $\bar{\tau}$ (Top: AMORE-ICM; Middle: FE solution; Bottom: Reference)

Figure 6-14: Numerical solutions for the plate with two holes (continued)

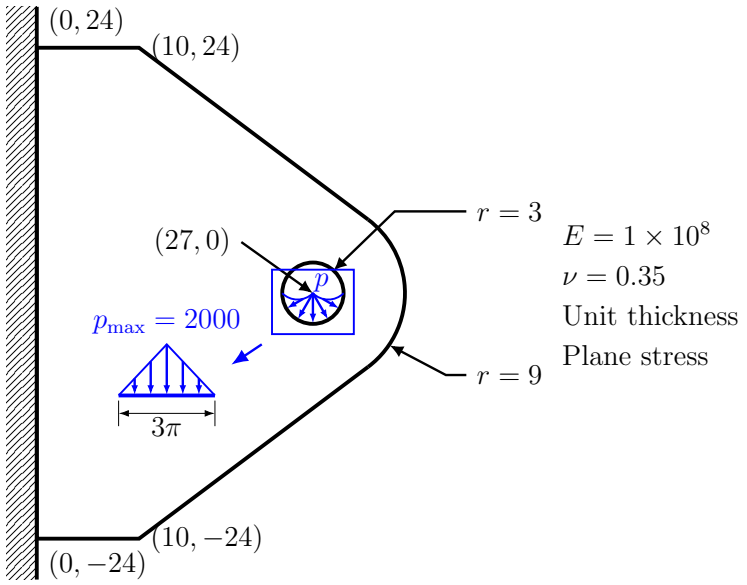

(a) Problem description

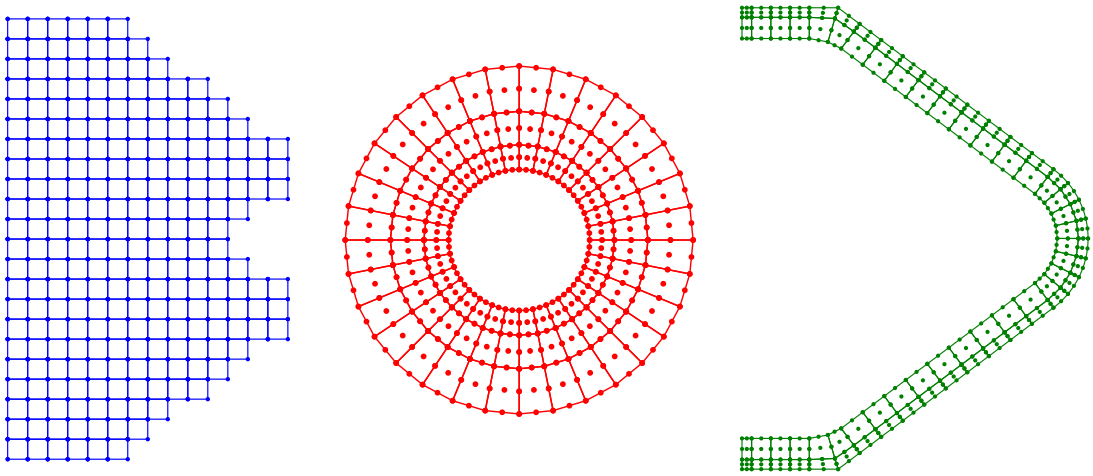

(b) Individual meshes (not to scale)

Figure 6-15: A bracket with a hole

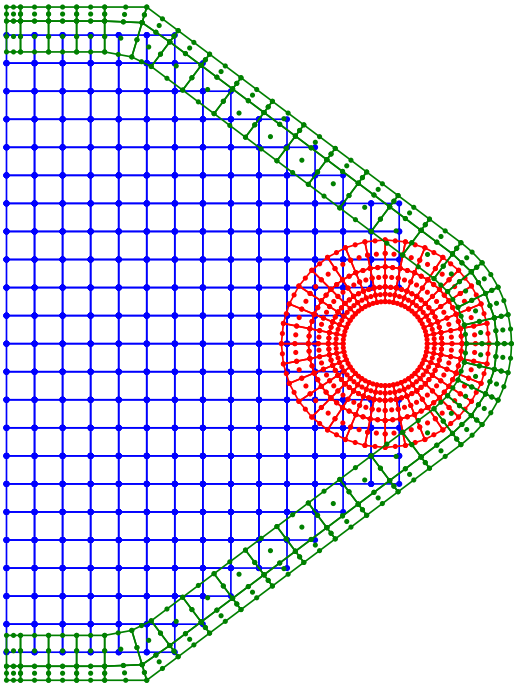

(c) Overlapping meshes

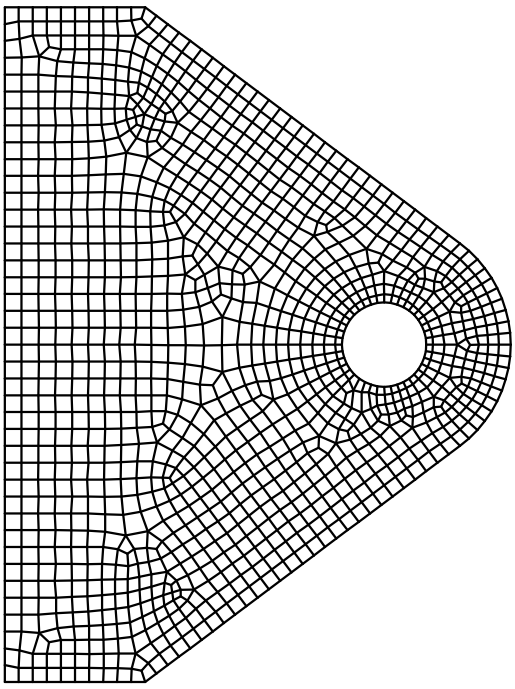

(d) Traditional mesh of 4-node incompatible elements

Figure 6-15: A bracket with a hole (continued)

directly from the displacement solutions, while in ADINA the stress fields are extrapolated from solutions at Gauss points.

Although the AMORE-ICM scheme uses a comparable number of dofs, the number of non-zero sparse matrix entries (NNZ) is much larger, which corresponds to an increase of the solution effort. As discussed before, such increase of NNZ is due to the fact that at most three meshes now overlap at a location. It would be valuable if the scheme can be improved to reduce the NNZ. However the current scheme is still advantageous as an effort to reduce the human effort for meshing.

Table 6.6: Numerical solutions for the bracket with a hole

	AMORE-ICM	ICM solution	Reference
Energy	1.0617	1.0551	1.0630
$v_{\min}$	−0.29732E−3	−0.29597E−3	−0.29777E−3
$\tau_{xy\,\min}$	−1.4079E+3	−1.3531E+3	−1.4560E+3
$\bar{\tau}_{\max}$	2.5129E+3	2.5560E+3	2.5732E+3
Number of dofs	2,156	2,480	>166,000
NNZ*	94,750	22,516	>2,722,000

*NNZ: Number of non-zero sparse matrix entries

A bracket with an inclusion

We also illustrate the potential of using overlapping meshes to simplify the meshing of an analysis domain consisting of different materials. In traditional finite element analysis, the regions of different materials are meshed and these meshes usually match on the interfaces. Schemes involving Lagrange multipliers (like the mesh gluing feature in ADINA) or penalty terms also allow for using non-matching meshes on the interfaces [70, 71, 72]. The proposed scheme may be an interesting alternative.

The bracket considered in this section is geometrically similar to the bracket in the last section. Instead of having a hole, the bracket has a stiff inclusion and is

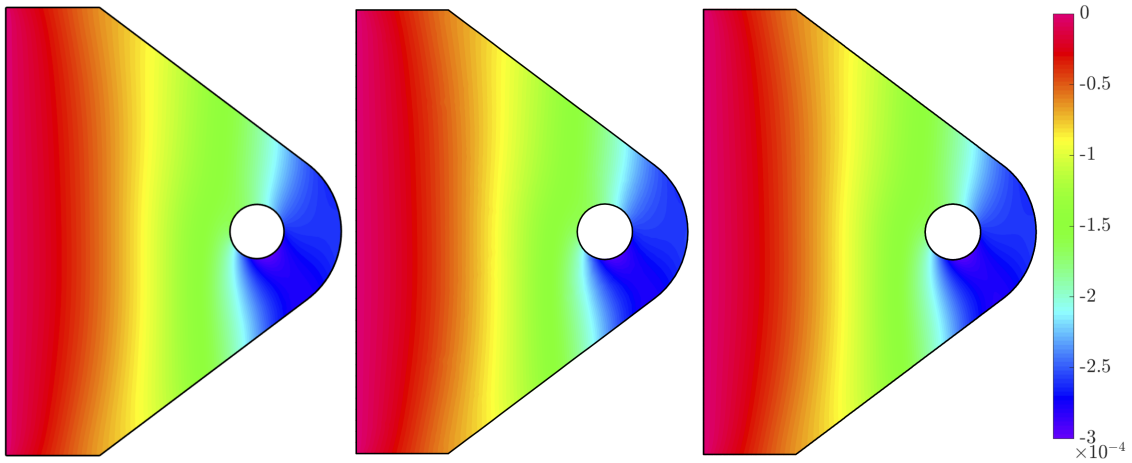

(a) Solutions of v (Left: AMORE-ICM; Middle: ICM solution; Right: Reference)

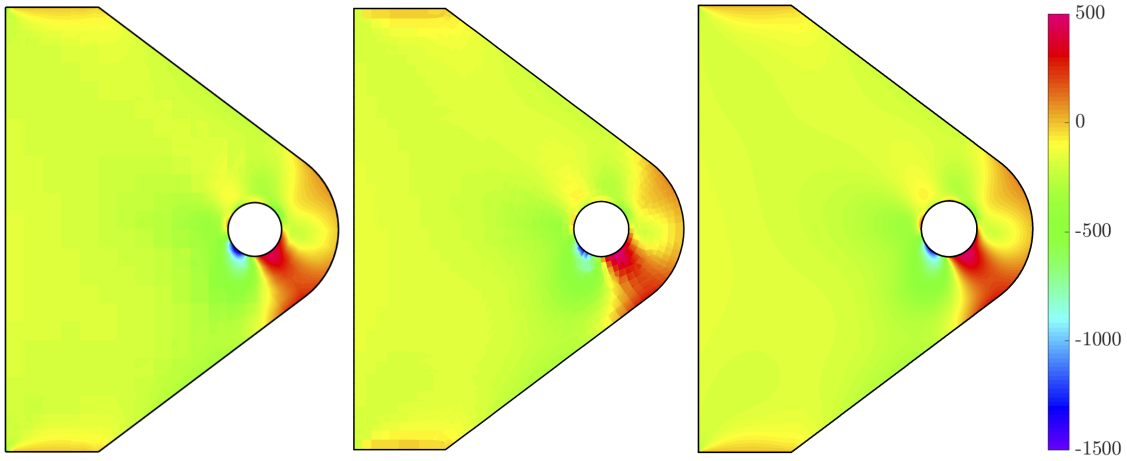

(b) Solutions of τ_{xy} (Left: AMORE-ICM; Middle: ICM solution; Right: Reference)

Figure 6-16: Numerical solutions for the bracket with a hole

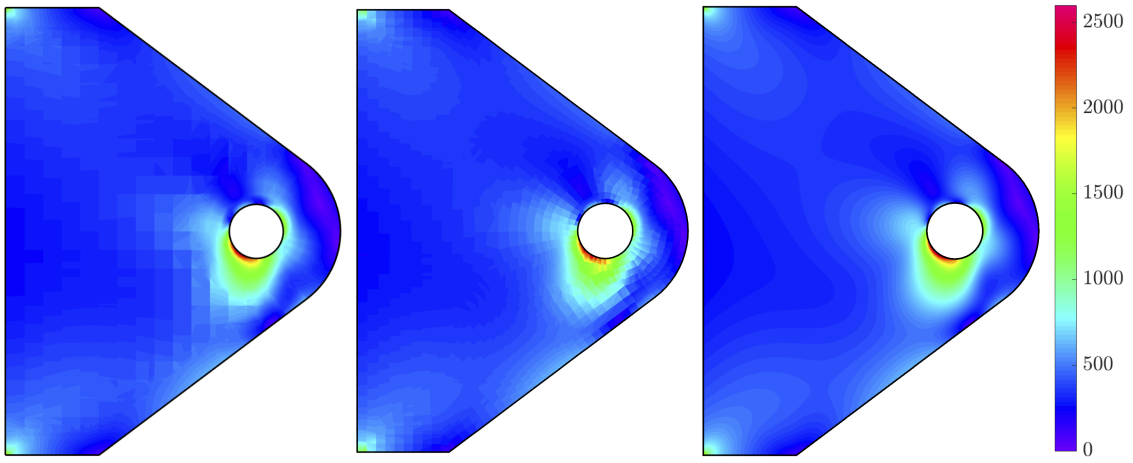

(c) Solutions of $\bar{\tau}$ (Left: AMORE-ICM; Middle: ICM solution; Right: Reference)

Figure 6-16: Numerical solutions for the bracket with a hole (continued)

loaded by a concentrated force at the center of the inclusion. The problem and corresponding meshes can be seen in Figure 6-17. We again use a traditional mesh of 4-node incompatible elements in ADINA for comparison. In this problem, an interface mesh is created along the interface, and overlaps with other meshes that do not touch the interface. For the interior mesh of the inclusion, we use a fine 9-node element mesh.

Solutions to this problem are given in Table 6.7 and Figure 6-18. The reference solutions have been obtained using a very fine 9-node element mesh in ADINA. Of course this problem involves a stress singularity caused by the concentrated external force. Comparing stress solutions at the singularity may be impractical since this can be avoided in engineering by design. However, the distribution of effective stress $\bar{\tau}$ near the loading point may still be interesting, and we see from Figure 6-18 that the proposed scheme leads to a reasonable local solution for the effective stress while the fine traditional mesh of 4-node incompatible elements performs poorly. Since different meshes are independently spanned, we can easily adjust the mesh density inside the inclusion. If the local solution is not important, we can use a coarser interior mesh for the inclusion so as to save computational effort. In this problem, we still have at most three meshes overlapping at a location and as a result, the NNZ using overlapping

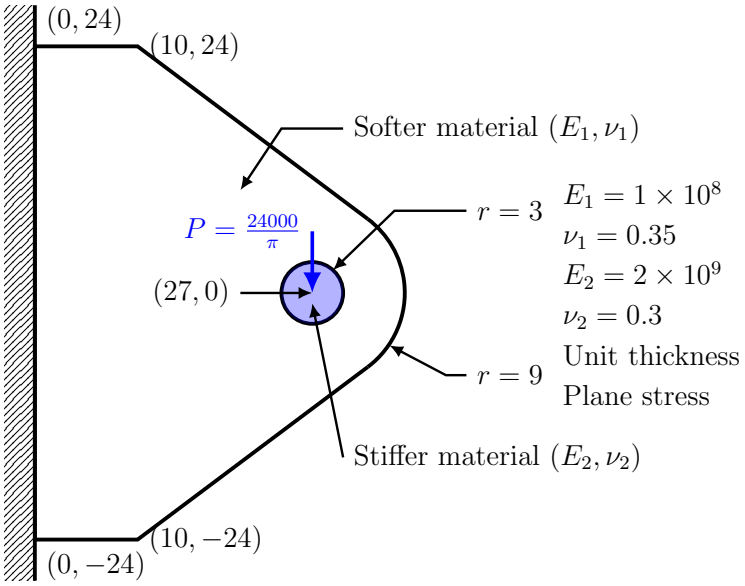

(a) Problem description

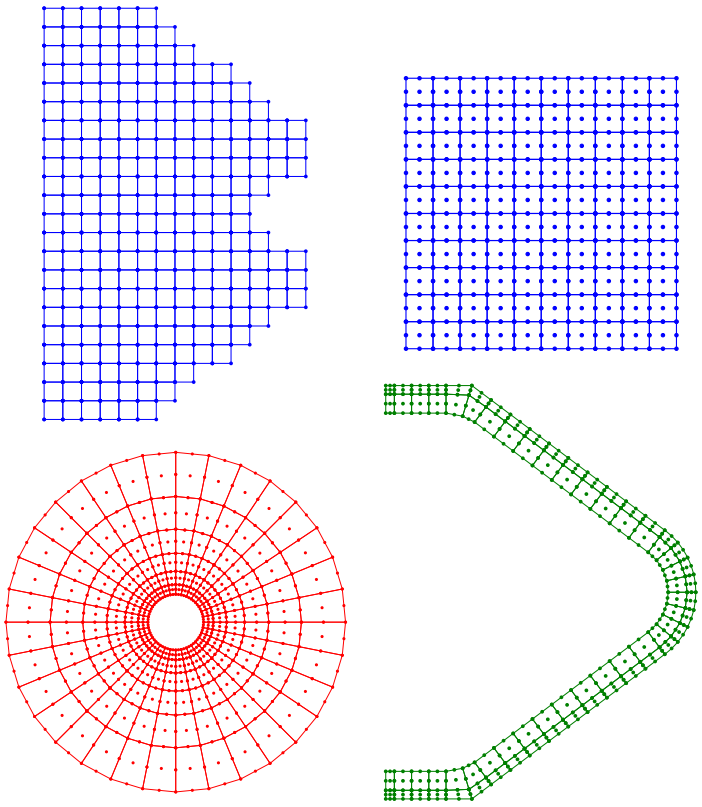

(b) Individual meshes (not to scale)

Figure 6-17: A bracket with a stiff inclusion

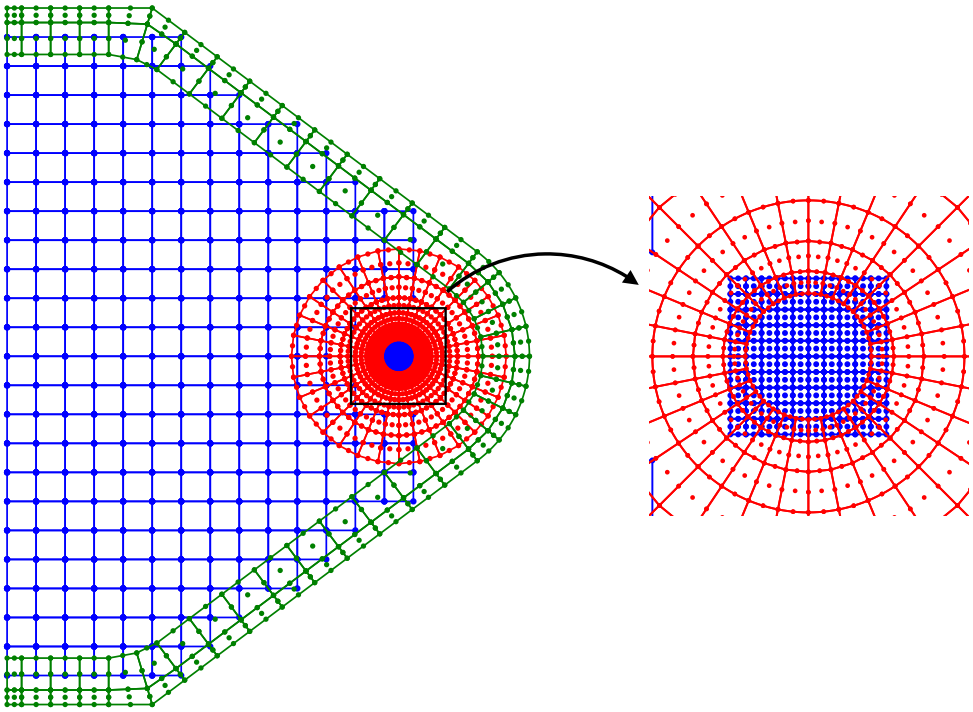

(c) Overlapping meshes

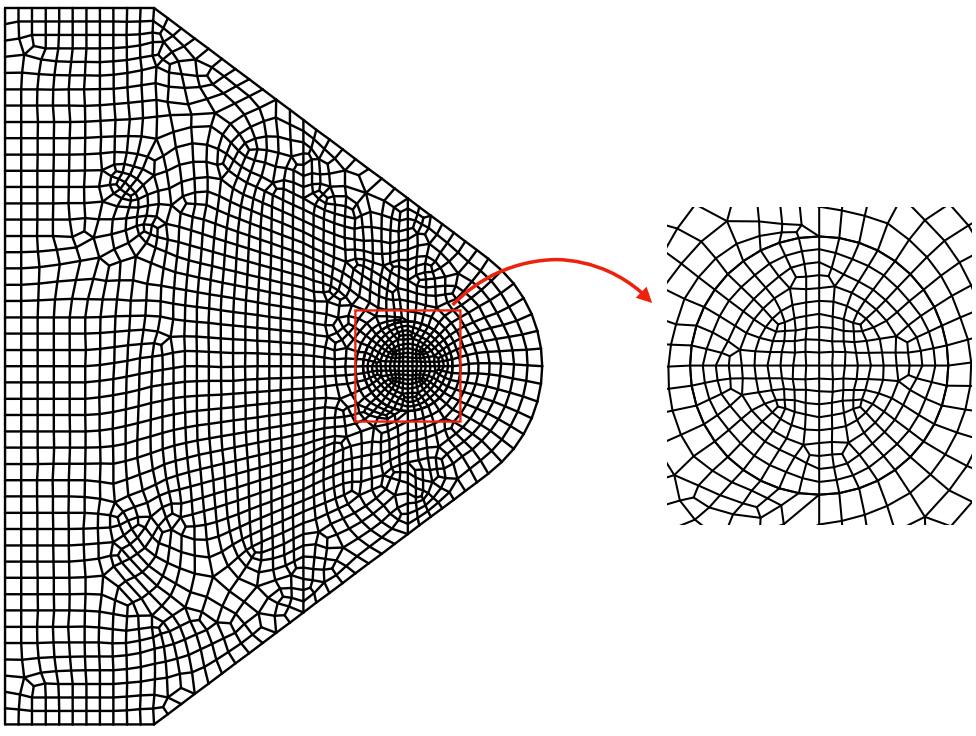

(d) Traditional mesh of 4-node incompatible elements

Figure 6-17: A bracket with a stiff inclusion (continued)

meshes is much larger.

Table 6.7: Numerical solutions for the bracket with a stiff inclusion

	AMORE-ICM	ICM solution	Reference
Energy	0.82215	0.81867	0.83044
$v_{\min}$	−2.4056E−4	−2.4052E−4	−2.4069E−4
$\bar{\tau}_{\max}$	5.0424E+4	1.5969E+4	23.921E+4 ($+\infty$)
Number of dofs	3,806	3,934	>331,000
NNZ*	210,690	36,577	>5,443,000

*NNZ: Number of non-zero sparse matrix entries

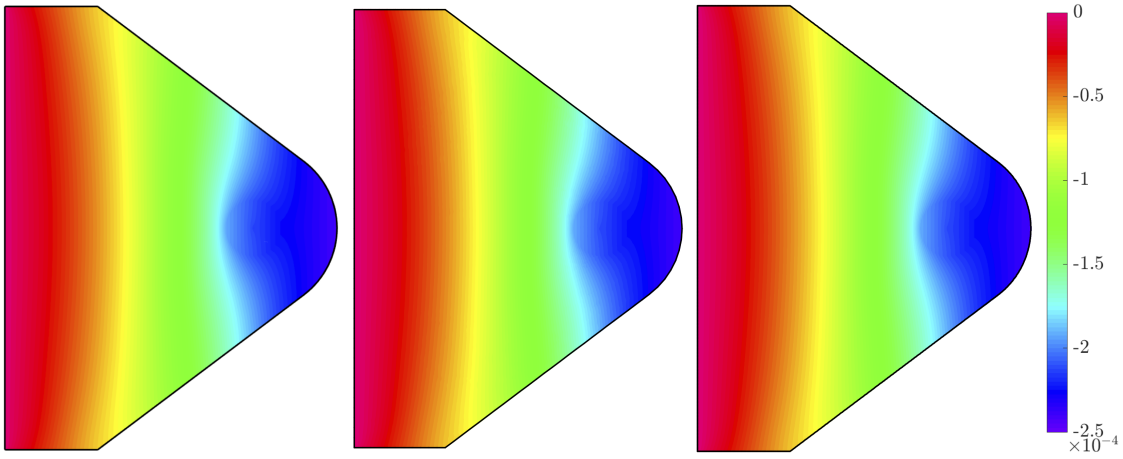

(a) Solutions of v (Left: AMORE-ICM; Middle: ICM solution; Right: Reference)

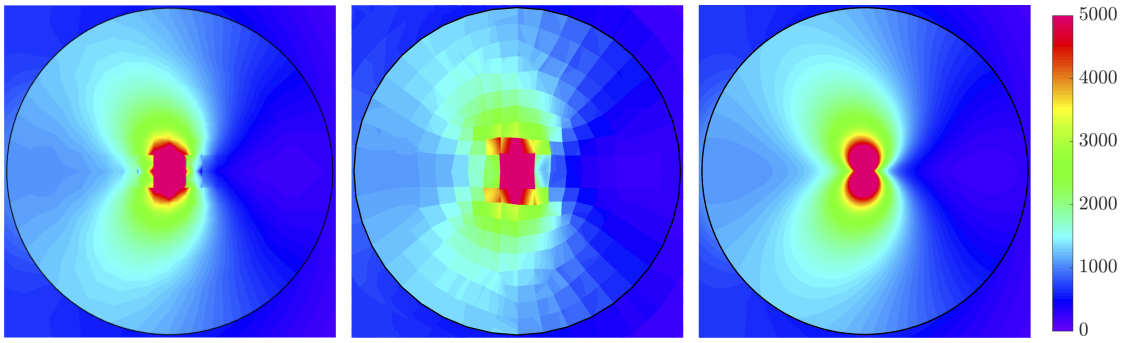

(b) Solutions of $\bar{\tau}$ inside the inclusion (Left: AMORE-ICM; Middle: ICM solution; Right: Reference)

Figure 6-18: Numerical solutions for the bracket with a stiff inclusion

Chapter 7

Conclusions

In this thesis, we proposed two new schemes for finite element analysis in order to reduce the human effort needed for meshing the analysis domain. The new schemes are based on the AMORE paradigm, i.e. regular traditional finite elements are used for the interior of the domain and novel overlapping schemes are used near the boundaries. The new schemes presented mainly serve as alternatives to effectively mesh the boundary regions. With these new interpolation schemes the complete mesh can be generated highly automatically, because, in the first scheme the overlapping elements are insensitive to mesh distortions so that the boundary regions can be meshed with simple rules, and in the second scheme the individual meshes are allowed to overlap freely so that each single mesh can be quite regular and effectively meshed with existing procedures.

7.1 Contributions

1. In the first method, each quadrilateral in the discretized space is formulated as the overlapped region of four polygonal elements. A local field is interpolated on each polygonal element using the method of finite spheres but the Shepard functions are now interpolated using the traditional high-order interpolation to render the numerical integration effective. The re-interpolation also reduces the bandwidth of the final stiffness matrix as the interpolation on each (quadrilat-

eral) element is now only dependent on its nodal dofs. The final interpolation is the weighted average of four local interpolations on each quadrilateral, with the weight functions being the traditional bilinear shape functions. It is seen that the new interpolation scheme combines advantageous aspects from both traditional finite elements and meshless methods, i.e. the elements are insensitive to mesh distortions, the numerical integration effort is much less than that of meshless methods, and the bandwidth structure of the final stiffness matrix is similar to that of traditional elements. The final form of the interpolation is very close to the traditional interpolations, but a major difference is that the nodal knowns in the new scheme are polynomial or other suitable functions instead of single nodal values. Analysis shows that the new interpolation can exactly reproduce high-order polynomial fields provided the basis order is high enough. As a result, the new elements are insensitive to mesh distortions. Consequently, these elements can be used in AMORE to allow fast meshing for the boundary regions. The overlapping elements are indeed seen to be insensitive to mesh distortions and give accurate solutions for the several tested problems.

2. Instead of the overlapping of individual finite elements, we studied in the second scheme the overlapping of complete finite element meshes. In this scheme, the analysis domain is decomposed into several regular subdomains that overlap. On each subdomain, a conforming mesh is spanned and the traditional finite element interpolations are used to construct a local field. In addition, continuous weight functions are automatically computed and form a partition of unity for the complete domain. The final interpolation is the weighted average of local fields and it is compatible. We suggested an efficient implementation based on the plane sweep algorithm. The mesh overlay structure is calculated, the overlapped regions are divided into triangles, and then quadrature schemes for triangles are used. The weight functions are further interpolated by linear functions on each triangle to reduce the numerical integration expense. In the suggested implementation, an undistorted low-order traditional element mesh

is used for the interior subdomain and higher-order meshes are used near the boundaries so as to resolve the boundary stress concentrations and the boundary curvature. Since these meshes (subdomains) are allowed to overlap freely, the meshing process can be highly automated and the local refinement can be achieved efficiently. We see from the solutions of numerical examples that overlapping meshes lead to reasonable overall and local solution accuracy with a reasonable computational effort. We used in the thesis traditional finite elements in each individual mesh. However, the use of more advanced interpolation techniques may make the overlapping meshes more effective.

3. The convergence of new methods was studied. The error bounds provide theoretical evidence for the methods to work in the solution of general problems. In the case of overlapping meshes, it is also seen from the error bound that the overlapped regions should be moderately thick, i.e. the overlapping sizes should be comparable to the overall element size, for the scheme to reach its optimal performance.

7.2 Limitations and outlook

There are still several unsolved problems due to the restricted amount of time.

1. The low-order (first-order) overlapping elements suffer from locking as traditional low-order finite elements. This issue may be tackled by the MITC interpolation technique [1] or other existing techniques for eliminating locking problems. Such techniques may also be used for high-order overlapping elements to further improve the performance. Although the proposed quadratic overlapping elements show no locking in the tested problems, a comprehensive study should be pursued and a mixed formulation may be used to reach an interpolation free from any locking phenomenon.

2. We suggested an implementation for the use of overlapping meshes. The procedure calls the plane sweep algorithm to effectively compute the mesh overlay

structure. In an actual discretization of engineering problem, many overlapping edges and horizontal edges may be found in the overlapping meshes. In such a case, the use of the plane sweep algorithm requires attention on rounding errors. For this reason, the proposed implementation may not be optimal from the practical point of view. Other geometric algorithms [67, 68, 69] should be investigated.

3. We gave simple error bounds for the methods. However, the error bound for overlapping meshes involves the overlapping sizes. While the error bound predicts an increasing solution error for decreasing overlapping sizes, it is found from numerical examples that the solution may converge in the limit case. The current error bound for overlapping meshes is also too rough to explain the coupling effect. A better error bound would be very valuable. In addition, an adaptive refinement procedure using overlapping elements or overlapping meshes may be developed based on a suitable a posteriori error estimate. Although it can be seen that the solution error is bounded in some cases as the overlapping sizes tend to zero, we still do not know if the solution of overlapping meshes really converges to the solution of a certain scheme for non-matching grids. Developing theoretical tools to solve these problems is important for both the completeness of theory and using it to guide applications.

4. We see that, as the overlapping sizes tend to zero, the condition number of the resulting stiffness matrix may grow rapidly. Improving the overlapping interpolation so that the solution procedure remains stable in the limit case is also of much value.

5. The use of overlapping meshes, although saving much human effort for meshing, leads to a larger number of non-zero sparse matrix entries in the stiffness matrix, and thus a larger solution effort. We see that if the number of overlapping meshes remains small and the overlapped regions constitute a small part of the analysis domain, the increase of solution effort is reasonable. In addition, depending on the global numbering, the coupling entries in the stiffness matrix

follow some specific pattern. Special sparse solvers may be developed to make the scheme more effective.

6. Stress recovery procedures are very useful for improving the stress solutions of displacement-based finite elements. In traditional finite elements, the stress solutions at specific local coordinates give higher-order stress accuracy. The new schemes may have similar properties and the corresponding stress recovery procedures should be formulated.

7. The current implementation of overlapping meshes relies on a triangulation of the overlapped regions and quadrature schemes for triangles are used. However, using such quadrature schemes for quadrilaterals is not very effective. A better numerical integration procedure should be pursued.

8. The proposed methods should also be extended for solutions of three-dimensional problems, non-linear problems, fluid and multi-physics problems.

THIS PAGE INTENTIONALLY LEFT BLANK

Appendix A

Triangular Overlapping Finite Elements

The triangular overlapping finite elements were first proposed by Zhang et al. [5]. Here we give a new formulation as a direct application of the concepts introduced in Chapter 3. In addition, the new triangular overlapping elements achieve the global compatibility when they are used together with quadrilateral overlapping elements.

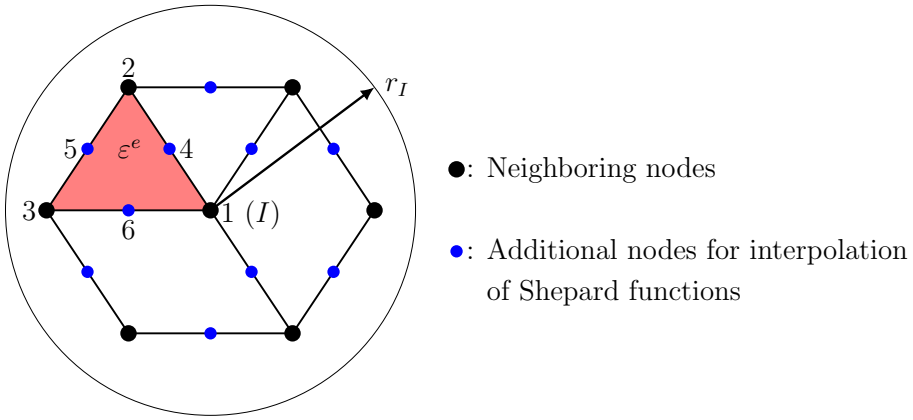

Figure A-1: Interpolation of the Shepard functions on a triangular element ε^e

The formulation is very similar to what we have for quadrilateral overlapping elements. Each triangle is formulated as the overlapped region of three polygonal elements. In each polygonal element D_I, a local field ψ_I is given using the method

of finite spheres, and finally three local fields are combined using traditional shape functions to give the final interpolation on a triangle, i.e.

$$u = \sum_{I=1}^{3} h_I \psi_I \tag{A.1}$$

where h_I is the traditional shape function for 3-node triangular element. The local field ψ_I is interpolated using the (interpolated) Shepard functions:

$$\psi_I(\mathbf{x}) = \sum_{K=1}^{3} \phi_K^I(\mathbf{x}) u_K(\mathbf{x}) \tag{A.2}$$

where ϕ_K^I is the interpolated Shepard function. As for quadrilateral elements, we use mid-edge nodes to achieve the interpolation (see Figure A-1). The interpolated Shepard functions are given by

$$\phi_J^I = \frac{\sqrt{r_I^*}}{\sqrt{r_I} + \sqrt{r_I^*}} \tilde{\phi}_J^I + \frac{\sqrt{r_I}}{\sqrt{r_I} + \sqrt{r_I^*}} \delta_{IJ} \tag{A.3}$$

where the radii r_I and r_I^* are defined similarly as for quadrilateral elements, δ_{IJ} is the Kronecker delta, and

$$\tilde{\phi}_J^I(\mathbf{x}) = \sum_{i=1}^{6} \hat{h}_i(\mathbf{x}) \hat{\phi}_{Ji}^I \tag{A.4}$$

where $\hat{h}_i$ is a shape function for the 6-node triangular finite element, and the coefficients are listed in Table A.1. These coefficients are determined based on the criteria given in Chapter 3. In addition, the coefficients lead to a continuous interpolation if triangular and quadrilateral overlapping elements are used in the same mesh, e.g. an AMORE mesh with both types of overlapping elements.

Table A.1: Interpolation of the Shepard functions on a triangular element (see Figure A-1)

$\tilde{\phi}_1^I = \sum_{i=1}^{6} \hat{h}_i \hat{\phi}_{1i}^I$		
$\hat{\phi}_{11}^I$	$\hat{\phi}_{12}^I$	$\hat{\phi}_{13}^I$
1	$\frac{W_1}{W_1+W_2}\Big\|_{\mathbf{x}_2}$	$\frac{W_1}{W_1+W_3}\Big\|_{\mathbf{x}_3}$
$\hat{\phi}_{14}^I$	$\hat{\phi}_{15}^I$	$\hat{\phi}_{16}^I$
$\frac{W_1}{W_1+W_2}\Big\|_{\mathbf{x}_4}$	$\frac{W_1}{W_1+W_2+W_3}\Big\|_{\mathbf{x}_5}$	$\frac{W_1}{W_1+W_3}\Big\|_{\mathbf{x}_6}$
$\tilde{\phi}_2^I = \sum_{i=1}^{6} \hat{h}_i \hat{\phi}_{2i}^I$		
$\hat{\phi}_{21}^I$	$\hat{\phi}_{22}^I$	$\hat{\phi}_{23}^I$
0	$\frac{W_2}{W_1+W_2}\Big\|_{\mathbf{x}_2}$	0
$\hat{\phi}_{24}^I$	$\hat{\phi}_{25}^I$	$\hat{\phi}_{26}^I$
$\frac{W_2}{W_1+W_2}\Big\|_{\mathbf{x}_4}$	$\frac{W_2}{W_1+W_2+W_3}\Big\|_{\mathbf{x}_5}$	0
$\tilde{\phi}_3^I = \sum_{i=1}^{6} \hat{h}_i \hat{\phi}_{3i}^I$		
$\hat{\phi}_{31}^I$	$\hat{\phi}_{32}^I$	$\hat{\phi}_{33}^I$
0	0	$\frac{W_3}{W_1+W_3}\Big\|_{\mathbf{x}_3}$
$\hat{\phi}_{34}^I$	$\hat{\phi}_{35}^I$	$\hat{\phi}_{36}^I$
0	$\frac{W_3}{W_1+W_2+W_3}\Big\|_{\mathbf{x}_5}$	$\frac{W_3}{W_1+W_3}\Big\|_{\mathbf{x}_6}$

THIS PAGE INTENTIONALLY LEFT BLANK

Appendix B

Geometric Algorithms

B.1 The doubly-connected edge list

In traditional finite element analysis, the nodes and elements are linked via a connectivity list. A finite element mesh can be simply stored as a list of nodes and a list of elements. In the method of overlapping finite element meshes, more information is maintained in order to effectively compute the mesh overlay structure.

For simplicity, we consider a mesh as a collection of straight line segments. Calculating the intersection of two curved edges is not considered in the proposed scheme because it is reasonable to assume that curved edges only occur on boundaries. Each finite element mesh contains nodes, edges, and elements. To generalize the concept of node, a vertex is defined to be a finite element node from some mesh, or an intersection of edges from different meshes. Generally, a face is a maximal connected subset of the plane that does not contain any point from an edge or a vertex. Each element can be seen as a face in its own mesh. The exterior domain is also a face by definition. The planar subdivision induced by several overlapping meshes is therefore composed of polygons (polygonal faces). This planar subdivision is referred to as the mesh overlay. We say a vertex and an edge are incident to each other if the vertex is an end point of the edge. Similarly, an edge or a vertex on the boundary of a face is incident to this face, and vice versa.

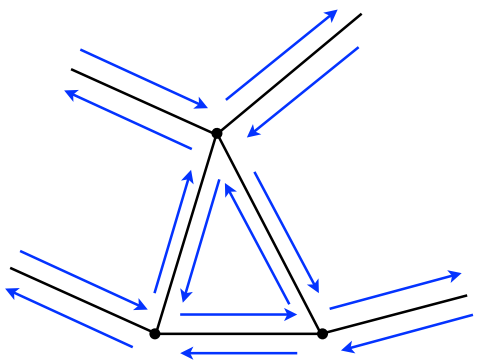

Figure B-1: The doubly-connected edge representation of a planar subdivision

We adopt the doubly-connected edge representation of a mesh in order to conveniently access the incident edges of a vertex, incident faces of an edge, etc. A doubly-connected edge list is defined as follows. As can be seen from Figure B-1, each edge is represented by a pair of directed edges, which are of opposite orientations. Each directed edge is called a half edge, and the pair of half edges is called twins. Each half edge of course has an origin and a destination. Furthermore, each half edge has a pointer to its twin half edge. Since we split an edge into two half edges, we define that each half edge is only incident to the face on its left. Similarly, a half edge is only incident to its origin. In order to have each loop of half edges represent a face, we also maintain for each half edge a next half edge and a previous half edge. By doing so, we can traverse the boundary of a face by starting from an arbitrary incident half edge and iteratively visiting the next half edge till some edge is repeated.

In summary, each vertex has pointers to its coordinates and one of its incident half edges; each half edge has pointers to its twin, incident face, origin, destination, next half edge, and previous half edge; each face has a pointer to one of its incident half edges. In addition, we need to store all incident elements for each face, i.e. all elements that are coupling on this face.

B.2 The plane sweep algorithm

As usual, we define a Cartesian coordinate system (x, y) for the plane, where the x-axis points to the right and the y-axis points to the top. The idea of the plane sweep algorithm is to imagine a line sweeping towards a fixed direction and visiting all vertices one-by-one. In this section, we assume that the sweep line is horizontal and moves from the top to the bottom. Whenever the sweep line visits a node or an intersection, the algorithm tries to find some new intersections that are to be visited. It can be proved that all intersections will be found when the algorithm terminates [55, 56]. If additional work is done at each vertex, the algorithm further returns a valid doubly-connected edge representation for the mesh overlay of overlapping meshes.

In the algorithm, we maintain a set of points called the event queue Q, of which the members are called event points, and a set of line segments called the status S. The event queue initially contains all nodes from the overlapping meshes. As the algorithm runs, new intersections are found and added into the event queue. Whenever the sweep line visits an event point, this point is removed from Q. Therefore, all current members of Q are below the sweep line. The set S contains all edges that currently intersect with the sweep line. A brief example is shown in Figure B-2.

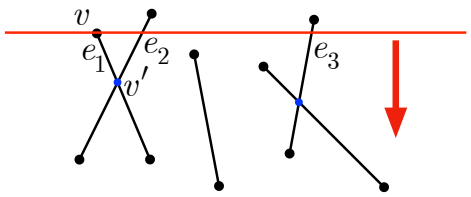

Figure B-2: An example for the plane sweep algorithm

We see from Figure B-2 that the red sweep line arrives at the vertex v. The current status contains three edges e_1, e_2, and e_3. The algorithm tests several neighboring edges of v in S and decides if any pair of edges have a new intersection below the sweep line. In this simple example, the intersection v' of edges e_1 and e_2 is found. This new intersection is then added into the event queue and the sweep line moves downwards

to the next position. Some vertices may have exactly the same y-coordinate. For such a special case, we imagine that the sweep line is slightly slanted and has a positive infinitesimal slope. Vertices with the same y-coordinate are then visited from the left to the right. Formally, we are defining an order relation: we say two vertices $v_1 = (x_1, y_1)$ and $v_2 = (x_2, y_2)$ satisfying $v_1 < v_2$ if $y_1 < y_2$ or $y_1 = y_2$ and $x_1 > x_2$. The data structure in Q is required to support fast operations including searching an event point, inserting new event points, and extracting the maximum element currently in Q, i.e. the next position to visit. The event queue can be implemented using an AVL tree or any other suitable balanced binary search tree [73]. Similarly, the edges in S are ordered by their intersections with the sweep line because we need to test if any pair of adjacent edges near the current event point have a new intersection below the sweep line. Whenever the horizontal line leaves its current position and visits a new event point, some edges in S no longer intersect the sweep line and should be removed from S. At the meanwhile, some edges should be added into S. For maintaining the order relation of members in S as well as enabling fast operations including searching neighboring edges, inserting edges, and deleting edges, the AVL tree can also be used for implementing S. Note that some edges in S may intersect the horizontal line at the same position. In this case, the order is defined by the intersections after moving the sweep line infinitesimally forward. The slopes of these edges thus come into play.

So far we have only introduced how all intersections are found. To obtain a valid doubly-connected edge representation for the mesh overlay, we need to fix the connectivity at each event point so that each loop of half edges still represents a face in the mesh overlay. As can be seen in Figure B-3, on the blue mesh, the next half edge of e_1 is e_2. However, in the mesh overlay, the next half edge of e_1 is actually the edge e_3 (in the red mesh).

Since we need to calculate the incident elements of each polygon in the mesh overlay, additional information is stored for each event point v. This additional information is an m-dimensional array named *LeftList*, where each entry corresponds to a mesh. If a mesh is involved at v, i.e. there exists an edge touching v from

this mesh, one of the half edges originating from v and from this mesh is stored in the corresponding entry of *LeftList*. If a mesh is not involved at v, we define $S_i = \{e \mid e \in S \text{ and } e \text{ is an edge in the } i\text{th mesh}\}$. Then we store in the ith entry of *LeftList* the edge in S_i that locates immediately to the left of v. The use of *LeftList* for obtaining the information of incident elements is straightforward. Such additional information can be collected during the main algorithm.

The algorithm for computing a mesh overlay induced by overlapping meshes is summarized in Table B.1.

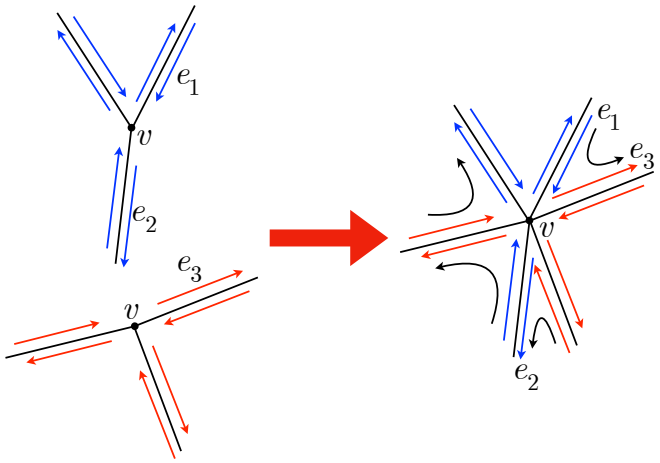

Figure B-3: Fixing the connectivity of half edges

B.3 A simple algorithm for polygon triangulation

Triangulating a simple polygon is a classical problem in computational geometry. The difficulty is only addressed when the number of vertices is very large. In fact, a polygon with m vertices can be triangulated within $O(m \ln m)$ time [55]. This actually ensures that the total runtime for calculating the mesh overlay and the triangulation can be achieved within $O(n \ln n)$ time, where n is the complexity of the mesh overlay.

However, a polygon occurring in a mesh overlay of overlapping finite element meshes does not tend to have many vertices as long as all overlapping meshes have close element sizes. Noticing this, we use a simple $O(m^2)$ algorithm to triangulate

Table B.1: The plane sweep algorithm for computing the mesh overlay of overlapping meshes

Algorithm Mesh overlay

1. **Input**: Several conforming finite element meshes
2. Convert the meshes into their doubly-connected edge forms.
3. Add all finite element nodes into the event queue Q. Initialize the status S to an empty set. Initialize the set V of visited event points to an empty set.
4. While Q is not empty:
   - Extract the maximum event point v from Q (and remove it from Q).
   - Insert v into V.
   - Initialize the array *LeftList* of v to an array with m empty entries.
   - Let $L(v)$ be the set of edges that have v as a lower (less in the special order) end point. Let $U(v)$ be the set of edges that have v as a higher (greater in the order) end point. Let $C(v)$ be the set of edges that have v in the interior.
   - For each edge in $C(v)$:
     - Split the edge at v into two edges, and update $L(v)$ and $U(v)$ accordingly.
   - Fill in the array *LeftList* using these involved edges in $L(v) \cup U(v)$. [Note that for each mesh, we just choose an arbitrary involved (half) edge originating from v. Some meshes are not involved at v, so some entries in *LeftList* have not yet been filled in.] Store in remaining entries the edges that locate immediately to the left of v from these meshes, as explained. [Some entries may still be empty.]
   - Delete edges in $L(v)$ from the status.
   - Insert edges in $U(v)$ into the status.

Table B.1: The plane sweep algorithm for computing the mesh overlay of overlapping meshes (continued)

Algorithm Mesh overlay

4. • If $U(v)$ is empty:
   – Find the edge in S that locates immediately to the left of v. Find the edge in S that locates immediately to the right of v. Test if these two edges have an intersection less than v. If they have and the intersection is not currently in Q, insert it into Q.

   Else:
   – Find the leftmost edge in $U(v)$ and the edge in S that locates immediately to the left of v. Test if these two edges have an intersection less than v. If they have and the intersection is not currently in Q, insert it into Q.
   – Find the rightmost edge in $U(v)$ and the edge in S that locates immediately to the right of v. Test if these two edges have an intersection less than v. If they have and the intersection is not currently in Q, insert it into Q.

5. For each vertex in V:
   • Modify the connectivity between half edges at this vertex as explained.

6. Traverse all half edges to find loops. [Each loop represents a polygon in the mesh overlay.] Create a new (polygonal) face for each loop and use the arrays *LeftList* to find the set of incident elements for each polygon.

each polygon [55]. As can be seen in Figure B-4, we first find the maximum vertex v of the polygon. Denote by v' and v'' the two neighboring vertices of v. If the edge $\overline{v'v''}$ is contained in the polygon, the original polygon is divided into two smaller polygons by the edge $\overline{v'v''}$. If $\overline{v'v''}$ is not contained in the polygon, some vertices must be inside the triangle $\Delta vv'v''$. Assume v''' is the vertex in $\Delta vv'v''$ that is the farthest away from the line through $\overline{v'v''}$. It can be seen that the edge $\overline{vv'''}$ must be completely contained in the polygon. In either case, we succeed in dividing the polygon into two smaller polygons. Recursively doing so yields a triangulation of the polygon. The runtime is $O(m^2)$ since each split costs linear time and we can draw at most $O(m)$ additional edges. The recursive algorithm is summarized in Table B.2.

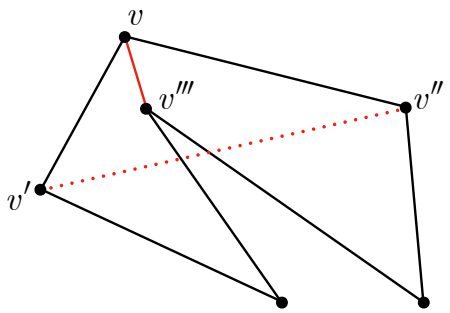

Figure B-4: A simple algorithm for polygon triangulation

Table B.2: The algorithm for polygon triangulation

Algorithm Polygon triangulation

1. **Input**: Doubly-connected edge representation of a polygon
2. If the polygon is a triangle, return.
3. Find the maximum vertex v and its two neighboring vertices v' and v''.
4. Find all vertices insider the triangle $\Delta vv'v''$ (see Figure B-4) and calculate their distances to the line through $\overline{v'v''}$.
5. If no vertex locates inside the triangle $\Delta vv'v''$:
   - Split the polygon into two polygons by the edge $\overline{v'v''}$.

   Else:
   - Find among all vertices inside the triangle $\Delta vv'v''$ the vertex v''' that is the farthest away from the line through $\overline{v'v''}$.
   - Split the polygon into two polygons by the edge $\overline{vv'''}$.
6. Recursively call the algorithm on these two smaller polygons.

THIS PAGE INTENTIONALLY LEFT BLANK

Bibliography

[1] KJ Bathe. *Finite element procedures*. KJ Bathe, Watertown, MA, 2nd edition, 2014. And Higher Education Press, China, 2016.

[2] KJ Bathe. The finite element method with "overlapping finite elements". In A Zingoni, editor, *Proceedings sixth international conference on structural engineering, mechanics and computation – SEMC 2016*, Cape Town, South Africa, 2016.

[3] KJ Bathe and L Zhang. The finite element method with overlapping elements – A new paradigm for CAD driven simulations. *Computers & Structures*, 182:526–539, 2017.

[4] L Zhang and KJ Bathe. Overlapping finite elements for a new paradigm of solution. *Computers & Structures*, 187:64–76, 2017.

[5] L Zhang, KT Kim, and KJ Bathe. The new paradigm of finite element solutions with overlapping elements in CAD – Computational efficiency of the procedure. *Computers & Structures*, 199:1–17, 2018.

[6] J Huang and KJ Bathe. Quadrilateral overlapping elements and their use in the AMORE paradigm. *Computers & Structures*, 222:25–35, 2019. DOI: 10.1016/j.compstruc.2019.05.011.

[7] KJ Bathe. The AMORE paradigm for finite element analysis. *Advances in Engineering Software*, 130:1–13, 2019.

[8] J Huang and KJ Bathe. Overlapping finite element meshes in AMORE. *Advances in Engineering Software*, 144:102791, 2020. DOI: 10.1016/j.advengsoft.2020.102791.

[9] S De and KJ Bathe. The method of finite spheres. *Computational Mechanics*, 25(4):329–345, 2000.

[10] S De and KJ Bathe. The method of finite spheres with improved numerical integration. *Computers & Structures*, 79(22–25):2183–2196, 2001.

[11] JW Hong and KJ Bathe. Coupling and enrichment schemes for finite element and finite sphere discretizations. *Computers & Structures*, 83(17–18):1386–1395, 2005.

[12] B Lai and KJ Bathe. The method of finite spheres in three-dimensional linear static analysis. *Computers & Structures*, 173:161–173, 2016.

[13] KT Kim, L Zhang, and KJ Bathe. Transient implicit wave propagation dynamics with overlapping finite elements. *Computers & Structures*, 199:18–33, 2018.

[14] G Chesshire and WD Henshaw. Composite overlapping meshes for the solution of partial differential equations. *Journal of Computational Physics*, 90(1):1–64, 1990.

[15] JL Steger and JA Benek. On the use of composite grid schemes in computational aerodynamics. *Computer Methods in Applied Mechanics and Engineering*, 64(1–3):301–320, 1987.

[16] JA Benek, PG Buning, and JL Steger. A 3-D Chimera grid embedding technique. In *7th Computational Physics Conference*, Cincinnati, OH, 1985.

[17] T Belytschko, YY Lu, and L Gu. Element-free Galerkin methods. *International Journal for Numerical Methods in Engineering*, 37(2):229–256, 1994.

[18] WK Liu, S Jun, and YF Zhang. Reproducing kernel particle methods. *International Journal for Numerical Methods in Fluids*, 20(8–9):1081–1106, 1995.

[19] GR Liu. *Meshfree methods: Moving beyond the finite element method.* CRC Press, Boca Raton, FL, 2nd edition, 2010.

[20] JS Chen, C Pan, CT Wu, and WK Liu. Reproducing kernel particle methods for large deformation analysis of non-linear structures. *Computer Methods in Applied Mechanics and Engineering*, 139(1–4):195–227, 1996.

[21] WK Liu, S Li, and T Belytschko. Moving least-square reproducing kernel methods (I) Methodology and convergence. *Computer Methods in Applied Mechanics and Engineering*, 143(1–2):113–154, 1997.

[22] T Belytschko, Y Guo, WK Liu, and SP Xiao. A unified stability analysis of meshless particle methods. *International Journal for Numerical Methods in Engineering*, 48(9):1359–1400, 2000.

[23] S Beissel and T Belytschko. Nodal integration of the element-free Galerkin method. *Computer Methods in Applied Mechanics and Engineering*, 139(1–4):49–74, 1996.

[24] T Belytschko, Y Krongauz, D Organ, M Fleming, and P Krysl. Meshless methods: An overview and recent developments. *Computer Methods in Applied Mechanics and Engineering*, 139(1–4):3–47, 1996.

[25] JS Chen, CT Wu, S Yoon, and Y You. A stabilized conforming nodal integration for Galerkin mesh-free methods. *International Journal for Numerical Methods in Engineering*, 50(2):435–466, 2001.

[26] I Babuška, U Banerjee, JE Osborn, and Q Li. Quadrature for meshless methods. *International Journal for Numerical Methods in Engineering*, 76(9):1434–1470, 2008.

[27] JM Melenk and I Babuška. The partition of unity finite element method: Basic theory and applications. *Computer Methods in Applied Mechanics and Engineering*, 139(1–4):289–314, 1996.

[28] CAM Duarte and JT Oden. Hp clouds – A meshless method to solve boundary-value problems. Technical Report 95-05, TICAM, The University of Texas at Austin, Taylor Hall 2.400, Austin, Texas, 78712, USA, 1995.

[29] JT Oden, CAM Duarte, and OC Zienkiewicz. A new cloud-based hp finite element method. *Computer Methods in Applied Mechanics and Engineering*, 153(1–2):117–126, 1998.

[30] J Huang, S Cen, Y Shang, and CF Li. A new triangular hybrid displacement function element for static and free vibration analyses of Mindlin-Reissner plate. *Latin American Journal of Solids and Structures*, 14(5):765–804, 2017.

[31] J Huang, S Cen, Z Li, and CF Li. An unsymmetric 8-node hexahedral solid-shell element with high distortion tolerance: Linear formulations. *International Journal for Numerical Methods in Engineering*, 116(12–13):759–783, 2018.

[32] Z Li, J Huang, S Cen, and CF Li. An unsymmetric 8-node hexahedral solid-shell element with high distortion tolerance: Geometric nonlinear formulations. *International Journal for Numerical Methods in Engineering*, 120(5):580–606, 2019.

[33] Z Li, S Cen, J Huang, and CF Li. Hyperelastic finite deformation analysis with the unsymmetric finite element method containing homogeneous solutions of linear elasticity. *International Journal for Numerical Methods in Engineering*, 2020. Accepted.

[34] PL Zhou, S Cen, J Huang, CF Li, and Q Zhang. An unsymmetric 8-node hexahedral element with high distortion tolerance. *International Journal for Numerical Methods in Engineering*, 109(8):1130–1158, 2017.

[35] Y Shang, S Cen, CF Li, and J Huang. An effective hybrid displacement function element method for solving the edge effect of Mindlin-Reissner plate. *International Journal for Numerical Methods in Engineering*, 102(8):1449–1487, 2015.

[36] V Dolean, P Jolivet, and F Nataf. *An introduction to domain decomposition methods – Algorithms, theory, and parallel implementation.* SIAM, Philadelphia, 2015.

[37] A Toselli and O Widlund. *Domain decomposition methods – Algorithms and theory.* Springer-Verlag, Berlin Heidelberg, 2005.

[38] T Strouboulis, K Copps, and I Babuška. The generalized element method. *Computer Methods in Applied Mechanics and Engineering*, 190(32–33):4081–4193, 2001.

[39] T Strouboulis, I Babuška, and K Copps. The design and analysis of the generalized finite element method. *Computer Methods in Applied Mechanics and Engineering*, 181(1–3):43–69, 2000.

[40] CA Duarte, I Babuška, and JT Oden. Generalized finite element methods for three-dimensional structural mechanics problems. *Computers & Structures*, 77(2):215–232, 2000.

[41] A Hansbo, P Hansbo, and MG Larson. A finite element method on composite grids based on Nitsche's method. *ESAIM: Mathematical Modelling and Numerical Analysis*, 37(3):495–514, 2003.

[42] R Becker, E Burman, and P Hansbo. A Nitsche extended finite element method for incompressible elasticity with discontinuous modulus of elasticity. *Computer Methods in Applied Mechanics and Engineering*, 198(41–44):3352–3360, 2009.

[43] A Hansbo and P Hansbo. An unfitted finite element method, based on Nitsche's method, for elliptic interface problems. *Computer Methods in Applied Mechanics and Engineering*, 191(47–48):5537–5552, 2002.

[44] A Massing, MG Larson, and A Logg. Efficient implementation of finite element methods on nonmatching and overlapping meshes in three dimensions. *SIAM Journal on Scientific Computing*, 35(1):C23–C47, 2013.

[45] R Glowinski, TW Pan, TI Hesla, and DD Joseph. A distributed Lagrange multiplier/fictitious domain method for particulate flows. *International Journal of Multiphase Flow*, 25(5):755–794, 1999.

[46] R Glowinski, TW Pan, and J Periaux. A fictitious domain method for Dirichlet problem and applications. *Computer Methods in Applied Mechanics and Engineering*, 111(3–4):283–303, 1994.

[47] KJ Bathe and MR Khoshgoftaar. Finite element free surface seepage analysis without mesh iteration. *International Journal for Numerical and Analytical Methods in Geomechanics*, 3(1):13–22, 1979.

[48] SE Benzley. Representation of singularities with isoparametric finite elements. *International Journal for Numerical Methods in Engineering*, 8(3):537–545, 1974.

[49] KJ Bathe and CA Almeida. A simple and effective pipe elbow element – Linear analysis. *Journal of Applied Mechanics*, 47(1):93–100, 1980.

[50] EN Dvorkin, AM Cuitiño, and G Gioia. Finite elements with displacement interpolated embedded localization lines insensitive to mesh size and distortions. *International Journal for Numerical Methods in Engineering*, 30(3):541–564, 1990.

[51] N Moës, J Dolbow, and T Belytschko. A finite element method for crack growth without remeshing. *International Journal for Numerical Methods in Engineering*, 46(1):131–150, 1999.

[52] T Belytschko, R Gracie, and G Ventura. A review of extended/generalized finite element methods for material modeling. *Modelling and Simulation in Materials Science and Engineering*, 17(4):043001 (24pp), 2009.

[53] J Kim and KJ Bathe. The finite element method enriched by interpolation covers. *Computers & Structures*, 116:35–49, 2013.

[54] NS Lee and KJ Bathe. Effects of element distortions on the performance of isoparametric elements. *International Journal for Numerical Methods in Engineering*, 36(20):3553–3576, 1993.

[55] M de Berg, O Cheong, M van Kreveld, and M Overmars. *Computational geometry: Algorithms and applications*. Springer-Verlag, Berlin Heidelberg, 3rd edition, 2008.

[56] JL Bentley and TA Ottmann. Algorithms for reporting and counting geometric intersections. *IEEE Transactions on Computers*, C–28(9):643–647, 1979.

[57] GR Cowper. Gaussian quadrature formulas for triangles. *International Journal for Numerical Methods in Engineering*, 7(3):405–408, 1973.

[58] DA Dunavant. High degree efficient symmetrical gaussian quadrature rules for the triangle. *International Journal for Numerical Methods in Engineering*, 21(6):1129–1148, 1985.

[59] PG Ciarlet. *The finite element method for elliptic problems*. SIAM, Philadelphia, 2002.

[60] D Chapelle and KJ Bathe. *The finite element analysis of shells – Fundamentals*. Springer-Verlag, Berlin Heidelberg, 2nd edition, 2011.

[61] Z Chen and H Wu. *Selected topics in finite element methods*. Science Press, Beijing, China, 2010.

[62] G Duvaut and JL Lions. *Inequalities in mechanics and physics*. Springer-Verlag, Berlin Heidelberg, 1976. Translated from the French by CW John.

[63] PG Ciarlet and PA Raviart. Interpolation theory over curved elements, with applications to finite element methods. *Computer Methods in Applied Mechanics and Engineering*, 1(2):217–249, 1972.

[64] ML Bucalem and KJ Bathe. *The mechanics of solids and structures – Hierarchical modeling and the finite element solution*. Springer-Verlag, Berlin Heidelberg, 2011.

[65] RH Macneal. A theorem regarding the locking of tapered four-node membrane elements. *International Journal for Numerical Methods in Engineering*, 24(9):1793–1799, 1987.

[66] A Ibrahimbegovic and EL Wilson. A modified method of incompatible modes. *Communications in Applied Numerical Methods*, 7(3):187–194, 1991.

[67] P van Oosterom. An R-tree based map-overlay algorithm. In *Proceedings EGIS/MARI'94*, Paris, France, 1994.

[68] U Finke and KH Hinrichs. Overlaying simply connected planar subdivisions in linear time. In *Proceedings of the eleventh annual symposium on computational geometry*, Vancouver, Canada, 1995.

[69] WR Franklin, C Narayanaswaml, M Kankanhalll, D Sun, MC Zhou, and PYF Wu. Uniform grids: A technique for intersection detection on serial and parallel machines. In *Proceedings of Auto-Carto 9*, Baltimore, MD, 1989.

[70] I Babuška. The finite element method with penalty. *Mathematics of Computation*, 27(122):221–228, 1973.

[71] I Babuška. The finite element method with Lagrangian multipliers. *Numerische Mathematik*, 20(3):179–192, 1973.

[72] ADINA R & D, Inc. *ADINA solids & structures*, volume 1 of *ADINA theory and modeling guide*. ADINA R & D, Inc., Watertown, MA, 2012.

[73] TH Cormen, CE Leiserson, RL Rivest, and C Stein. *Introduction to algorithms*. The MIT Press, Cambridge, MA, 3rd edition, 2009.